Western Graduate&PostdoctoralStudies

Western University
Scholarship@Western

Electronic Thesis and Dissertation Repository

9-15-2020 10:15 AM

Measurement and modeling of micro residual stresses in pure zirconium and Zr-2.5Nb polycrystals

Abdulla Alawadi, *The University of Western Ontario*

Supervisor: Abdolvand, Hamidreza, *The University of Western Ontario*

A thesis submitted in partial fulfillment of the requirements for the Master of Engineering Science degree in Mechanical and Materials Engineering

© Abdulla Alawadi 2020

Follow this and additional works at: https://ir.lib.uwo.ca/etd

Part of the Other Engineering Science and Materials Commons, and the Other Materials Science and Engineering Commons

Recommended Citation

Alawadi, Abdulla, "Measurement and modeling of micro residual stresses in pure zirconium and Zr-2.5Nb polycrystals" (2020). *Electronic Thesis and Dissertation Repository*. 7349.
https://ir.lib.uwo.ca/etd/7349

This Dissertation/Thesis is brought to you for free and open access by Scholarship@Western. It has been accepted for inclusion in Electronic Thesis and Dissertation Repository by an authorized administrator of Scholarship@Western. For more information, please contact wlswadmin@uwo.ca.

Abstract

In CANada Deterium Uranium (CANDU) nuclear reactors, Zr-2.5Nb alloy pressure tubes separate the hot water and cold moderator. Pressure tubes are susceptible to the diffusion of hydrogen from water and formation of a brittle phase called zirconium hydrides. The diffusion and formation of hydrides are affected by the state of stresses within the tubes. As such, it is of great significance to understand the source of the stresses that develop within the tubes. This thesis focuses on the characterization of the micro and nano scale residual stresses that develop in pure zirconium and Zr-2.5Nb polycrystals. With using three-dimensional synchrotron X-ray diffraction (3D-XRD) technique and crystal plasticity finite element (CPFE) modeling, it is shown that the state of micro-residual stresses in pure zirconium is affected by grain size and the specimen texture. In addition, the variation of microstructure and residual stress in a neutron irradiated Zr-2.5Nb CANDU pressure tube specimens are studied and compared to an unirradiated specimen. It is shown that the microstructure, texture, and the grain-scale residual stresses of the pressure tube vary as a function of the axial position along the pressure tube.

Keywords

3D-XRD, HR-EBSD, CPFE, residual stress, neutron irradiation, size effect, texture effect, Zr-2.5Nb

Summary for Lay Audience

Nuclear energy provides 16% of the total electricity generated in Canada. In Ontario, about 60% of electricity is generated by the CANada Deterium Uranium (CANDU) nuclear reactors. Pressure tubes are one of the main components of the CANDU reactors. Hot water runs through pressure tubes and removes heat from fuel bundles. CANDU pressure tubes are made of a Zr-2.5Nb alloy. The tubes are susceptible to cracking due to the diffusion of hydrogen from water and formation of a brittle phase called zirconium hydride. It is reported in literature that the formation of this brittle phase is affected by the state of localized stresses that develop in the tube. Therefore, the goal of this research is to better understand how and why these stresses develop. This is done by firstly characterizing the state of stresses in pure zirconium crystals in three dimension using an experimental technique known as 3D-XRD. It is found that grain size and how the atoms sit within grains (orientation) have a significant effect on the state of the stresses. Further, specimens were removed from different location of a CANDU pressure tube that was in a reactor for 22 years. Electron diffraction and finite element numerical modeling are used to understand how the state of residual stresses varies along the tube. We report that the front-end of the pressure tubes is relatively more stressed compared to other axial positions that we investigated.

Statement of Co-Authorship

This thesis is presented in an integrated article format and consists of the following three articles which are published or are ready for submission:

Chapter 2: Alawadi, A., Abdolvand, H., "Measurement and modeling of micro residual stresses in zirconium crystals in three dimension," *Journal of the Mechanics and Physics of Solids*, vol. 135, 2020, 103799, doi: 10.1016/j.jmps.2019.103799.

Contribution: The CPFE model develped by Prof. Abdolvand was used. The 3D-XRD experiment was conducted by Prof. Abdolvand at the European Synchrotron Radiation Facility (ESRF), France. Postprocessing of the model results and experimental data were conducted by me. Most of the codes for postprocessing the results were developed by me. With the exception of figures 2.1, 2.2, and 2.3, all figures in this article were generated by me. Interpretations and conclusions are my own. I have written the first draft of the article and Prof. Abdolvand editted the article, and gave advice on conclusions.

Chapter 3: Alawadi, A., Abdolvand, H., Bach, M., Topping, M., St Lawrence, S., "Microstructural variations in a neutron irradiated Zr-2.5Nb CANDU pressure tube" *ready for submission.*

Chapter 4: Alawadi, A., Abdolvand, H., Bach, M., St Lawrence, S., "Residual stresses in a neutron irradiated Zr-2.5Nb CANDU pressure tube" *ready for submission.*

Speceimens were prepared at the Canadian Nuclear Laboratories and provided by Drs. Bach and St Lawrence. EBSD measurmeents were conducted at the Reactor Materials Testing Laboratory, Queen's University with the help of Dr. Topping. The postprocessing of the EBSD data was done by me. The codes generated for post-processing are my own. The CPFE models for chapter 4 were originally developed by Prof. Abdolvand, but I modified the code to include the effects of irradiation growth. The post-processing of the CPFE results was done by me. The postprocessing of HR-EBSD patterns was done by Prof. Abdolvand. The figures for chapters 3 and 4 were generated by me. Interpretations and the conclusions made in chapters 3 and 4 are my own. I have written the first drafts of the articles and Prof. Abdolvand edited them and gave his suggestions and advice on the interpretation of results and conclusions.

Acknowledgments

Firstly, I would like to acknowledge professor Hamidreza Abdolvand for giving me the opportunity to join his MSDL research group. I would also like to thank him for always offering help and valuable advice that helped me throughout my research and helped me develop much needed skills. To the rest of the MSDL group, thank you for creating a healthy and motivational environment that encouraged and motivated me to always do my best.

I would also like to acknowledge NSERC, CNL, and CANDU owners group for supporting this project.

Finally, to my family, thank you for always supporting me, believing in me, and inspiring me to pursue and achieve my goals.

Table of Contents

Abstract ii

Keywords iii

Summary for Lay Audience iv

Statement of Co-Authorship v

Acknowledgments vi

Table of Contents vii

List of Tables x

List of Figures xi

List of Acronyms xv

List of Symbols xvi

1 Introduction 1

1.1 Motivation 1

1.2 CANDU Pressure Tubes 2

1.3 Experimental Techniques 4

1.3.1 Three-Dimensional synchrotron X-Ray Diffraction 5

1.3.2 Electron Backscatter Diffraction 6

1.4 Crystal plasticity finite element 10

1.5 Objectives 2

1.6 Thesis Overview 12

1.7 References 13

2 Measurement and modeling of micro residual stresses in zirconium crystals in three dimensions 15

2.1 Introduction 15

2.2 Experimental Method 17

2.2.1 Sample 17

2.2.2 3D-XRD experiment 18
2.3 Crystal Plasticity Simulations 21
2.3.1 Input model 21
2.4 Results 26
2.4.1 3D-XRD vs. CPFE results 26
2.4.2 Effects of grain size 30
2.5 Discussion 32
2.5.1 Size effects 32
2.5.2 Effects of neighboring grains 35
2.5.3 Effects of Texture 38
2.6 Conclusion 42
2.7 References 43
3 Microstructural variations in a neutron irradiated Zr-2.5Nb CANDU pressure tube .. 49
3.1 Introduction 49
3.2 Samples and experimental setup 52
3.3 Results 53
3.3.1 Reconstruction of grain maps 53
3.3.2 Microstructure 56
3.4 Discussion 57
3.4.1 Texture Analysis 57
3.4.2 Misorientation Analysis 59
3.5 Conclusion 63
3.6 References 64
4 Residual stresses in a neutron irradiated Zr-2.5Nb CANDU pressure tube 66
4.1 Introduction 66
4.2 Experimental Method 69

4.2.1 Sample 69
4.2.2 HR-EBSD Experiment 70
4.3 CPFE Model 72
4.4 Results and Discussion 76
4.4.1 HR-EBSD Results 76
4.4.2 Effects of thermal residual stresses 77
4.4.3 Effects of Irradiation Growth 79
4.4.4 Effects of Combined Loading 83
4.4.5 CPFE vs HR-EBSD Results 85
4.5 Conclusion 88
4.6 References 89
5 Conclusions and Future Recommendations 92
5.1 Conclusions 92
5.2 Future Recommendations 93
Curriculum Vitae 95

List of Tables

Table 2.1 Chemical composition of the CPZr sample [2]. Numbers are given in ppm 18

Table 2.2 Details of the 3D-XRD experiment 19

Table 2.3 single crystal parameters used for S4, S5, and S17 models 23

Table 2.4 Grain 4329 and 3144 stress values 33

Table 2.5 Grain 5732 and 3492 stress values 36

Table 2.6 Stress Values for grain 3144 and grain 3492 40

Table 3.1 Axial positions of the samples in the pressure tube, number of EBSD maps, and average map size. 53

Table 3.2 Number of measured grains after filtering 54

Table 3.3 Summary of average grain area measured for each sample 56

Table 3.4 Summary of Kearns factor 58

Table 4.1 Summary of the analyzed samples 70

Table 4.2 Irradiation growth coefficients 74

Table 4.3 Summary of HR-EBSD results 77

Table 4.4 Summary of the CPFE results for the T-model 78

Table 4.5 Summary of the CPFE results for G1-Model 80

Table 4.6 Summary of the CPFE results for G2-Model 81

Table 4.7 Summary of the CPFE results for C1-Model 83

Table 4.8 Summary of the C2-Model Results 84

List of Figures

Figure 1.1 A schematic of a CANDU pressure tube and a calandria tube [6]. 3

Figure 1.2 An incident beam diffracting off crystallographic planes [10]. 5

Figure 1.3 (a) Schematic of 3D-XRD. (b) Example of a diffraction pattern [8]. 6

Figure 1.4 The schematic of an EBSD setup [12]. 7

Figure 1.5 Example of a Kikuchi pattern of a silicon sample obtained from EBSD [10]. 7

Figure 1.6 Kikuchi pattern before and after load application [14]. 9

Figure 2.1 (a) an EBSD map of the undeformed sample with the color legend given in the right hand side of the figure. Colors are coded with respect to inverse pole figure z. (b) The sample used in 3D-XRD experiment with the lab coordinate system shown in the bottom of the picture; z-axis is the loading direction and the sample gauge length is 20 mm. (c) The (0002) and 1100 measured pole figures from 3D-XRD. Scales are given in multiples of random distribution. (d) Test set-up..... 20

Figure 2.2 (a) The modelled microstructure that was imported into a finite element solver for simulating 1038 grains. Random colors are assigned to elements to distinguish different grains. (b) The corresponding pole figure of the modelled microstructure. (c) Comparison between the measured volumes of the grains and the simulated ones using Voronoi and weighted Voronoi tessellation. (d) Comparison between the average stress-strain curves calculated for each model with the experimentally measured ones..... 25

Figure 2.3 Measured stresses and orientations from 3D-XRD experiment: (a) the misorientation between the basal plane normals and the loading direction (β) for preload. Stress in the loading direction at the (b) onset of plasticity (c) applied strain of 1.2%, (d) preload and (e) unload. Hydrostatic stresses at the (f) preload and (g) unload steps. 29

Figure 2.4 Grain measured residual stresses as a function of the angle between the basal plane normals (β) and the loading direction: (a) σ_{33} and (b) σ_{11} at the preload and (c) σ_{33} at the unload. The size of each circle is proportional to the measured volume for each grain. (d)

– (i): Comparison between σ_{11}, σ_{22}, and σ_{33} obtained from CPFE and 3D-XRD for the preload and unload steps. 30

Figure 2.5 Grain average σ_{33} and σ_H as a function of grain diameters: Results from 3D-XRD are shown in the top row and those from CPFE are shown in the bottom row. The first two columns are from preload step and the last two are from unload. The magnitudes of the measured and calculated data are used for data fitting. 31

Figure 2.6 Grain-average stresses and stress variations for σ_{11} and σ_H: Results for grain 4329 and 3144 are shown in the first and second rows, respectively. The calculated full width of half max (FWHM), stress range, and the ratio of FWHM to stress range of (g-i) σ_{11} and (i-l) σ_H. 34

Figure 2.7 Comparison between CPFE and 3D-XRD results for the surface grain 2309: (a) σ_{11}, (b) σ_{22}, and (c) σ_{33}. 35

Figure 2.8 Grain-average stresses and stress variations for σ22 and σH: Results for grain 5732 and 3492 are shown in the top and bottom rows, respectively. The first two columns are from the preload step and the last two are from the unload step. 37

Figure 2.9 The distribution of misorientation of (a) grain 5732 and (b) grain 3492 with their neighbors. CPFE results for grain 3492: the variation of (c) σ_H and (d) σ_{VM} for the element located at the grain boundaries as a function of basal plane misorientation with the immediate neighboring grain. The lines shown in (c) and (d) are for the ideal bi-crystal model shown above. 38

Figure 2.10 (a) The pole figure of the "randomly" textured CPFE model. The distribution of misorientations between the basal plane normals of any two neighboring grains in (b) "random" and (c) "original" model. Grain-average residual stresses from "random" and "original" model. Grain-average residual stresses from "random" and "original" model: (d) σ_{11}, (e) σ_{22}, and (f) σ_{33}. Grain-average residual stresses as a function of grain dimeter from "random" model: (g) σ_{33} and (h) σ_H. The absolute of the calculated data is used for data fitting. 41

Figure 3.1 Grain maps from sample A1 reconstructed using (a) 2.5° and (b) 1° misorientation thresholds. (c) The corresponding quality map. Grain maps from sample A1 reconstructed using (d) 1° and (e) 0.5° misorientation thresholds. (f) The corresponding quality map. A reconstructed map from the AR sample (g) before filtering, (h) after filtering noise and using 10 points as the minimum limit for determining grains, and (i) after filtering the noise and using 50 points as the minimum limit for determining grains. The inverse pole figure Y legend and the coordinate system that are used are shown on the right. 55

Figure 3.2 (a) The distribution of the measured grain areas for all samples. (b) The distribution of the measured grain aspect ratios for all samples. 57

Figure 3.3 The misorientation between the basal plane normals and (a) TD, (b) RD, and (c) AD. The measured pole figures of (d) S1, (e) S2, (f) S3, and (g) AR samples. Pole figures are provided in the units of multiple random distribution (mrd). 59

Figure 3.4 (a) Distribution of the grain average misorientation. (b) The local misorientation plot of a grain in sample S1. (c) The local misorientation plot of a grain from the AR sample. (d) The local misorientation plot of the major and minor axes of a grain in sample S1. (e) The grain average misorientation plotted against the grain area. (f) The grain average misorientation plotted against the grain aspect ratio..... 62

Figure 4.1 (a) A schematic of pressure tube and the coordinate system used in this paper. (b) An example of a Kikuchi pattern obtained from a neutron irradiated sample. (c) An example of relative σ_R stress measured by HR-EBSD (c) Measured pole figures for (d) S1, (e) S2, (f) S3, and (g) AR samples. 71

Figure 4.2 EBSD maps of (a) sample S1, (b) sample S3, and (c) AR sample with their corresponding reconstructed CPFE models shown in (d) I(e), respectively. The results of CPFE modeling for σ_T stress (in MPa) for (g) sample S1, (h) sample S3, and (i) sample AR. 72

Figure 4.3 Comparison between calculated and measured growth strain after calibrating the parameters of Eq. 6. 75

Figure 4.4 CPFE results: the distribution of (a) σR and (b) σT from all integration points assigned to samples S1, S3, and AR. Histograms of the FWHM distribution of (c) σR and (d) σT for individual grains for all grains of samples S1, S3, and AR. 79

Figure 4.5 CPFE results: the distribution of (a) σ_R and (b) σ_T from all integration points assigned to samples S1, S3, and AR. Histograms of the FWHM distribution of (c) σ_R and (d) σ_T for individual grains for all grains of samples S1, and S3. 81

Figure 4.6 CPFE results: the distribution of (a) σ_R and (b) σ_T from all integration points assigned to samples S1, S3, and AR. Histograms of the FWHM distribution of (c) σ_R and (d) σ_T for individual grains for all grains of samples S1, and S3. 82

Figure 4.7 . CPFE results: the distribution of (a) σ_R and (b) σ_T from all integration points assigned to samples S1, S3, and AR. Histograms of the FWHM distribution of (c) σ_R and (d) σ_T for individual grains for all grains of samples S1, and S3. 84

Figure 4.8 CPFE results: the distribution of (a) σ_R and (b) σ_T from all integration points assigned to samples S1, S3, and AR. Histograms of the FWHM distribution of (c) σ_R and (d) σ_T for individual grains for all grains of samples S1, and S3. 85

Figure 4.9 A comparison of relative stress and elastic rotation variation trends obtained from CPFE models and HR-EBSD. The first column shows the sample from which the grains are obtained. The second column shows the stress and elastic rotation components examined. The stresses and elastic rotation from CPFE are shown after reducing the reference point values. The reference points are shown by the red dots. The stresses are reported in MPa and elastic rotations are reported in radians. 87

List of Acronyms

Zr	Zirconium
CANDU	CANada Deuterium Uranium
HCP	Hexagonal close-packed
BCC	Body centered-cubic
3D-XRD	Three-dimensional synchrotron X-ray diffraction
EBSD	Electron backscatter diffraction
COM	Center of mass
SEM	Scanning electron microscope
HR-EBSD	High resolution electron backscatter diffraction
CTE	Coefficient of thermal expansion
IP	Integration point
FWHM	Full width at half maximum
GB	Grain boundary
TD	Transverse direction
RD	Radial direction
LD	Longitudinal direction
MD	Molecular dynamics
BPN	Basal plane normal
CRSS	Critical resolved shear stress

List of Symbols

σ_{11}	Stress in the beam direction
σ_{22}	Stress in the transverse direction
σ_{33}	Stress in the loading direction
σ_H	Hydrostatic stress
β	Angle between the basal plane normal and loading direction
σ_{VM}	Von Mises stress
σ_R	Radial normal stress
σ_T	Transverse normal stress
σ_{RT}	Radial-transverse shear stress
ω_{RT}	Radial-transverse elastic lattice rotation

1 Introduction

This thesis is presented in an integrated article format consisting of three articles. After presenting the motivation and objectives for this research, the details of the implemented experimental and numerical techniques are discussed. The thesis outline is provided in the last section of this chapter.

1.1 Motivation

In Canada, more than 16% of electricity is generated by CANDU nuclear reactors which makes nuclear energy as a significant part of Canada's energy supply [6]. Zirconium (Zr) and its alloys are used in manufacturing of structural materials used in the core CANDU reactors because these alloys have good mechanical and corrosion properties. In addition, Zr has a low neutron absorption cross section which increases the efficiency of the fission process as well as allows for the usage of natural uranium as the nuclear fuel. Examples of the components that use Zr alloys include calandria tube, fuel cladding, and pressure tubes. The calandria vessel is the outermost tube and contains heavy water that acts as the moderator and neutron reflector. The calandria tube is made of Zircaloy-2 [1] and contains thermally insulating gas. The fuel cladding is the casing in which the fuel rods are contained and is made of Zircaloy-4 [2]. The pressure tube, which is the focus of this thesis, is made of a zirconium-niobium (Zr-2.5Nb) alloy and is manufactured by extrusion at elevated temperatures [3].

Zr-2.5Nb is a dual phase alloy of α-zr crystals with hexagonal close packed (HCP) structure and a β phase with body centered crystal structure (BCC). During service, hydrogen diffuses into zirconium crystals and form a brittle phase called zirconium hydrides. Hydrogen diffusion depends on many parameters, including, zirconium texture, microstructure and local state of stresses. It has been shown that the formation of hydrides is significantly affected by the stresses that develop at the grain boundaries as well as those that develop within the grains of the alloy [4], [5]. In addition, it is suggested that the thermal residual stresses that develop during manufacturing of the pressure tubes may accelerate the formation of hydrides. The objective of this research is to characterize the

residual stresses that develop in pure Zr and Zr-2.5Nb during heat treatments and characterize the correlation between micro residual stresses and materials texture as well as microstructure.

1.2 Objectives

The main objective of this thesis is to characterize micro- and nano-scale residual stresses that develop in pure Zr metal and Zr-2.5Nb pressure tubes. In the first step, the thermal residual stresses that develop in a fully recrystallized pure Zr is characterized. This is to understand the effects of heat treatment, materials texture, and microstructure on development of residual stresses. This is done by using 3D-XRD and CPFE methods.

In the second step, an intensive microstructure and texture analysis is performed on neutron irradiated Zr-2.5Nb pressure tube specimens using EBSD. These specimens were obtained from different axial locations of a pressure tube to understand how the microstructure and texture of the tube varies as a function of the axial location.

Finally, the residual stresses of the neutron irradiated samples are characterized using HR-EBSD and CPFE methods. Results are compared against those obtained for unirradiated specimens taken from the offcut of the same pressure tube. The goal of this step is to understand how residual stresses vary along the axial position of the pressure tube and if such variations are significant enough to affect hydride embrittlement.

1.3 CANDU Pressure Tubes

CANDU nuclear reactors contain 380-480 fuel channels. The design of the CANDU fuel channels is based on four major criteria. The first one is to use natural uranium as a fuel. To improve neutron economy, the coolant used is heavy water (D_2O) which runs through pressure tubes at high temperature and pressure. For the same reason, D_2O is used as the neutron moderator at low temperature and pressure. Fuel channels are mostly made of Zr alloys due to their low neutron absorption cross section. The pressure tubes should be easily replaced for surveillance and maintenance as the knowledge on Zr alloys, at the time, was limited. CANDU fuel channels are designed to allow for on-power refueling [3].

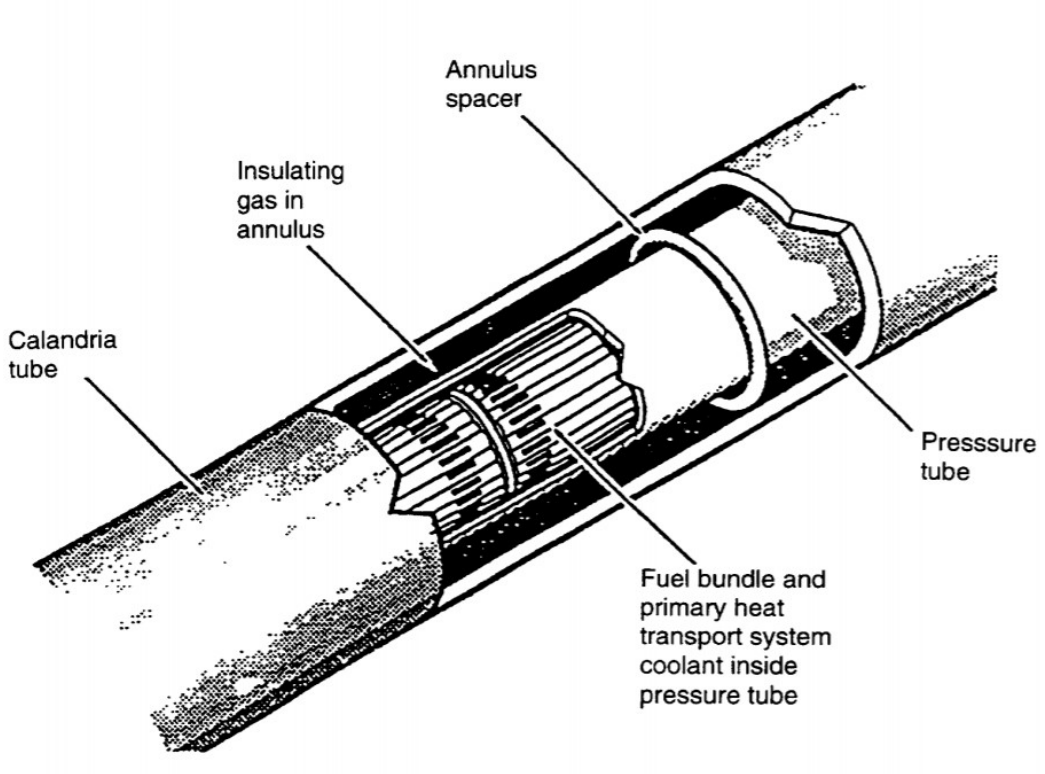

Figure 1.1 A schematic of a CANDU pressure tube and a calandria tube [6].

Figure 1.1 shows a schematic of a CANDU pressure tube and Calandria tube. The pressure tube is placed inside the calandria tube and is thermally insulated from the cooler calandria by annulus gas of dry CO_2. The pressure tube is physically separated from the calandria using close coiled helical spring annulus spacers, which are placed 1 m apart along the tube. The pressure tube is supported at each end by end fittings [6]. At operating conditions, the coolant temperature is 250-270 °C at the inlet of the tube and 292-315 °C at the outlet. The operating pressure is 10.5 MPa at the inlet and 9.9 MPa at the outlet. The operating pressure results in an axial stress of 65 MPa, and a hoop stress of 130 MPa and 122 MPa at the inlet and outlet of the pressure tube, respectively [7].

CANDU pressure tubes are made of a Zr-2.5Nb alloy, and are 6 m long, with average diameter of 104 mm, and wall thickness of 4.2 mm [7]. The Zr-2.5Nb alloy is a dual phase alloy consisting of α- and β-Zr. The α-Zr phase has hexagonal close-packed (HCP) crystal structure and has anisotropic elastic, plastic, and thermal properties. That is, the response

of the alloy to a thermomechanical load depends on the direction of the applied load. The α-Zr grains are elongated along the axial direction of the pressure tube. The β-Zr phase has a body centered cubic (BCC) crystal structure and has anisotropic elastic and plastic properties; however, it is thermally isotropic. The β-Zr grains are mainly found at the α-α grain boundaries. The main deformation modes of a pressure tube are irradiation growth, irradiation creep and thermal creep. Irradiation growth is the change in the dimension of the HCP crystals due to a neutron flux, but under no applied load. Irradiation creep is the change in the dimension of the crystals due to both stress and neutron flux. Thermal creep is the dimensional change due to temperature and stress. These mechanisms lead to dimensional changes in pressure tubes, one of which is known as diametral expansion. Diametral expansion is the increase in the circumference of the pressure tube. The main contributor to diametral expansion is irradiation creep, with a smaller contribution of thermal creep. The effect of irradiation growth on diametral expansion is negative i.e. it causes the circumference to decrease; however, the contribution of creep is higher, so the pressure tube ends up expanding. Due to irradiation growth and irradiation creep, the length of pressure tubes increases with time. Since creep and growth are volume conserving, the pressure tube's walls end up thinning as results of axial elongation and diametral expansion. Lastly, pressure tubes prone to sag due to the weight of the fuel bundles and heavy water. This is particularly detrimental to pressure tubes if the spacers are moved from their initial locations, causing the hot pressure tube contacting the cooler calandria tube [7]. This contact causes a temperature gradient to form through the thickness of pressure tubes which could result in the formation of brittle hydrides and initiate a process known as Delayed Hydride Cracking (DHC) [6].

1.4 Experimental Techniques

Two experimental techniques are used in this research, three-dimensional synchrotron X-ray diffraction (3D-XRD) and electron backscatter diffraction (EBSD). In this section, a brief explanation of each technique is provided.

1.4.1 Three-Dimensional synchrotron X-Ray Diffraction

3D-XRD is a diffraction based technique that can be used to measure the elastic strain tensor, center of mass (COM), orientation, relative volume, and stress tensor of individual grains in three dimension [8]. The X-rays generated by a synchrotron source are diffracted by the crystallographic planes of crystals and are recorded on a detector. The condition that must be met for the X-rays for diffraction follows the Bragg's law:

$$n\lambda = 2d_{hkl}sin\theta_{hkl} \tag{1.1}$$

where n is an integer, λ is the wavelength of the incident X-ray beam, d_{hkl} is the interplanar spacing of the hkl plane, and θ_{hkl} is the diffraction angle of the hkl plane. For α-Zr with HCP crystals the interplanar planar spacing is:

$$\frac{1}{d_{hkil}^2} = \frac{4}{3}\left(\frac{h^2+hk+k^2}{a^2}\right) + \frac{l^2}{c^2} \tag{1.2}$$

where h, k, and l are the miller indices and a and c are unit cell parameters of the HCP crystal. Figure 1.2 shows a schematic of the Bragg's condition. The 3D-XRD setup (shown in Figure 1.3(a)) includes an X-ray beam that goes through a monochromator to ensure that the generated X-ray beam is monochromatic, i.e, has a single wavelength. The sample is mounted on a ω-stage that can rotate [-180°:180°]. The sample is rotated about the ω-axis to capture several crystallographic planes of the same grain and bring grains to the diffraction condition. The diffracted beam is then recorded on the 2D detector [9].

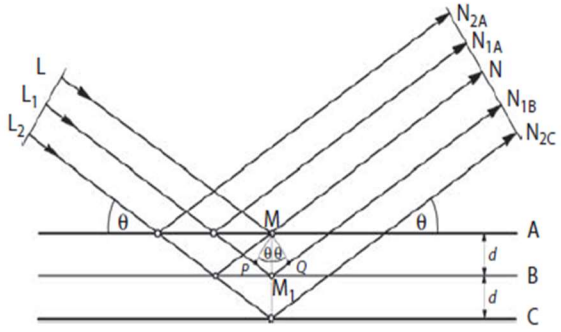

Figure 1.2 An incident beam diffracting off crystallographic planes [10].

Figure 1.3(b) shows an example of a diffraction pattern collected in a 3D-XRD experiment. Applying loads to the sample changes the interplanar distancing of the planes in crystals, therefore, changing the diffraction angle, and, consequently, causing shifts in the diffraction patterns. The elastic strain is subsequently calculated using [11]:

$$\varepsilon_{hkl} = \frac{d_{hkl} - d_{ref}}{d_{ref}} = \frac{sin\theta_{ref}}{sin\theta_{hkl}} - 1 \tag{1.3}$$

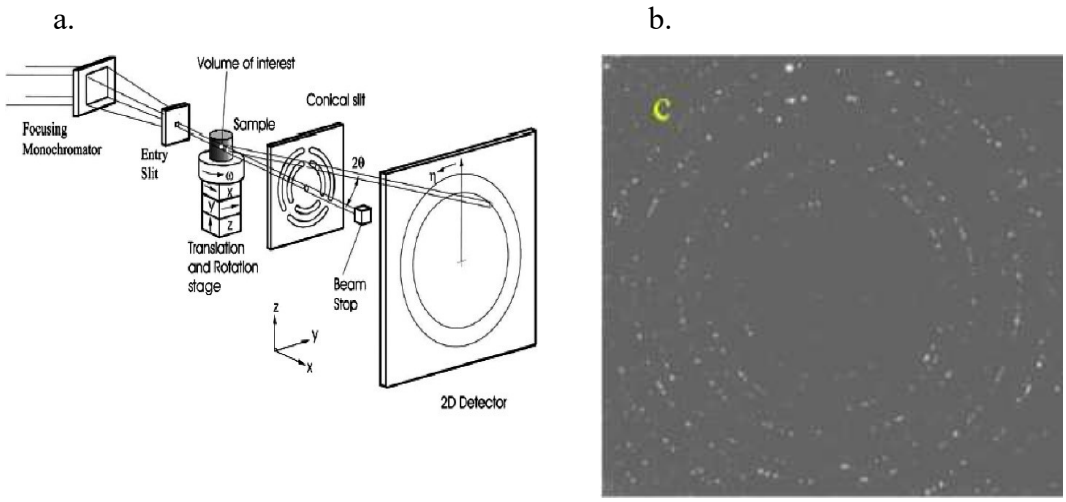

Figure 1.3 (a) Schematic of 3D-XRD. (b) Example of a diffraction pattern [8].

1.4.2 Electron Backscatter Diffraction

EBSD is another diffraction technique used in this research. The technique follows the same diffraction principles discussed in the previous section. In EBSD, the experimental setup includes a scanning electron microscope (SEM) in which the sample is placed. The experimental setup also includes an EBSD detector, a phosphor screen, and a charged couple device (CCD) camera. The samples used for the experiments of this research are 2 mm thick foils. The foils are electropolished at 17 V at -30 °C in a solution of 95% methanol and 5% perchloric acid until the surface quality is suitable for EBSD measurements. After preparation, the samples are placed in the SEM chamber at a tilt of 20° with respect to the incident beam direction. Figure 1.4 shows a schematic of the experimental setup.

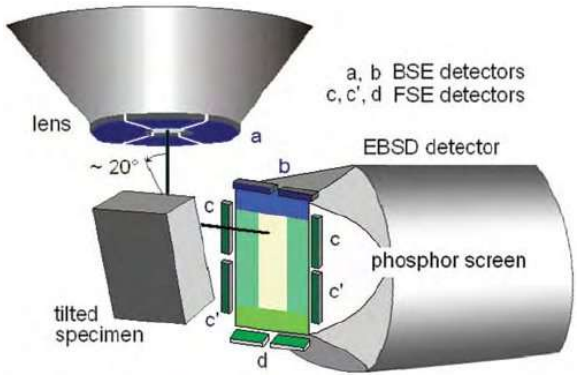

Figure 1.4 The schematic of an EBSD setup [12].

One of the main applications of EBSD is mapping the nanoscale crystallographic orientation. Unlike 3D-XRD, EBSD can measure the variation of crystal orientation within a grain rather than a single average orientation for each grain. The diffracted electrons form a pattern known as Kikuchi pattern, which is shown in Figure 1.5.

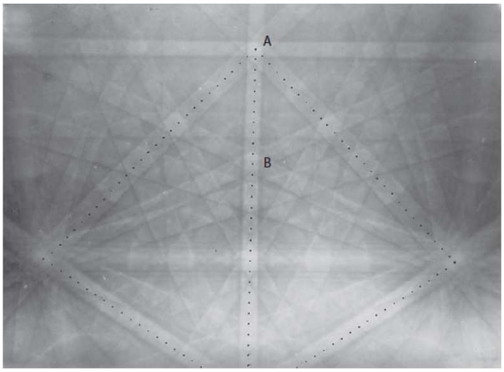

Figure 1.5 Example of a Kikuchi pattern of a silicon sample obtained from EBSD [10].

The Kikuchi pattern includes Kikuchi bands with certain widths that intersect other bands at a certain angle. Each band represents a unique crystallographic orientation. The dotted line represents a feature of a band called a zone axis which is used to derive the transformation matrices to map from the crystallographic orientation using [10]:

$$\begin{pmatrix} q_1^i \\ q_2^i \\ q_3^i \end{pmatrix} * \begin{pmatrix} h \\ k \\ l \end{pmatrix} = cos\alpha_i \sqrt{(q_1^i)^2 + (q_2^i)^2 + (q_3^i)^2} \tag{1.4}$$

where q is the position of the zone axis relative to the pattern center labeled B in Figure 1.5, and the superscript i represents the number of the band being examined (e.g. band 1, band 2, etc.). The subscripts 1,2, and 3 represent the axes (x_1, x_2, x_3). α is the angle between any two bands. q and α are measured directly from the Kikuchi pattern, and then the equation is solved to find h, k, and l, which are the crystallographic plane indices. The crystallographic indices are used to find a rotation matrix to change the coordinates from the crystallographic coordinates to the Kikuchi pattern coordinates using the following equation [10]:

$$R_{CP} = \big((BNxhkl)xBN \qquad BNxhkl \qquad BN\big) \tag{1.5}$$

where BN is the coordinate of the incident beam normal to the sample and hkl is the crystallographic index. The previous equation describes a cross multiplication operation between the incident beam and the crystallographic indices. Another rotation matrix is required to transform the pattern coordinates to the sample coordinates [10]:

$$R_{PS} = \begin{pmatrix} \cos\gamma & -\sin\gamma & 0 \\ \sin\gamma & \cos\gamma & 0 \\ 0 & 0 & 1 \end{pmatrix} \tag{1.6}$$

where γ is the angle between the Kikuchi band and the sample y-axis. Finally, the rotation matrix between the crystal coordinates to the sample coordinates equals to:

$$R_{CS} = R_{CP} * R_{PS} \tag{1.7}$$

with this equation, the orientations of the crystals within the sample are known.

High resolution EBSD (HR-EBSD), developed by Wilkinson et al [13] allows for, in addition to orientation mapping, measuring nanoscale localized relative elastic strain and elastic rotation. The precision of HR-EBSD for measuring strain is $1x10^{-4}$ and for measuring elastic lattice rotations is $1x10^{-4}$ radians [13]. In HR-EBSD, the shifts in the Kikuchi patterns are correlated to elastic strains (Figure 1.6) using the Eulerian displacement gradient [13]:

$$\boldsymbol{q} = \boldsymbol{Q} - (\boldsymbol{Q} \cdot \hat{\boldsymbol{r}})\hat{\boldsymbol{r}} \tag{1.8}$$

where **q** is the pattern shift or displacement on the phosphor screen, $\hat{\boldsymbol{r}}$ is the unit vector along the zone axis direction of the band that is being studied, and **Q** is defined by [13]:

$$\boldsymbol{Q} = a\hat{\boldsymbol{r}} = \begin{pmatrix} \frac{\partial u_1}{\partial x_1} & \frac{\partial u_1}{\partial x_2} & \frac{\partial u_1}{\partial x_3} \\ \frac{\partial u_2}{\partial x_1} & \frac{\partial u_2}{\partial x_2} & \frac{\partial u_2}{\partial x_3} \\ \frac{\partial u_3}{\partial x_1} & \frac{\partial u_3}{\partial x_2} & \frac{\partial u_3}{\partial x_3} \end{pmatrix} \begin{pmatrix} \boldsymbol{r_1} \\ \boldsymbol{r_2} \\ \boldsymbol{r_3} \end{pmatrix} \tag{1.9}$$

where "a" is the displacement gradient tensor. The pattern shifts in HR-EBSD are measured at the surface of the sample, limiting the application of HR-EBSD to in-plane strains. Therefore, the term $Q_3 = 0$, and the problem is treated as a plane stress problem ($\sigma_{33} = 0 = C_{33kl}\varepsilon_{kl}$).

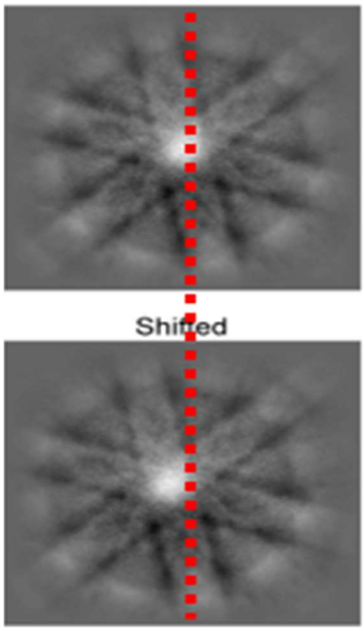

Figure 1.6 Kikuchi pattern before and after load application [14].

Expanding and substituting terms from equations (1.8) and (1.9) yield two independent equations as follows:

$$r_1 r_2 \left[\frac{\partial u_1}{\partial x_1} - \frac{\partial u_3}{\partial x_3}\right] + r_2 r_3 \frac{\partial u_1}{\partial x_2} + r_3^2 \frac{\partial u_1}{\partial x_3} - r_1^2 \frac{\partial u_3}{\partial x_1} - r_1 r_2 \frac{\partial u_3}{\partial x_2} = r_3 q_1 - r_1 q_3$$

$$r_2 r_3 \left[\frac{\partial u_2}{\partial x_2} - \frac{\partial u_3}{\partial x_3}\right] + r_1 r_3 \frac{\partial u_2}{\partial x_1} + r_3^2 \frac{\partial u_2}{\partial x_3} - r_1 r_2 \frac{\partial u_3}{\partial x_1} - r_2^2 \frac{\partial u_3}{\partial x_2} = r_3 q_2 - r_2 q_3 \tag{1.10}$$

The displacement of the pattern q and the unit vector $\hat{\boldsymbol{r}}$ can be measured directly by cross correlating the shifted pattern to the original reference pattern, leaving 8 unknowns after applying the plane stress condition. Therefore, 4 different noncoplanar measurements of q and $\hat{\boldsymbol{r}}$ are required. After the displacement gradient tensor elements are calculated, the elastic strain tensor and the elastic rotation tensor are calculated using:

$$\varepsilon_{ij} = \frac{1}{2}\left(\frac{\partial u_i}{\partial x_j} + \frac{\partial u_j}{\partial x_i}\right) \text{ and } \omega_{ij} = \frac{1}{2}\left(\frac{\partial u_i}{\partial x_j} - \frac{\partial u_j}{\partial x_i}\right) \tag{1.11}$$

where ε_{ij} is the strain tensor and ω_{ij} is the rotation tensor. Finally, the stresses are calculated from the strain tensor using:

$$\sigma_{ij} = C_{ijkl}\varepsilon_{kl} \tag{1.12}$$

where σ_{ij} is the stress tensor and C_{ijkl} is the stiffness tensor. HR-EBSD is used to measure localized elastic strains, elastic rotations, and stresses at several locations within each grain.

1.5 Crystal plasticity finite element

The main numerical technique used in this project is crystal plasticity finite element (CPFE). Crystal plasticity is a set of constitutive equations that describe plastic deformation by the movement of dislocations on a slip plane in a slip direction [15]. The crystal plasticity user material (UMAT) subroutine used in this project was developed by Dr. Abdolvand [16]. A brief explanation of the formulation is given here. The code was developed based on the mathmetical formulation for rate-dependent equations developed by Hill [17], Hill and Rice [18], Asaro [15], and Asaro and Needleman [19]. The total strain rate ($\dot{\varepsilon_{tot}}$) is divided into elastic ($\dot{\varepsilon_{el}}$) and plastic ($\dot{\varepsilon_{pl}}$) parts. The plastic strain rate is calculated by:

$$\dot{\varepsilon}^{pl} = \sum_{\alpha=1}^{N^{spl}} P^{\alpha}\dot{\gamma}^{\alpha}$$
$$P^{\alpha} = sym(S^{\alpha}) \; where \; S^{\alpha} = d^{\alpha} \otimes n^{\alpha} \tag{1.13}$$

P^{α} is the symmetric part of the Schmid tensor (S^{α}) for the slip system α, d^{α} is the direction of the slip and n^{α} is the normal to the slip plane. The slip rate of the slip system α is calculated using:

$$\dot{\gamma}^{\alpha} = \dot{\gamma}_0 \left|\frac{\tau^{\alpha}}{g^{\alpha}}\right|^{n} sign\left(\frac{\tau^{\alpha}}{g^{\alpha}}\right) \tag{1.14}$$

where $\dot{\gamma}_0$ is a reference shear strain rate, and n is a constant that controls rate dependency, both of which are material properties. τ^{α} and g^{α} are the resolve shear stress on the slip system α and the current strength of this system, respectively. The shear stress acting on each slip system is calculated by:

$$\tau^{\alpha} = P^{\alpha} : \Psi \tag{1.15}$$

where Ψ is the Kirchoff stress. The Jaumann rate of Kirchoff stress ($\overset{\nabla}{\Psi}$) is related to the elastic part of the rate of deformation ($\dot{D}^{el}$) and the elastic stiffness tensor ($\mathbb{C}$) as:

$$\overset{\nabla}{\Psi} = \mathbb{C} : \dot{D}^{el} \text{ where } \overset{\nabla}{\Psi} = \dot{\Psi} - \dot{\Omega}^{el}\,\Psi + \Psi\dot{\Omega}^{el} \tag{1.16}$$

where $\dot{\Omega}^{el}$ is the elastic part of the rotation tensor. The deformation and the rotation rates are correlated to the symmetric and asymmetric parts of the velocity gradient (L) as:

$$\left(\dot{D}^{el} + \dot{D}^{pl}\right) + \left(\dot{\Omega}^{el} + \dot{\Omega}^{pl}\right) = sym(L) + asym(L) \tag{1.17}$$

and the plastic part of the rotation increment is correlated to the plastic shear rate and asymmetric part of the Schmid tensor (W^{α}):

$$\dot{\Omega}^{pl} = \sum_{\alpha=1}^{N^{spl}} W^{\alpha}\dot{\gamma}^{\alpha} \tag{1.18}$$

The velocity gradient is the time derivative of the deformation gradient (F):

$$L = \dot{F}F^{-1} = \dot{F}^{e}F^{e-1} + F^{e}(\dot{F}^{p}F^{p-1})F^{e-1} \tag{1.19}$$

where F^{e} and F^{p} are the elastic and plastic parts of the deformation gradient, respectively. Assuming the plastic slip does not cause any lattice reorientation, the deformation gradient is found by:

$$F_{ij} = \frac{\partial x_i}{\partial x_j} \tag{1.20}$$

x_i is the displacement field in the current configuration, and x_j is the displacement field in the previous configuration.

1.6 Thesis Overview

Chapter 1 of this thesis provides a summary of the motivation and objective of the thesis, as well as the experimental and numerical techniques used throughout this thesis. Chapter 2 is the first article which discusses the characterization of residual stresses in pure Zr in 3D using 3D-XRD and CPFE. Chapter 3 provides an intensive microstructural and texture analysis of neutron irradiated and unirradiated Zr-2.5Nb specimens using EBSD. Chapter 4 discusses the development of the localized residual stresses in the neutron irradiated and unirradiated specimens. Chapter 5 provides a summary of the conclusions made from each chapter and provides recommendations for future work.

1.7 References

[1] IAEA, “Assessment and management of ageing of major nuclear power plant components important to safety: CANDU reactor assemblies,” *Significance*, 2001.

[2] R. D. Page, “Canadian power reactor fuel,” *AECL Rep. 5609*, 1976.

[3] G. L. Brooks and E. G. Price, “Fuel channel performance,” 1988.

[4] V. Perovic *et al.*, “Microstructural and microchemical studies of Zr-2.5Nb pressure tube alloy,” *J. Nucl. Mater.*, 1993, doi: 10.1016/0022-3115(93)90087-F.

[5] H. Abdolvand, “Progressive modelling and experimentation of hydrogen diffusion and precipitation in anisotropic polycrystals,” *Int. J. Plast.*, 2019, doi: 10.1016/j.ijplas.2018.12.005.

[6] IAEA, “Assessment and management of ageing of major nuclear power plant components important to safety: CANDU pressure tubes,” 1998.

[7] R. A. Holt, “In-reactor deformation of cold-worked Zr-2.5Nb pressure tubes,” *J. Nucl. Mater.*, 2008, doi: 10.1016/j.jnucmat.2007.02.017.

[8] H. F. Poulsen, X. Fu, E. Knudsen, E. M. Lauridsen, L. Margulies, and S. Schmidt, “3DXRD - Mapping grains and their dynamics in 3 dimensions,” in *Materials Science Forum*, 2004, doi: 10.4028/www.scientific.net/msf.467-470.1363.

[9] K. Louca, “THREE DIMENSIONAL CHARACTERIZATION OF DEFORMATION TWINS USING,” *Electron. Thesis Diss. Repos. 6374. https//ir.lib.uwo.ca/etd/6374*, 2019.

[10] O. Engler and V. Randle, *Introduction to Texture Analysis: Macrotexture, Microtexture and Orientation Mapping*. 2010.

[11] W. Massa, *Crystal Structure Determination*. 2004.

[12] R. A. Schwarzer and J. Hjelen, “Backscattered Electron Imaging with an EBSD Detector,” *Micros. Today*, 2015, doi: 10.1017/s1551929514001333.

[13] A. J. Wilkinson, G. Meaden, and D. J. Dingley, “High-resolution elastic strain measurement from electron backscatter diffraction patterns: New levels of sensitivity,” *Ultramicroscopy*, 2006, doi: 10.1016/j.ultramic.2005.10.001.

[14] T. B. Britton and A. J. Wilkinson, “Measurement of residual elastic strain and lattice rotations with high resolution electron backscatter diffraction,” *Ultramicroscopy*, 2011, doi: 10.1016/j.ultramic.2011.05.007.

[15] R. J. Asaro, “Micromechanics of Crystals and Polycrystals,” *Adv. Appl. Mech.*, 1983, doi: 10.1016/S0065-2156(08)70242-4.

[16] H. Abdolvand, “MULTI-SCALE MODELING AND EXPERIMENTAL STUDY OF DEFORMATION TWINNING IN HEXAGONAL CLOSE-PACKED MATERIALS,” *Queen’s Grad. Theses Diss. Dep. Mech. Mater. Eng. Grad. Theses*, 2012.

[17] R. Hill, “Generalized constitutive relations for incremental deformation of metal crystals by multislip,” *J. Mech. Phys. Solids*, 1966, doi: 10.1016/0022-5096(66)90040-8.

[18] R. Hill and J. R. Rice, “Constitutive analysis of elastic-plastic crystals at arbitrary strain,” *J. Mech. Phys. Solids*, 1972, doi: 10.1016/0022-5096(72)90017-8.

[19] R. J. Asaro and A. Needleman, “Overview no. 42 Texture development and strain hardening in rate dependent polycrystals,” *Acta Metall.*, 1985, doi: 10.1016/0001-6160(85)90188-9.

2 Measurement and modeling of micro residual stresses in zirconium crystals in three dimensions

Abstract

The performance of the zirconium alloys used in nuclear reactors can be affected by the state of the residual stresses that develop during manufacturing of the reactor core components. In this paper, the residual stresses within individual grains of a textured α-zirconium polycrystal are investigated. For this purpose, three-dimensional synchrotron X-ray diffraction is used to measure elastic strain tensor, center-of-mass (COM), orientation, and stress tensor of more than 11000 grains in a zirconium sample. The grain measured COMs and orientations are used to reconstruct the 3D microstructure of the sample using the weighted Voronoi tessellation technique. The microstructure is subsequently imported into Abaqus to simulate the experiment using a crystal plasticity finite element model. The state of the thermal residual stresses that develop during slow cooling from 700 °C, and those that develop after unloading from 1.2% applied tensile strain are discussed. It is shown that both thermal and mechanical micro residual stresses, and their variations within a grain, are correlated with the grain size. Also, due to strong anisotropy of the single crystal, residual stresses are significantly affected by the configuration of local grain neighborhood.

2.1 Introduction

Zirconium (Zr) and its alloys have been widely used in the core of nuclear reactors due to their good mechanical properties and high neutron transparency. The most common form of Zr is the α-phase which has hexagonal close-packed (HCP) crystal structure with high elastic, thermal, and plastic anisotropy. One of the main challenges of using Zr in light or heavy water reactors is its susceptibility to formation of zirconium hydrides. During the normal operation of a nuclear reactor, hydrogen from water can diffuse into the Zr lattice. At lower temperatures, the solubility limit of hydrogen in Zr reduces, resulting in the formation of zirconium hydride. This is a brittle phase with a very low fracture toughness

affecting the life-span of core components. It has been suggested that formation of hydrides is affected by the state of stresses at the grain boundaries and the stress variation within the grain [1]. More importantly, it has been suggested, that grain-level thermal residual stresses that develop during manufacturing of zirconium nuclear pressure tubes can affect their response against hydrogen diffusion and hydride formation [2]. As such, this paper focuses on characterizing such localized stresses in α-Zr crystals.

Different diffraction techniques are used to measure stresses in Zr-alloys. For example, neutron diffraction was used to measure internal lattice strains developed during uni-axial deformation of Zircaloy-2 [3]. In this experiment, the average stress within families of grains, that diffract an incident beam, is measured. Such measurements are valuable as the effects of load partitioning on deformation mechanism at the meso-scale can be studied; however, stress development within individual grains cannot be measured due to resolution limits of the method. A few experimental techniques are currently available for measuring grain-level stresses. Laue micro-diffraction is one of those techniques, which was used, for example, to measure lattice curvature in fatigued copper [4]; however, in Laue micro-diffraction technique, only a few grains can usually be examined. Three-dimensional synchrotron X-ray diffraction (3D-XRD) is another technique that provides grain-level stress tensor [5, 6, 7, 8]. With 3D-XRD, the center-of-mass position (COM), relative volume, average orientation, average elastic strain, and stress of individual grains in a polycrystal can be measured. For instance, this technique was used to measure the evolution of stress in twin and parent pairs in Zircaloy-2 [9, 10] and magnesium alloys [11, 12]. Furthermore, 3D-XRD was recently used to study deformation-induced grain orientation spread and the possible effects of grain-grain interactions on the activation of various slip systems in steel [13, 14]. Since the average stress and orientation for many grains are measured, normally the variation of stress within a grain is missed. For capturing such variations, high resolution electron backscatter diffraction (HR-EBSD) can be used. HR-EBSD has been used to study residual stress field close to grain boundaries [15, 16, 17]; however, due to low penetration depth of electrons, such variations can only be measured at the sample surface.

Various numerical techniques have been used to simulate stress development in polycrystals at different length scales. For simulating meso-scale stresses, crystal plasticity has been employed in various frameworks including, finite element [18, 19, 20], self-consistent [21, 22, 23], and fast Fourier transformation [24, 25, 26]. Crystal plasticity is a set of constitutive equations that describes plastic deformation by the movement of dislocations on a slip plane in the slip direction [27]. This technique has been successfully used for modelling plastic deformation by slip [28, 29] and twinning [30, 31, 32]. Also, it has been used to model damage nucleation at or close to grain boundaries [33, 34], and to model non-Schmid effects in nickel based superalloys [35]. Advances in the field have led to the development of strain gradient CPFE models to study formation of slip bands and capture non-local effects [36, 37, 38].

In this study, the state of the residual stresses in Zr crystals are investigated using CPFE numerical modeling and 3D-XRD experimental measurement. Firstly, the steps required for extracting grains stress and strain tensors, COMs, orientations, and volumes using 3D-XRD are described. Several codes are developed to reconstruct grain shapes based on their measured COMs, and relative volumes. The simulated microstructure is subsequently imported into a CPFE model to simulate thermal and mechanical residual stresses. The results of the CPFE model are compared against measured values to understand the nature and source of such stresses. The effects of sample texture on the reported trends are subsequently studied.

2.2 Experimental Method

2.2.1 Sample

A large bar of CPZr with the composition shown in table 2.1 was first annealed at 700°C in an Argon gas environment to prevent oxide layer formation and then air cooled to relieve residual stresses from manufacturing. A dog-bone sample was then cut from the bar such that the sample tensile axis coincided with the original bar diameter. To reduce the effects of machining, the sample was then mechanically polished down to 4000 grit followed by polishing with colloidal silica solution. To reduce the effects of the surface damage on the quality of the collected diffraction patterns, the sample was finally electro-polished for 45

seconds at 25 V in a solution of 10% perchloric acid and 90% methanol at -30°C. An example of the EBSD map measured for the sample is shown in Figure 2.1(a). The coordinate system used in this paper is shown in Figure 2.1(b) where the z-axis coincides with the original bar diameter and the loading direction, the x-axis points into the sample thickness along the incident X-ray beam direction, and the y-axis is given by the cross product of the other two which coincided with the longitudinal axis of the original bar. The 3D-XRD measured pole figure of the sample is shown in Figure 2.1(c). The (0002) pole figure shows that most of the grains have their c-axis oriented towards the x-axis with lesser grains oriented towards the z-axis.

Table 2.1 Chemical composition of the CPZr sample [2]. Numbers are given in ppm

Zr	C	Hf	Fe	Cr	N	O	H
Balance	**250**	**2500**	**200**	**200**	**100**	**1000**	**10**

2.2.2 3D-XRD experiment

The experiment was conducted at the ID-11 of the European Synchrotron Radiation Facility (ESRF), Grenoble, France. The sample was mounted on an Admet tensile rig that applies load uniaxially. The macroscopic applied load was measured by a load cell attached to the tensile rig while the macroscopic strain was measured using two different methods: (a) by tracking two silver wires glued to the sample and determining their precise position using the incident x-ray beam and (b) by digital image correlation tracking changes in the position of the wires using optical images. The sample was deformed under strain-control at an applied strain rate of 2.64×10^{-5} s^{-1}. Diffraction measurements were conducted at four different steps: preload, onset of plasticity (ε=0.59%), maximum applied strain of ε=1.2%, and finally unload. For the preload step, the sample was firstly aligned to ensure that the whole cross section would be immersed in the X-ray beam throughout the rotation steps; then, it was pre-loaded to 7 MPa for collecting diffraction patterns. For the next two steps, the sample was initially deformed to the prescribed strains. For the last step, the sample was unloaded to 10 MPa using the same strain rate. At each measurement step, after aligning the sample, the center of the probed volume was re-calculated by determining the current position of the silver wires and applying the necessary movements in the z-direction to follow the same volume. The first and last steps are the two steps where thermal and

mechanical residual stresses were measured, respectively, while the middle two steps were used to ensure that evolution of stress at the grain level was captured in the CPFE model.

At each loading step, diffraction patterns were acquired using a monochromatic X-ray beam with the energy of 78.39 keV. In order to measure the state of the deformation in 3D, the sample was rotated about the z-axis. The sample and the loading stage were firstly rotated from −234.5 to −125.5°, and then from −54.5 to 54.5° both with the rotation step of 0.25°. The exposure time for collecting diffraction images with 2048 × 2048 pixels was 0.25 s for each rotation step. Once diffraction patterns were measured for one layer, the sample was moved along the z-axis by 25μm so that measurement for the next layer could be conducted. This process was repeated until 15 layers of the sample were probed, i.e. a 0.375 mm length of the sample gauge was covered. The post-processing of the measured data was mainly done by the use of ImageD11 and the subroutines embedded into Fable (https://sourceforge.net/p/fable/wiki/Home/). Full description of this procedure is given in [39].

Table 2.2 Details of the 3D-XRD experiment

		Measured macro stress (MPa)	Number of grains	Average Number of peaks per grain	Average error for measured positions (μm)			Grain weighted-average stress with estimated errors (MPa)					
Step	**Applied strain (%)**				Δx_c	Δy_c	Δz_c	σ_{xx}	σ_{yy}	σ_{zz}	σ_{xy}	σ_{xz}	σ_{yz}
Preload	0.0	7	11247	102	±5.4	±3.2	±1.4	-20 ±27	8 ±19	2 ±16	-1 ±4	-2 ±5	2 ±7
Onset of plasticity	0.59	258	10677	102	±5.5	±3.3	±1.4	-23 ±27	11 ±20	249 ±17	-2 ±4	2 ±5	1 ±7
Plastic zone	1.2	270	8869	99	±6.7	±4.0	±1.7	-24 ±33	13 ±24	264 ±20	-2 ±5	2 ±7	2 ±8
Unload	NA	10	9013	98	±6.7	±4.0	±1.7	-28 ±33	9 ±24	2 ±21	0 ±5	-2 ±7	1 ±8

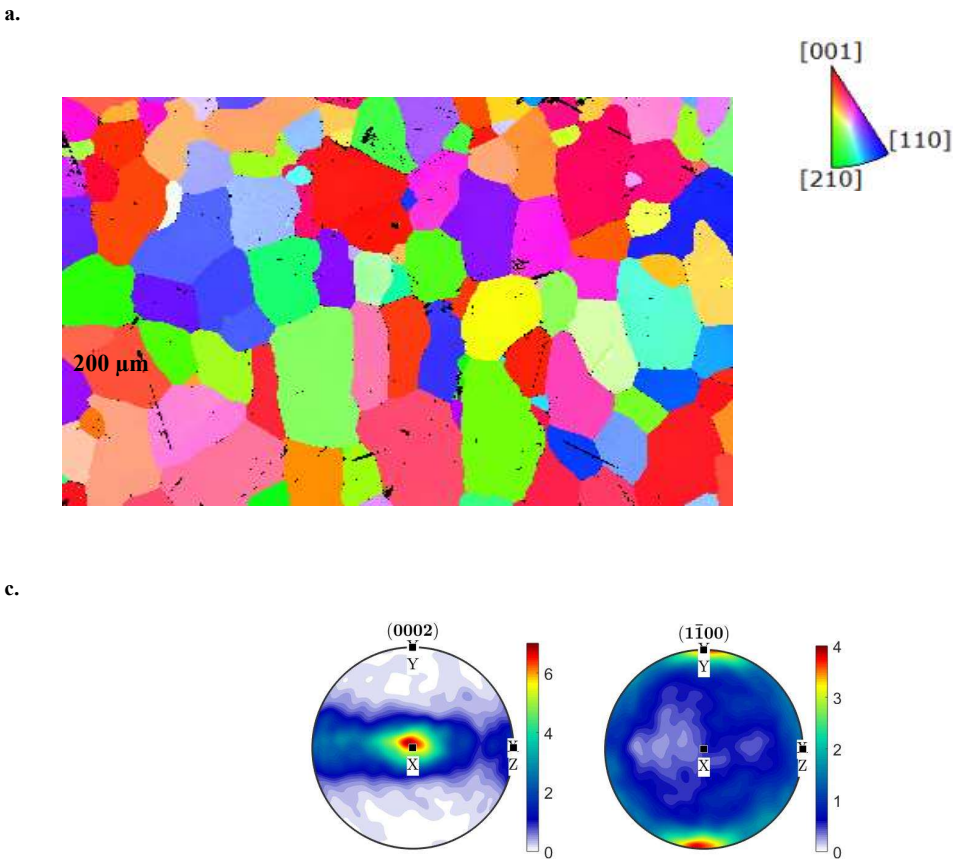

Figure 2.1 (a) an EBSD map of the undeformed sample with the color legend given in the right hand side of the figure. Colors are coded with respect to inverse pole figure z. (b) The sample used in 3D-XRD experiment with the lab coordinate system shown in the bottom of the picture; z-axis is the loading direction and the sample gauge length is 20 mm. (c) The (0002) and (1$\bar{1}$00) measured pole figures from 3D-XRD. Scales are given in multiples of random distribution. (d) Test set-up.

2.3 Crystal Plasticity Simulations

2.3.1 Input model

The measured COMs and relative volumes of the grains were used to simulate grain shapes and import the simulated microstructure into the Abaqus finite element solver. This was done by calculating the "real" physical volume of each grain in the scanned volume, assuming that grains are space-filling, and no grain was missed during the analysis of the 3D-XRD data. With these assumptions, the 3D-XRD measured relative volumes can be multiplied by the dimensions of the probed volume to get the "real" volume of each grain. Grain volumes and the measured COMs were subsequently used to simulate grain shapes using the weighted Voronoi tessellation technique described in [12].

Surface stresses may develop during machining, mechanical polishing, or mounting of the sample on the tensile rig. To avoid such effects, grains located within 100 microns of the free surfaces were removed, i.e. a subset of grains were imported into the Abaqus FE solver. These grains are located in the center of the probed volume and fall into a cube of 200 μm side meshed with a step size of 4 μm and has 50 x 50 x 50 elements that cover 1038 grains as shown in Figure 2.2(a). The same cube was also meshed at a step size of 5 and 17 μm to check the convergence of the FE results. These three models are called S4, S5, and S17, respectively. The simulation cube was then discretized using C3D8 elements. At this stage, the position of each element in the cube was substituted into Eq. 1 for grain assignment [12]:

$$C_i = \left\{ X \in R^d \middle| \|X - s_i\|^2 - w_i^2 < \left\|X - s_j\right\|^2 - w_j^2, i \neq j \right\} \quad (2.1)$$

Where X is the position vector of the element in the cube, s_i is the position vector of the seed point of the grain i, and w_i is the radius of the same grain. For determining the seed point of each grain, Eq. 1 is solved in two steps. In the first step, s_i is replaced by the measured COM_i of the grain G_i. This result in a new COM_b for G_i which does not necessarily coincide with the actual measured COM_i. In the second iteration, s_i is set equal to $2COM_b$- COM_i. It is shown that the second iteration provides a much better estimation of grain boundaries [40]. The model with its corresponding texture is illustrated in Figure

2.2. Comparison of the pole figures for the simulated cube (Figure 2.2(b)) with those measured experimentally for the larger probed volume (Figure 2.1(c)) indicate that the overall texture is well captured in the CPFE model. Further, in Figure 2.2(c), the relative volume of each grain in the simulated microstructure is compared to those measured. Results for a second case where Voronoi tessellation is used is also shown. For this case the weight function (w_i and w_j) in Eq. 1 was simply set to zero and grains COMs were used as seed points. It can be seen that the relative volume from weighed Voronoi are much closer to those measured experimentally.

For simulating the experiment, the model was firstly cooled down to room temperature in the absence of any external load (zero net force in all directions) to simulate the development of thermal residual stresses during heat treatment. In the second step, the sample was deformed at the same strain rate that was used in the experiment. Periodic boundary conditions were applied on each of the surfaces of the simulation cube following the method described in [41]. A tensile elongation was applied along the z-axis, while in the transverse x and y axes the contraction was left free, and the model was allowed to relax to zero transverse net force.

A crystal plasticity user material (UMAT) subroutine for the Abaqus finite element solver that was developed by [41] was used for simulating deformation of each grain. A brief description of the key equations used in the subroutine is given here; comprehensive explanations are given elsewhere [41]. At the beginning of each time increment, Abaqus FE solver provides strain and time increment data into the UMAT, in which the new state of stress, solution dependent state variables, and the Jacobian matrix ($\frac{\partial \Delta\sigma}{\partial \Delta\varepsilon}$) are calculated. The total strain increment ($\Delta\varepsilon$) can be decomposed to the elastic ($\Delta\varepsilon^{el}$) and plastic ($\Delta\varepsilon^{pl}$) parts. For the CPZr sample used in this study, the c-axis of the HCP crystals are mostly in compression, and since the deformation is applied to small strains, the effects of twinning is ignored; hence, the plastic strain rate can be calculated from the slip rate ($\dot{\gamma}^{\alpha}$) :

$$\dot{\varepsilon}^{pl} = \sum_{\alpha=1}^{N^{spl}} P^{\alpha}\dot{\gamma}^{\alpha} \qquad (2.2)$$
$$P^{\alpha} = sym(S^{\alpha}) \; where \; S^{\alpha} = d^{\alpha} \otimes n^{\alpha}$$

In which P^{α} is the symmetric part of the Schmid tensor (S^{α}) for the slip system α, d^{α} is the direction of the slip and n^{α} is the normal to the slip plane. The slip rate of the slip system α is calculated using Eq. 3 [27]:

$$\dot{\gamma}^{\alpha} = \dot{\gamma}_0 \left|\frac{\tau^{\alpha}}{g^{\alpha}}\right|^{n} sign\left(\frac{\tau^{\alpha}}{g^{\alpha}}\right) \tag{2.3}$$

where $\dot{\gamma}_0$ is a reference shear strain rate, and n is a constant that controls rate dependency. The value of $\dot{\gamma}_0$ and n are provided in table 2.3. τ^{α} and g^{α} are the resolve shear stress on the slip system α and the current strength of this system, respectively. At room temperature, plastic deformation of CPZr is mostly controlled by prism $\langle 11\bar{2}0\rangle$, basal $\langle 11\bar{2}0\rangle$, and pyramidal $\langle 11\bar{2}3\rangle$ slip systems [3, 41]. The CRSS values used in this study are 82 MPa, 109 MPa, and 287 MPa, respectively, with no further hardening. These CRSS values were established by scaling down those reported by [42] from micro-cantilever testing of the same batch of CPZr to allow for a change in strain rate and the stress relaxation occurring during the 3D-XRD experiment. This model is called "relaxed model". In addition, a second set of crystal parameters was used to study the effects single crystal hardening and the displacement-hold on the calculated residual stresses for the unload step. These parameters were extracted by [41] for α-Zr and are provided in the supplementary file (Table S1). This model is called "displacement-hold". In the supplementary file, it is shown that the difference between the "relaxed" and "displacement-hold" models for the thermal and mechanical residual stresses are negligible. Hence, in all simulations presented in this paper, the first set of parameters are used with the "relaxed model".

Table 2.3 single crystal parameters used for S4, S5, and S17 models

	N	$\dot{\gamma}_0$ (s^{-1})	CRSS (GPa)
Prism	**20**	**3.5×10^{-4}**	**0.082**
Basal	**20**	**3.5×10^{-4}**	**0.109**
Pyramidal	**20**	**1.0×10^{-4}**	**0.287**

The shear stress acting on each slip system can be calculated from the Kirchoff stress (Ψ) through the following equation:

$$\tau^{\alpha} = P^{\alpha} : \Psi \tag{2.4}$$

The Jaumann rate of Kirchoff stress ($\overset{\nabla}{\Psi}$) is related to the elastic part of the rate of deformation ($\dot{D}^{el}$) and the elastic stiffness tensor ($\mathbb{C}$) as:

$$\overset{\nabla}{\Psi} = \mathbb{C}: \dot{D}^{el} \text{ where } \overset{\nabla}{\Psi} = \dot{\Psi} - \dot{\Omega}^{el}\,\Psi + \Psi\dot{\Omega}^{el} \tag{2.5}$$

where $\dot{\Omega}^{el}$ is the elastic part of the rotation tensor. The deformation and the rotation rates are correlated to the symmetric and asymmetric parts of the velocity gradient (L) as:

$$\left(\dot{D}^{el} + \dot{D}^{pl}\right) + \left(\dot{\Omega}^{el} + \dot{\Omega}^{pl}\right) = sym(L) + asym(L) \tag{2.6}$$

and the plastic part of the rotation increment is correlated to the plastic shear rate and asymmetric part of the Schmid tensor (W^{α}):

$$\dot{\Omega}^{pl} = \sum_{\alpha=1}^{N^{spl}} W^{\alpha}\dot{\gamma}^{\alpha} \tag{2.7}$$

The elastic modulus of the single crystal CPZr used in this study is the one determined by [43]: C_{11}=143.5 GPa, C_{33}=164.9 GPa, C_{12}=72.5 GPa, C_{13}=65.4, GPa, and C_{44}=32.1 GPa.

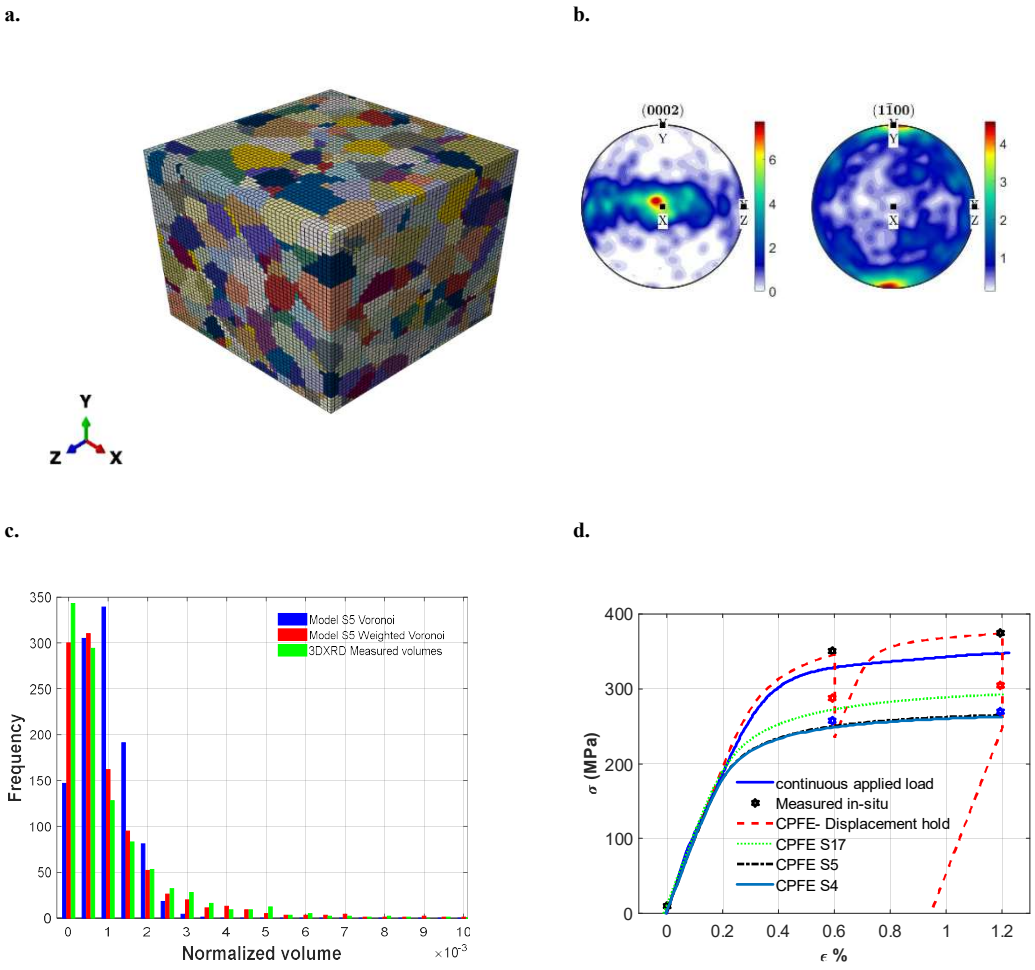

Figure 2.2 (a) The modelled microstructure that was imported into a finite element solver for simulating 1038 grains. Random colors are assigned to elements to distinguish different grains. (b) The corresponding pole figure of the modelled microstructure. (c) Comparison between the measured volumes of the grains and the simulated ones using Voronoi and weighted Voronoi tessellation. (d) Comparison between the average stress-strain curves calculated for each model with the experimentally measured ones.

2.4 Results

In the following sections, stresses and strains are given in the global coordinate system shown in Figure 2.1(b) where x, y, and z coincide with the X-ray beam (11), transverse (22), and the loading (33) directions, respectively. σ_H is used to represent hydrostatic stress. In calculating propensities from the 3D-XRD experiments, the measured volume fraction of grains are taken into account to provide a like-to-like comparison with the obtained values from CPFE simulations. Also, in all of the relevant figures, β represents the angle between the Basal Plane Normal and the loading direction. Neighboring grains are identified after meshing the volume and a grain neighbor is defined as the one that shares at least one element surface with another grain.

2.4.1 3D-XRD vs. CPFE results

The macroscopic stress-strain curve for CPZr is shown in Figure 2.2(d). In this figure, the continuous stress strain curve that was measured non-stop is compared against the one measured during 3D-XRD experiment. For each applied strain, there are three stresses that were measured during the 3D-XRD experiment; these three values correspond to the initial measured stress at a given strain, the stress measured after the sample alignment (~30 mins hold at that strain level) and right before the start of diffraction measurement, and the stress measured at the end of the measurement. For the preload and unload steps, the last two stresses coincide with the initial measured stresses as there was no evident stress relaxation. The initial measured stresses are close to the ones measured during continuous experiment, although they are slightly higher as the strain rate during the 3D-XRD experiment ($2.64\times10\text{-}5\ s^{-1}$) was a little higher than that of the continuous experiment ($1\times10\text{-}5\ s^{-1}$). The macroscopic stresses measured at the end of each loading step are very close to the stresses determined from the 3D-XRD measurements using the weighted volume average of the stresses measured for each grain. Further, it is shown in Figure 2.2(d) that CPFE results, at macro-level, are converged for S5 and S4 models. The results of model S4, however, is used throughout this paper as more elements are assigned to each grain. Further analysis of calculated stresses for each grain indicate that grain average stresses are converged for both model S5 and S4; however, to capture “true” stresses at the grain boundaries, it is necessary to use higher mesh densities or special element types as discussed by Gonzalez

et al. [44]. As such, for the analysis of stress variations, e.g. stress range, all elements located at the grain boundaries are removed and only the IPs located within grain interiors are used.

The total number of indexed grains obtained at each loading step and number of peaks assigned to each grain are shown in table 2.2. Since the sample was not heavily deformed, there is only a small reduction in the number of peaks per grain. This is also reflected in the estimated errors for the COM and stresses measured for each grain. The distribution of the measured stresses and orientations for each loading step are shown in Figure 2.3, where each grain is represented by a sphere with a volume proportional to the measured volume of the grain. It is shown in Figure 2.3(a) that most of the grains have their c-axis perpendicular to the loading direction. This means that basal and prism are the two main active slip systems. Further, σ_{33} stresses measured at the onset of plasticity and applied stress of 1.2% are generally varying between 100 to 400 MPa, while those measured at the preload and unload vary between -200 to 200 MPa. Since hydrogen diffusion in Zr lattice depends on the state of the hydrostatic stresses, the variation of σ_H at the preload and unload are provided in Figure 2.3(f), and 2.3(g).

The distribution of the grain measured residual stresses as a function of the angle β between the sample z-axis and the crystal c-axis for σ_{33} and σ_{11} at the preload step are shown in Figure 2.4(a) and 2.4(b), respectively. The grain to grain variations in residual stresses are large, despite the anneal and slow cool. Measured stresses vary between -200 and +200 MPa with an overall standard deviation of 52 MPa. Averaging stresses (by grain volume) within each 5° bin in angle β reveals an underlying trend of more σ_{33} tensile stress for grains with the c-axis aligned close to the sample z-axis, and a gradual decrease into a slight compressive stress for grains with c-axis near 90° to the z-axis. CPFE results shown in Figure 2.4(d)-2.4(f) indicate that such trends are due to anisotropy of the coefficient of thermal expansion (CTE) for the HCP crystal which is larger along the c-axis ($\alpha c=10.1\times10–6\ K^{-1}$) than normal to it ($\alpha a=5.3\times10–6\ K^{-1}$). The thermal residual stresses develop as a result of the grain-grain interaction and anisotropy in the elastic modulus and thermal coefficient of expansion.

The volume averaged of 3D-XRD results for the unload step, given in table 2.2, confirm that there is no external loading on the sample. The obvious comparison to make is with the initial state where grains with c-axis within ~15° of the z-axis exhibited tensile residual stress on average of ~50 MPa, but in some cases in excess of 150 MPa (Figure 2.4(a)). By comparison the residual stresses at the end of the test after the tensile deformation are significantly reduced for these hard oriented grains (Figure 2.4(c)) for which the average stress is close to zero, though individual grains have stresses distributed between +100 MPa and 100 MPa. Grains with high β have a slightly compressive σ_{33}, which is similar to the condition before the load-unload cycle. CPFE simulation at unload is shown in Figure 2.4(f)-2.4(g) where a good agreement between CPFE simulation and 3D-XRD measurement was achieved. In the both preload and unload steps, most grains have grain-average stress of zero. In the unload step, the bar graphs broaden showing overall standard deviation of 80.4 MPa reflecting the effects of plastic deformation that occurred in the crystals at 1.2% applied strain. Further analysis of the results shows that at the preload and unload, the hydrostatic stress varies between ±200 MPa with overall standard deviation of 44.9 MPa and 52.8 MPa, respectively.

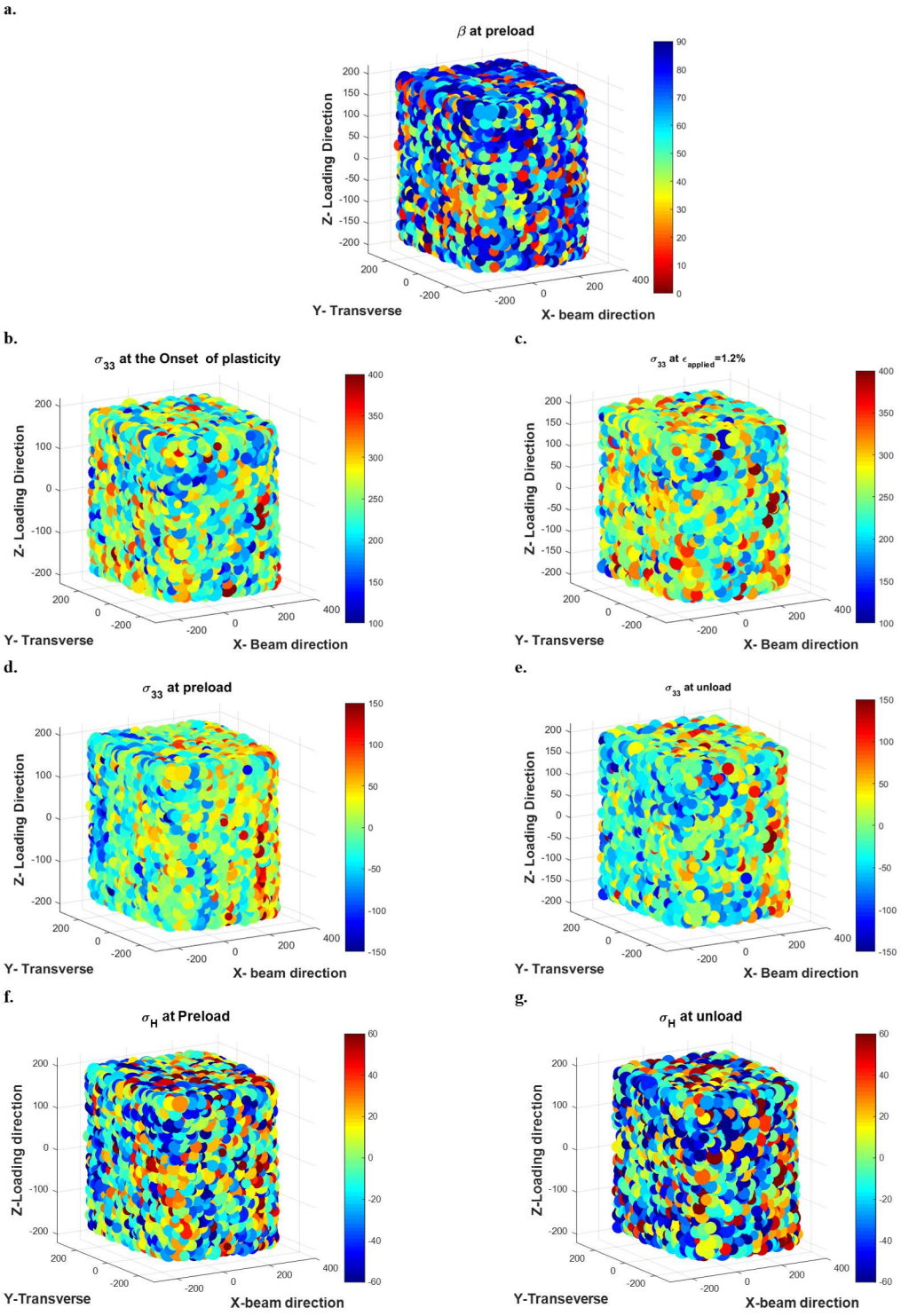

Figure 2.3 Measured stresses and orientations from 3D-XRD experiment: (a) the misorientation between the basal plane normals and the loading direction (β) for preload. Stress in the loading direction at the (b) onset of plasticity (c) applied strain of 1.2%, (d) preload and (e) unload. Hydrostatic stresses at the (f) preload and (g) unload steps.

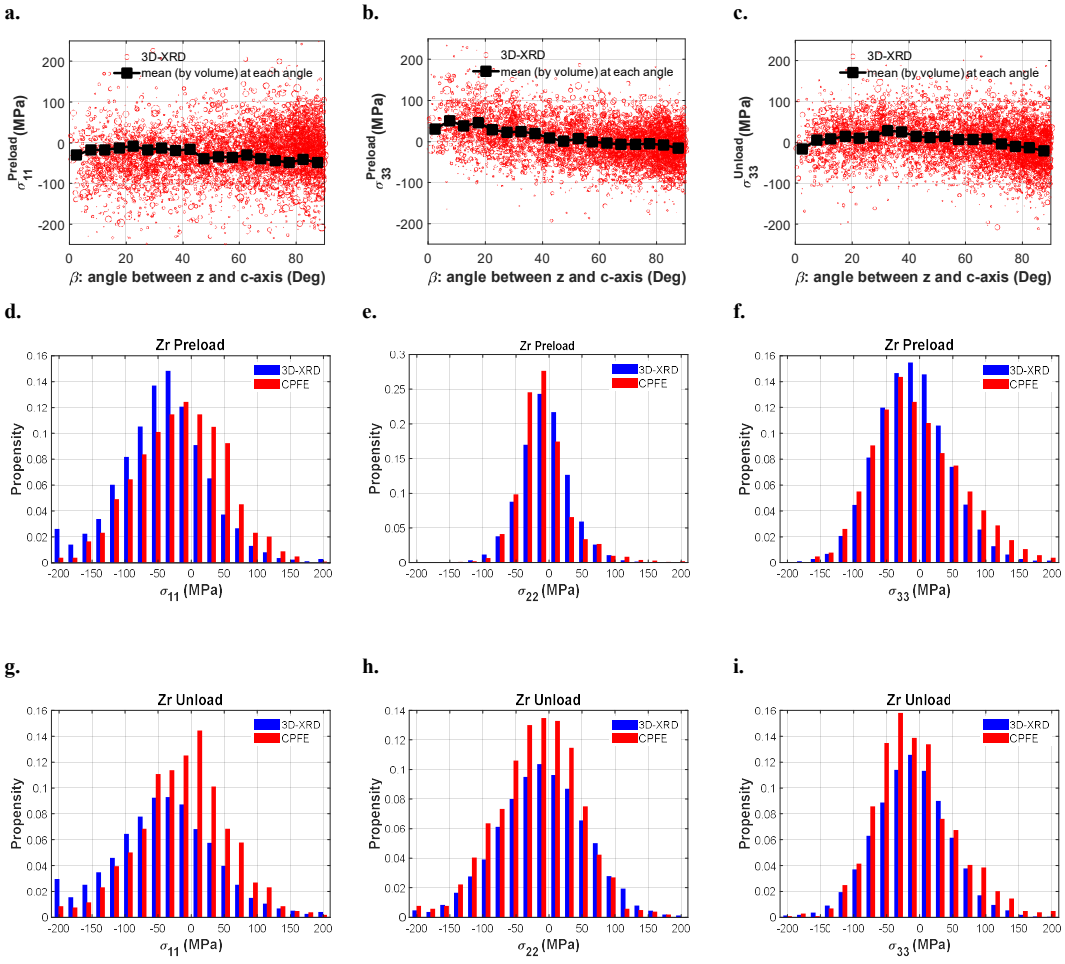

Figure 2.4 Grain measured residual stresses as a function of the angle between the basal plane normals (β) and the loading direction: (a) σ_{33} and (b) σ_{11} at the preload and (c) σ_{33} at the unload. The size of each circle is proportional to the measured volume for each grain. (d) – (i): Comparison between σ_{11}, σ_{22}, and σ_{33} obtained from CPFE and 3D-XRD for the preload and unload steps.

2.4.2 Effects of grain size

In Figure 2.5, the grain-average stress obtained from CPFE and 3D-XRD in the preload and unload steps are plotted against the measured diameters of the grains. In this figure, "o" represents the grain-average stress and grains are grouped based on their diameters with the increment of 5 μm. For each group, the stress magnitude is used to calculate the average stress shown with an "X". The plotted line is fitted using the X values, and the r^2 value of the fitted line is given. It can be seen that, in all scatter plots, the slope of the fitted

line is negative. This indicates that, on average, bigger grains are more likely to experience lower grain-average stresses; however, this does not imply that big grains have lower "local" stresses (see section 5.2). Also, as the diameter increases, stress range for each group decreases. For example, σ_H at preload for grains with dimeter of 10 µm vary between ±200 MPa, but at 60 µm, this range is ±50 MPa. Similar trends were captured at the unload step. The same trends are captured in CPFE results; however, the slopes of the fitted line obtained from CPFE are lower than those obtained from 3D-XRD. One of the factors that affect this slope is the number of grains contributed in each population. In the CPFE model, not all measured grains are simulated, hence, the effects of the grain-grain interactions are underestimated, especially for the grains at the model surface. This is further discussed in section 2.5.2.

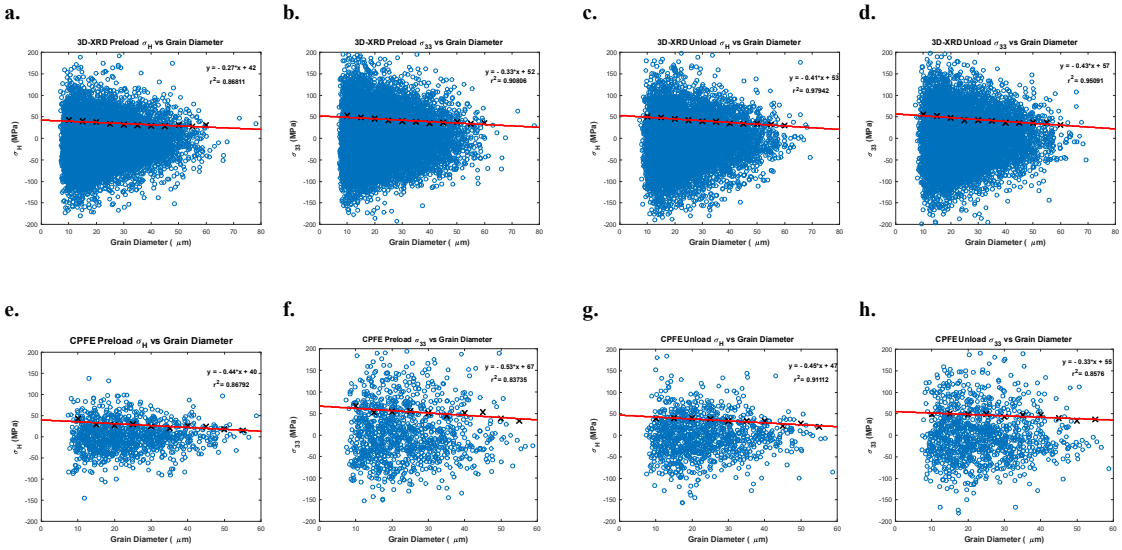

Figure 2.5 Grain average σ_{33} and σ_H as a function of grain diameters: Results from 3D-XRD are shown in the top row and those from CPFE are shown in the bottom row. The first two columns are from preload step and the last two are from unload. The magnitudes of the measured and calculated data are used for data fitting.

2.5 Discussion

Since stress variation within grains can be extracted from CPFE simulations, in this section, the effects of grain size and grain neighborhood on the development of localized stresses and their effects on the observed trends for grain-average stresses will be discussed.

2.5.1 Size effects

CPFE results are used to investigate the variation of stress across individual grains. Two grains that have different diameters are compared. The first grain is the grain number 4329, one of the biggest grains in the simulated population. It has a diameter of 54.5 μm with 8528 integration points (IP). The second grain, grain 3144, is a smaller grain that has a diameter of 28.2 μm and 1520 IPs. Both grains are compared in terms of stress variation within the grain, at the preload and unload steps (Figure 2.6(a)-2.6(f) and table 2.4). In these figures, the elements located at the grain boundaries are removed from the analysis to eliminate the numerical artifacts that might arise from such elements. In this paper, stress range refers to the difference between the highest and lowest calculated stresses from IPs of a grain. For the calculation of stress range, IPs located at the grain boundaries are removed from the analysis. Full width at half maximum (FWHM) of stress is calculated using stresses at each IP. Stress range is an indication of localized stress fields close to grain boundaries while FWHM represent general stress variation within the grain. In table 2.4, it is shown that FWHM of stress components as well as stress range for the bigger grain is generally higher than those of smaller grain, particularly for the unload step. This indicates that the bigger grain can accommodate the sharp stress variations from one side of the grain to another and reduce the stresses from the grain boundaries toward grain interiors; however, for the smaller grain, the effects of stress variations at the grain boundaries is not overcome by the grain size. Such effects can better be seen by dividing the calculated FWHM to the stress range to highlight the ratio between stress variations to stress localization.

Table 2.4 Grain 4329 and 3144 stress values

	Preload				Unload			
	σ_{11}	σ_{22}	σ_{33}	σ_H	σ_{11}	σ_{22}	σ_{33}	σ_H
Grain 4329 (with 8528 IPs)								
FWHM (MPa)	69.9	34.5	52.5	31.4	106.4	105.9	69.6	65.6
Stress range (MPa)	247.1	153.9	254.4	155.2	520.4	334.4	323.8	254.8
FWHM/ Stress range (%)	28.2	22.4	20.6	20.2	20.4	31.6	21.5	25.7
Grain 3144 (with 1520 IPs)								
FWHM (MPa)	86.1	34.6	53.2	30.0	88.8	93.4	64.4	69.5
Stress range (MPa)	181.6	99.6	140.9	101.8	280.9	265.0	242.9	202.8
FWHM/ Stress range (%)	47.4	34.7	37.7	29.5	31.6	35.2	26.5	34.3

These two grains represent an example of many grain combinations that are tested, yet similar trends are observed. The variation of FWHM, stress range, and their corresponding ration as a function of grain size for all of the simulated grains are shown in Figure 2.6(g)-2.6(l). It can be seen that FWHM of σ_{11} and σ_H is weakly correlated with the grain size; however, stress range is significantly affected by the grain size, i.e., bigger grains have higher stress range. This is significant because higher stress gradients may accelerate diffusion of hydrogen atoms [45, 46]. Such sharp stresses at the grain boundaries are caused

by the bigger grain having more neighbors, i.e. grain 4239 has 33 neighbors compared to the 19 neighbors of grain 3144.

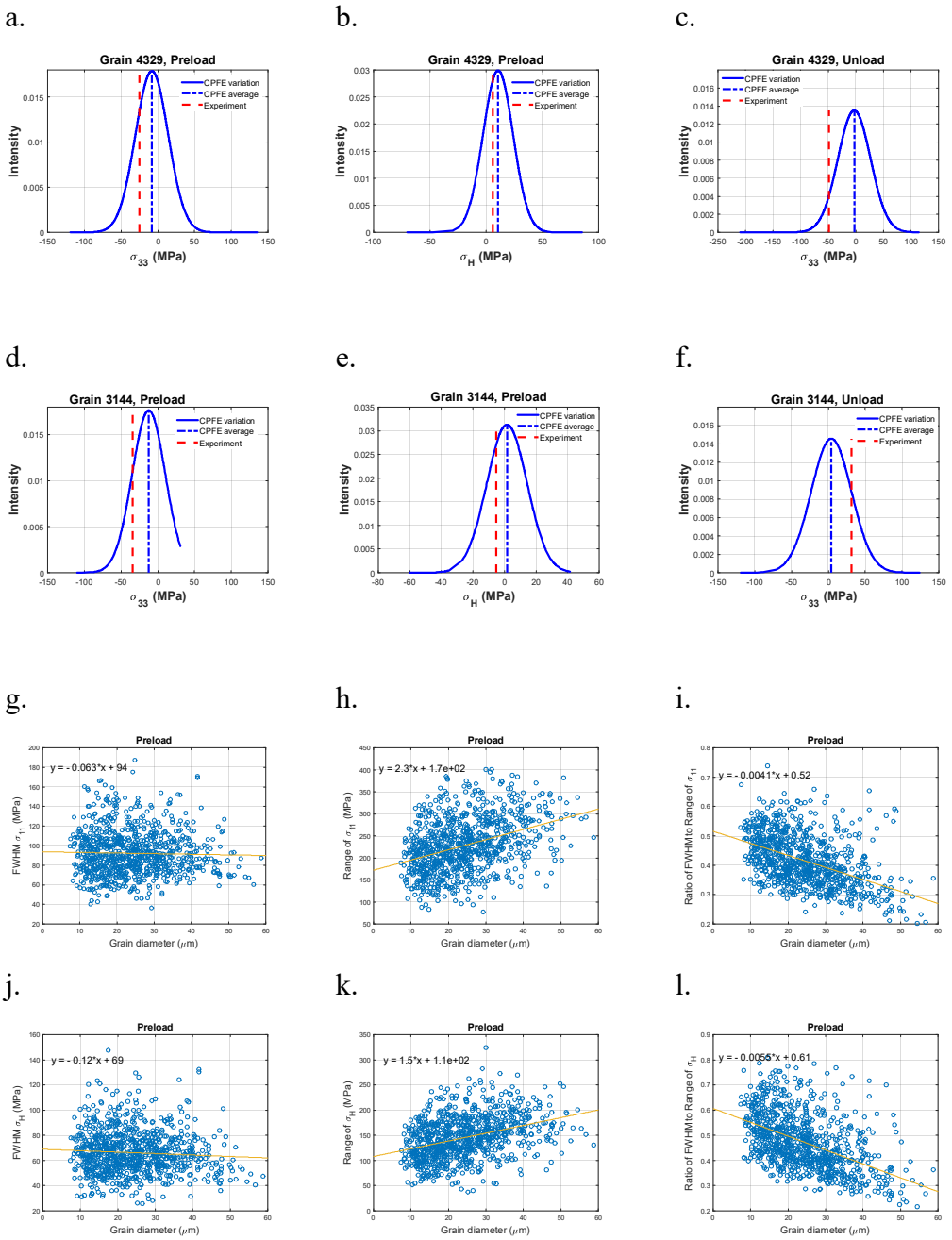

Figure 2.6 Grain-average stresses and stress variations for σ_{11} and σ_H: Results for grain 4329 and 3144 are shown in the first and second rows, respectively. The

calculated full width of half max (FWHM), stress range, and the ratio of FWHM to stress range of (g-i) σ_{11} and (i-l) σ_H.

2.5.2 Effects of neighboring grains

Localized stresses close to grain boundaries and grain-average stresses are very much affected by the grain neighborhood. The effects of grain neighborhood on two different sets of grains are studied here; in the first set, grains are located at the surface of the CPFE model and are called "surface grains". In the second set, the selected grains have no element at the model surface and are called "interior grains". Grain 2309, which lies on the surface of the simulated cube, is examined. This grain has 616 integration points, and 8 of its neighbors are present in the simulated cube, while in the actual specimen it has more than 8 neighbors. Figure 2.7 shows that there is a significant difference between the values calculated by CPFE and those measured with 3D-XRD at the preload step. This is due to missing neighbors and the lack of capturing the "true" grain-grain interaction. Such interactions control how thermal residual stresses develop. These results reveal the importance of materials microstructure in the analysis of residual stresses for anisotropic materials.

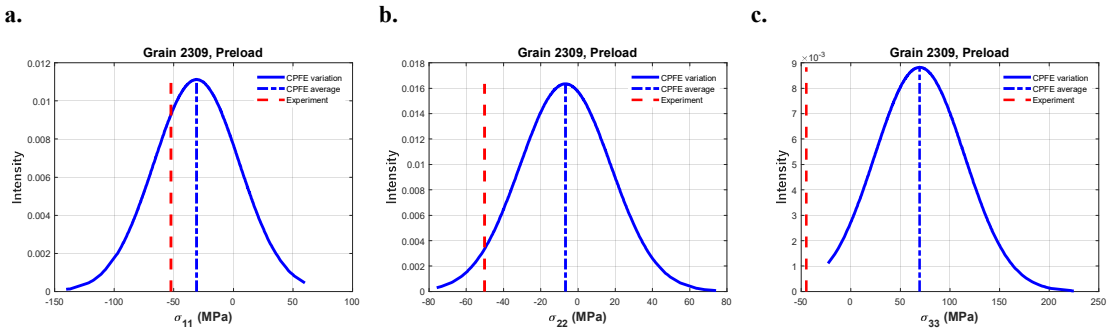

Figure 2.7 Comparison between CPFE and 3D-XRD results for the surface grain 2309: (a) σ_{11}, (b) σ_{22}, and (c) σ_{33}.

Two interior grains with nearly similar diameters were selected for further analysis. The choice of two grains was to only focus on grain neighborhood effects and to minimize the possible size effects. The first grain is grain 5732 which has a diameter of 41 μm, 21 neighbors, and 4232 integration points. The second grain is grain 3492 which has a diameter of 47 μm, 28 neighbors, and 6336 integration points. It is shown in Figure 2.8

that for both cases, the calculated average stresses from CPFE are in much better agreement with the measured ones.

Table 2.5 Grain 5732 and 3492 stress values

	Preload				Unload			
	σ_{11}	σ_{22}	σ_{33}	σ_H	σ_{11}	σ_{22}	σ_{33}	σ_H
Grain 5732 (with 4232 IPs and 21 neighbors)								
FWHM (MPa)	**42.0**	**22.6**	**51.8**	**29.3**	**109.9**	**65.9**	**76.6**	**62.7**
Stress range (MPa)	**226.7**	**91.6**	**170.7**	**114.8**	**395.4**	**306.5**	**257.7**	**253.7**
Grain 3492 (with 6336 IPs and 28 neighbors)								
FWHM (MPa)	**56.8**	**39.4**	**52.3**	**36.5**	**149.6**	**102.7**	**79.1**	**85.1**
Stress range (MPa)	**229.8**	**191.6**	**285.2**	**177.6**	**585.8**	**402.4**	**389.7**	**349.4**

As shown in Figure 2.8 and table 2.5, the stress range and FWHM for σ_{33} and σ_H at preload are higher for the grain with more neighbors (3492). This indicates that higher stresses have developed at the vicinity of grain boundaries. Similarly, for unload step, the grain with more neighbors has higher stresses at the grain boundaries. For this step, in addition to the thermal and elastic anisotropy, stresses are affected by the plastic anisotropy. Higher number of neighbors increases the possibility of having higher misorientation angle with the neighboring grains, resulting in the possibility of having higher stresses developed close to the grain boundaries. The distribution of misorientation between the two investigated grains and their neighbors are shown in Figure 2.9(a) and 2.9(b). Both total and basal plane normal misorientations are plotted. Grain 5732 has a maximum misorientation of 67° with its neighbors, while grain 3492 has a maximum misorientation of 90° which confirms the effects of higher misorientations on the development of higher localized stresses.

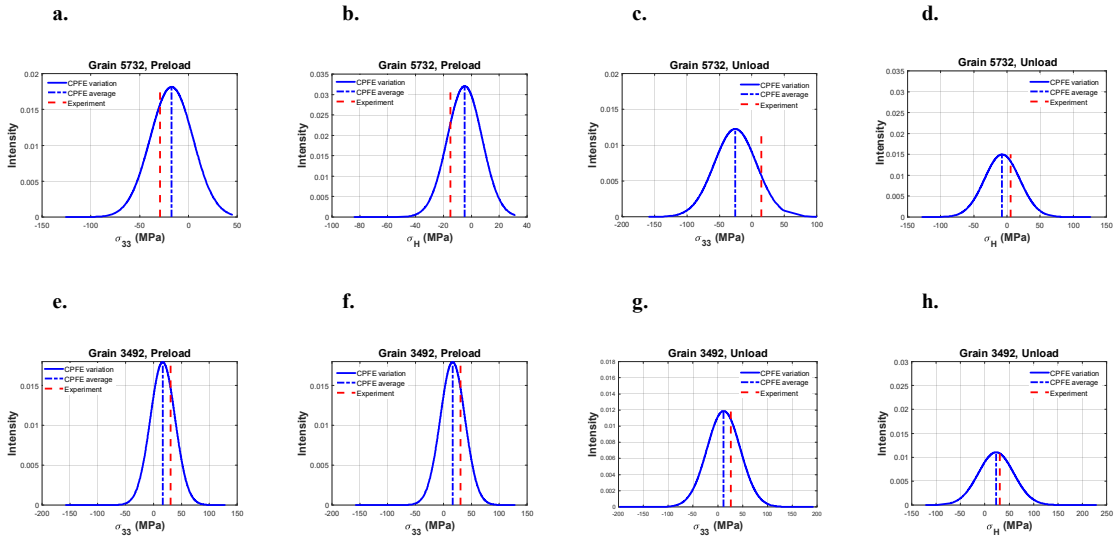

Figure 2.8 Grain-average stresses and stress variations for σ22 and σH: Results for grain 5732 and 3492 are shown in the top and bottom rows, respectively. The first two columns are from the preload step and the last two are from the unload step.

In Figure 2.9(c) and 2.9(d), the calculated hydrostatic (σ_H) and VonMises (σ_{VM}) stresses of each element located at the vicinity of the grain boundary of grain 3492 is plotted. Each point represents the stress averaged over eight integration points of the element, and the values on the x-axis represent the misorientation of the element with the elements of the immediate neighboring grains. Some elements have more than one neighbor, e.g. triple points, therefore, have multiple points on the plot. Generally, there is a huge variation in the magnitude of the stresses, even for the elements of the same grain boundary. Two parameters affect such variations: the type of grain boundary and the grain-neighbor misorientation. To separate the effects of these two parameters, a simple bicrystal model was made where the only variable was the orientation of the front crystal (see Figure 2.9). Only the heat treatment step was simulated by reducing the temperature from 700 °C to the room temperature and applying symmetry boundary conditions on all surfaces to have zero net macroscopic stresses. One crystal was kept at a fixed orientation, while the c-axis of the front crystal was rotated to increase the misorientation from 0° to 90° with 15° increments. The stresses at the center of the grain boundaries at each misorientation are used to generate the lines shown in Figure 2.9(c) and 2.9(d). The trend line shows that the

magnitude of the stresses at the grain boundary simply increase with misorientation. However, the large variation observed in the "real" polycrystal highlights the effects of grain boundary geometry.

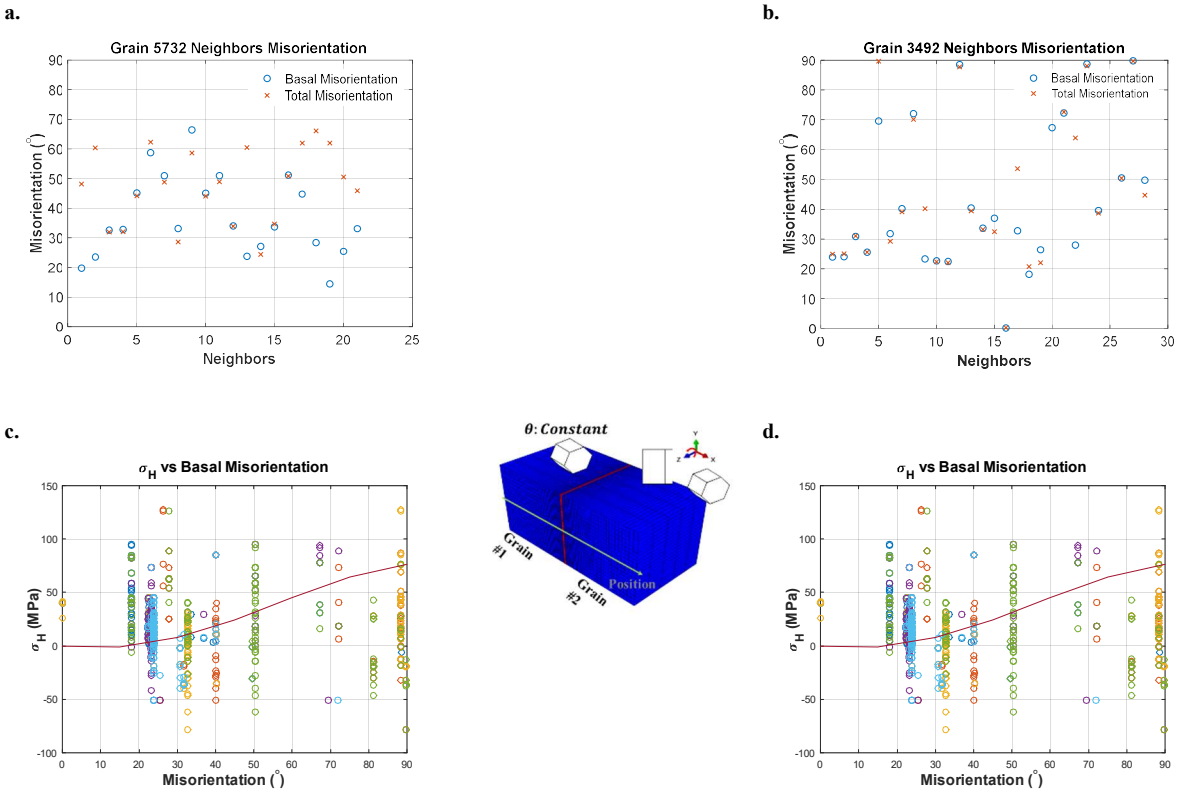

Figure 2.9 The distribution of misorientation of (a) grain 5732 and (b) grain 3492 with their neighbors. CPFE results for grain 3492: the variation of (c) σ_H and (d) σ_{VM} for the element located at the grain boundaries as a function of basal plane misorientation with the immediate neighboring grain. The lines shown in (c) and (d) are for the ideal bi-crystal model shown above.

2.5.3 Effects of Texture

In the previous sections it was shown that grain-grain interactions control the development of thermal residual stresses, particularly those that develop at the vicinity of grain boundaries. Such interactions can be affected by the macro-texture and the combination of the neighboring grains. As such, the effects of macro-texture on the development of thermal residual stresses are discussed in this section. The CPFE input model and applied boundary

conditions are kept the same; however, to generate a random macro-texture, random orientations are assigned to each grain. This texture is shown in Figure 2.10(a). In comparison to the original "textured" model, grain shapes are conserved, but not grain orientations.

In Figure 10(d)-10(f), the distribution of grain-average residual stresses for the "random" model are shown and are compared to those from the "textured" model. The "textured" model has more grains with zero grain-average stresses than the "random" model indicating that the grains of the "random" model are more stressed. The most significant difference is seen in σ_{22}. In the "textured" model, the specimen is textured such that the c-axis of the crystals are oriented towards the x- and z-axis, making the (22) direction elastically and thermally the "softest" direction where the misorientation variation among the neighboring grains is minimum. The "random" model has a wider σ_{22} distribution because the crystals c-axes are randomly distributed along all three directions increasing the mismatch in thermal and elastic properties of neighboring grains, and thus developing a wider distribution of GAS.

In Figure 2.10(g) and 2.10(h), grain-average σ_{33} and σ_H for the "random" model are respectively plotted against grain diameters. Similar to those presented in section 4.2, lines are fitted using the absolute values of σ_{33} and σ_H. It is interesting to see that similar trends are observed for the "random" model. The slope of the fitted lines in Figure 2.10(e) and 2.10(f) are all negative, similar to those calculated in Figure. 2.5(e) and 2.5(f). It can be concluded that for the smaller grains, the localized forces resulting from the grain-grain interactions and strain compatibilities are the dominant factor in the controlling the magnitude of the grain-average stresses. For the bigger grains, the grain area is big enough to counteract such localized forces. To further investigate this, the calculated stresses for the two previously discussed grains, grains 3144 and 3492, are analyzed and the results are summarized in table 2.6. Results from both "random" and "textured" model are provided. The grain-average stress, FWHM, and the stress range from the "random" model are higher than those of "textured" model which further reinforces our conclusion that the grains of a non-textured specimen have higher grain-average stress than a textured specimen. Also, grain-average stress of grain 3144 in the "random" model is increased significantly,

comparing to grain 3492. The volume of Grain 3492 is about four time bigger than grain 3144. This further highlights the conclusion that the grain-average stress of smaller grains is more affected by the localized forces from grain-grain interactions while for the bigger grains, the larger grain area counteracts the effects of the localized forces.

Table 2.6 Stress Values for grain 3144 and grain 3492

	"Original" Model (Textured)				**"Random" Model (Random Texture)**			
	σ_{11}	**σ_{22}**	**σ_{33}**	**σ_H**	**σ_{11}**	**σ_{22}**	**σ_{33}**	**σ_H**
Grain 3144 (with 1520 IPs)								
Grain-average	18.9	0	-34.1	-5.1	37.7	106	33.0	59.0
FWHM	86.1	34.6	53.2	30.0	102.6	103.7	46.8	64.8
Stress range	181.6	99.6	140.9	101.8	250.9	252.4	164.9	160.1
Grain 3492 (with 6336 IPs)								
Grain-average	26.5	-3.5	25.3	16.09	38.8	-13	40.66	22.2
FWHM	56.8	39.4	52.3	36.5	73.6	69.8	73.5	59.2
Stress range	229.8	191.6	285.2	177.6	304.9	300.5	293.1	246.7

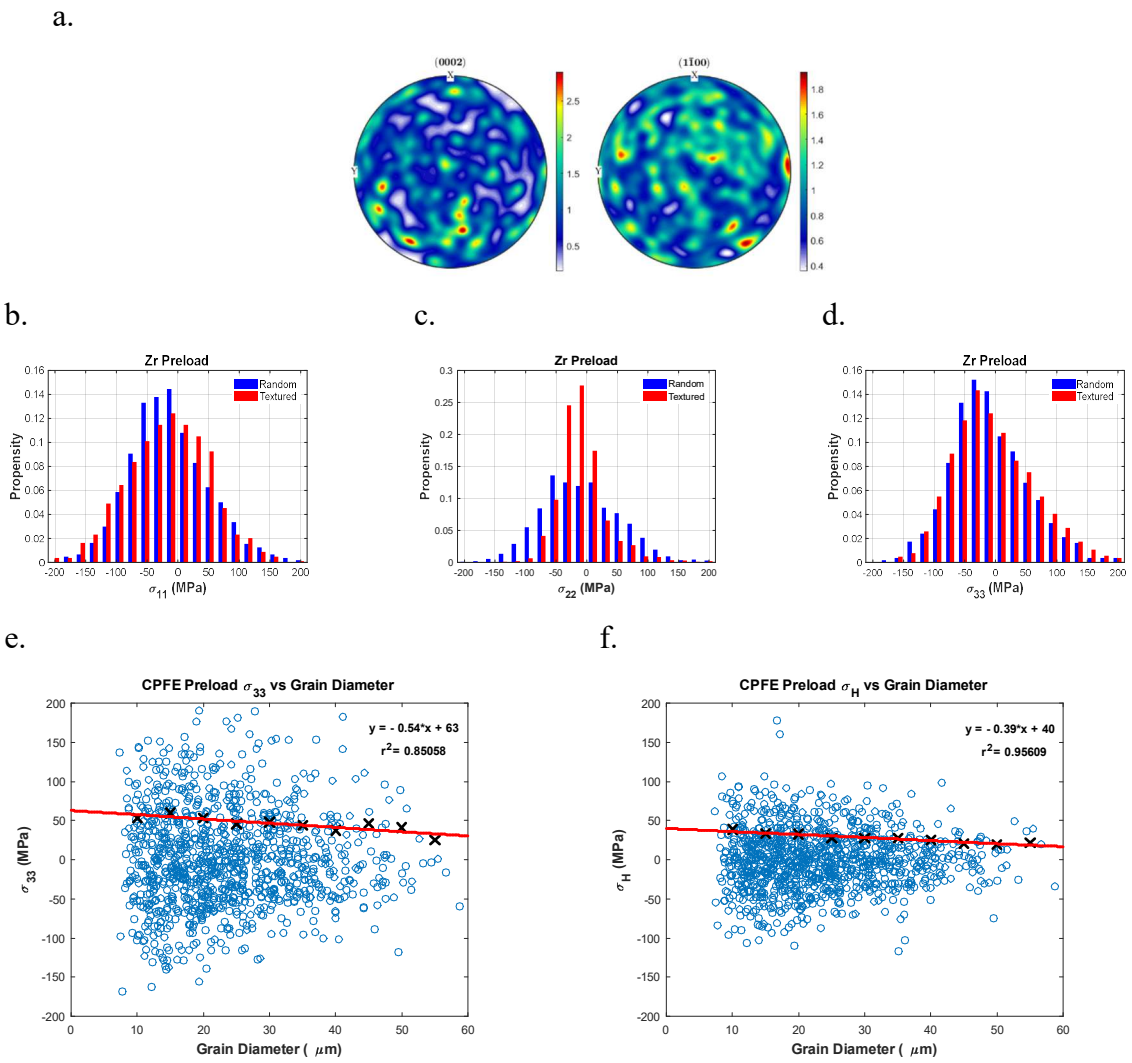

Figure 2.10 (a) The pole figure of the "randomly" textured CPFE model. The distribution of misorientations between the basal plane normals of any two neighboring grains in (b) "random" and (c) "original" model. Grain-average residual stresses from "random" and "original" model. Grain-average residual stresses from "random" and "original" model: (d) σ_{11}, (e) σ_{22}, and (f) σ_{33}. Grain-average residual stresses as a function of grain dimeter from "random" model: (g) σ_{33} and (h) σ_H. The absolute of the calculated data is used for data fitting.

2.6 Conclusion

Three-dimensional synchrotron X-ray diffraction was used to measure the state of the residual stresses in the grains of a textured zirconium polycrystal. Thermal residual stresses developed during heat treatment at 700 °C and mechanical residual stresses developed after deforming the sample to 1.2% tensile strain and unloading to nearly zero macroscopic stress. The measured center of mass, orientations, and volumes of grains were used to reconstruct 3D grain shapes using weighted Voronoi tessellation and import to a CPFE model. The results of the CPFE simulations were compared to those from 3D-XRD measurement. It is concluded that:

i. Thermal residual stresses are significant in α-Zr even after stress relieving and recrystallization. This is due to the thermal and elastic anisotropy of the HCP crystals.

ii. It is shown that grain-average residual stresses at the preload and unload vary between ±200 MPa for normal stresses, with an overall standard deviation of 69 MPa and 80 MPa, respectively. Similarly, it is shown that the hydrostatic stresses at the preload and unload vary between ± 200 MPa with a standard deviation of 43 MPa and 53 MPa, respectively. This is important as hydrogen embrittlement of zirconium alloys is affected by the state of hydrostatic stresses.

iii. A model was built using the same grains of the original “textured” model, yet with “random” macro-texture. It is shown that the grain-average stresses in the “textured” model have a smaller distribution than those of the “random” model.

iv. In smaller grains, the value of the grain-average residual stresses are mainly controlled by the localized forces from grain-grain interactions.

v. The grain-average residual stresses of bigger grains are lower than smaller grains as the area of the bigger grains are high enough to counteract the effects of the localized forces developing due to grain-neighbor interactions.

vi. As a result of grain neighborhood, stress range within a grain is generally increase with grain size.

vii. After unloading the specimen from 1.2% applied strain, the variations of the grain-average stress increase due to the plasticity that occur at the grain scale.

2.7 References

[1] V. Perovic, G. C. Wheatherly, S. R. MacEwen and M. Leger, "The influence of prior deformation on hydride precipitation on Zircaloy," *Acta Metallurgica et Materialia,* pp. 363-372, 1992.

[2] C. D. Judge, W. Li, C. Mayhew, A. Buyers and G. A. Bickel, "Adopting transmission kikuchi diffraction to characterize Zr-2.5Nb CANDU pressure tubes," *CNL Nuclear Review,* vol. 7, 2018.

[3] F. Xu, R. A. Holt, M. R. Daymond, R. B. Rogge and E. C. Oliver, "Development of internal strains in textured Zircaloy-2 during uni-axial deformation," *Materials Science and Engineering A,* pp. 172-185, 2008.

[4] A. Irastorza-Landa, N. Grilli and H. Van Swygenhoven, "Laue micro-diffraction and crystal plasticity finite element simulations to reveal a vein structure in fatigued Cu," *Journal of the Mechanics and Physics of Solids,* pp. 157-171, 2017.

[5] E. M. Lauridesen, D. J. Juul, H. Poulsen and U. Lienert, "Kinetics of individual grains during recrystallization," *Scripta Materialia,* pp. 561-566, 2000.

[6] B. Jakobsen, U. Lienert, A. Almer, H. F. Poulsen and W. Pantleon, "Direct observation of strain in bulk subgrains and dislocation walls by high angular resolution three-dimensional X-ray diffraction," *Materials Science and Engineering A,* pp. 641-643, 2006.

[7] G. Johnson, A. King, M. G. Honnicke, J. Marrow and W. Ludwig, "X-ray diffraction contrast tomography: a novel technique for three-dimensional grain mapping of polycrystals. II. The combined case," *Journal of Applied Crystallography,* pp. 310-318, 2008.

[8] R. C. Hurley, J. Lind, D. C. Pagan, M. C. Akin and E. B. Herbold, "In situ grain fracture mechanics during uniaxial compaction of granular solids," *Journal of the Mechanics and Physics of Solids,* vol. 112, pp. 273-290, 2018.

[9] H. Abdolvand, M. Majkut, J. Oddershede, J. P. Wright and M. R. Daymond, "Study of 3-D stress development in parent and twin pairs of a hexagonal close-packed polycrystal: Part I – in-situ three-dimensional synchrotron X-ray diffraction measurement," *Acta Materialia,* pp. 246-255, 2015a.

[10] H. Abdolvand, M. Majkut, J. Oddershede, J. P. Wright and M. R. Daymond, "Study of 3-D stress development in parent and twin pairs of a hexagonal close-packed polycrystal: Part II – crystal plasticity finite element modeling," *Acta Materialia,* vol. 245, p. 235, 2015b.

[11] C. Aydiner, J. V. Bernier, B. Clausen, U. Lienert, C. Tome and D. Brown, "Evolution of stress in individual grains and twins in a magnesium alloy aggregate," *Physical Review B,* vol. 80, no. 2, 2009.

[12] H. Abdolvand, M. Majkut, J. Oddershede, S. Schmidt, U. Leinert, B. J. Diak, P. J. Whithers and M. Daymond, "On the Deformation Twinning of Mg AZ31B: A Three-Dimensional Synchrotron X-ray Diffraction Experiment and Crystal Plasticity Finite Element Model," *International Journal of Plasticity,* pp. 77-97, 2015.

[13] J. Oddershede, J. P. Wright, A. Beaudoin and G. Winther, "Deformation-induced orientation spread in individual bulk grains of an interstitial-free steel," *Acta Materialia,* pp. 301-313, 2015.

[14] G. Winther, J. P. Wright, S. Schmidt and J. Oddershede, "Grain interaction mechanisms leading to intragranular orientation spread in tensile deformed bulk grains of interstitial-free steel," *International Journal of Plasticity,* pp. 108-125, 2017.

[15] Z. Zhang, D. Lunt, H. Abdolvand, A. J. Wilkinson and F. P. Dunne, "Quantitative investigation of micro slip and localization in polycrystalline materials under uniaxial tension," *International Journal of Plasticity,* vol. 108, pp. 88-106, 2018.

[16] J. Jiang, J. Yang, T. Zhang, F. P. Dunne and T. B. Britton, "On the mechanistic basis of fatigue crack nucleation in Ni superalloy containing inclusions using high resolution electron backscatter diffraction," *Acta Materialia,* vol. 97, pp. 367-379, 2015.

[17] V. Tong, J. Jiang, A. J. Wilkinson and T. B. Britton, "The effect of pattern overlap on the accuracy of high resolution electron backscatter diffraction measurements," *Ultramicroscopy,* vol. 155, pp. 62-73, 2015.

[18] M. Ardeljan, I. J. Beyerlein and M. Knezevic, "A dislocation density based crystal plasticity finite element model: Application to a two-phase polycrystalline HCP/BCC composites," *Journal of the Mechanics and Physics of Solids,* pp. 16-31, 2014.

[19] T. O. Enshiro and F. P. Dunne, "Strain localization and failure in irradiated zircaloy with crystal plasticity," *International Journal of Plasticity,* vol. 71, pp. 170-194, 2015.

[20] J. Cheng and S. Ghosh, "Crystal plasticity finite element modeling of discrete twin evolution in polycrystalline magnesium," *Journal of the Mechanics and Physics of Solids,* pp. 512-538, 2017.

[21] R. A. Lebensohn and C. N. Tome, "A self-consistent anisotropic approach for the simulation of plastic deformation and texture development of polycrystals: Application to zirconium alloys," *Acta Metallurgica et Materialia,* vol. 41, no. 9, pp. 2611-2624, 1993.

[22] H. Wang, P. D. Wu, C. N. Tome and Y. Huang, "A finite strain elastic–viscoplastic self-consistent model for polycrystalline materials," *Journal of the Mechanics and Physics of Solids,* vol. 58, pp. 594-612, 2010.

[23] X. Xiazi, D. Song, J. Xu, H. Chu and H. Duan, "A self-consistent plasticity theory for modeling the thermo-mechanical properties of irradiated FCC metallic polycrystals," *Journal of the Mechanics and Physics of Solids,* vol. 78, pp. 1-16, 2015.

[24] M. A. Kumar, I. J. Beyerlein and C. N. Tome, "Effect of local stress fields on twin characteristics in HCP metals," *Acta Materialia,* vol. 116, pp. 143-154, 2016.

[25] R. A. Lebensohn and A. Needleman, "Numerical implementation of non-local polycrystal plasticity using fast Fourier transforms," *Journal of the Mechanics and Physics of Solids,* vol. 97, pp. 333-351, 2016.

[26] M. A. Kumar, L. Capolungo, R. McCabe and C. N. Tome, "Characterizing the role of adjoining twins at grain boundaries in hexagonal close packed materials," *Scientific Reports,* vol. 9, 2019.

[27] R. J. Asaro, "Crystal Plasticity," *Journal of Applied Mechanics,* vol. 50, pp. 921-934, 1983.

[28] A. Shahba and S. Ghosh, "Crystal plasticity FE modeling of Ti alloys for a range of strain-rates. Part I: A unified constitutive model and flow rule," *International Journal of Plasticity,* pp. 48-68, 2016.

[29] Y. Guan, B. Chen, J. Zou, T. B. Britton, J. Jiang and F. P. Dunne, "Crystal plasticity modelling and HR-DIC measurement of slip activation and strain localization in single and oligo-crystal Ni alloys under fatigue," *International Journal of Plasticity,* pp. 70-88, 2017.

[30] H. Abdolvand and M. R. Daymond, "Multi-scale modeling and experimental study of twin inception and propagation in hexagonal close-packed materials using a crystal plasticity finite element approach—Part I: Average behavior," *Journal of the Mechanics and Physics of Solids,* pp. 783-802, 2013a.

[31] H. Abdolvand and M. R. Daymond, "Multi-scale modeling and experimental study of twin inception and propagation in hexagonal close-packed materials using a crystal plasticity finite element approach; part II: Local behavior," *Journal of the Mechanics and Physics of Solids,* vol. 61, no. 3, pp. 803-818, 2013b.

[32] J. Cheng and S. Ghosh, "A crystal plasticity FE model for deformation with twin nucleation in magnesium alloys," *International Journal of Plasticity,* pp. 148-170, 2015.

[33] T. R. Bieler, P. Eisenlohr, F. Roters, D. Kumar, D. E. Mason, M. A. Crimp and D. Raabe, "The role of heterogeneous deformation on damage nucleation at grain boundaries in single phase metals," *International Journal of Plasticity,* pp. 1655-1683, 2009.

[34] Y. Su, C. Zambaldi, D. Mercier, P. Eisenlohr, T. R. Bieler and M. A. Crimp, "Quantifying deformation processes near grain boundaries in α titanium using nanoindentation and crystal plasticity modeling," *International Journal of Plasticity,* pp. 170-186, 2016.

[35] S. Keshavarz, S. Ghosh, A. C. Reid and S. A. Langer, "A non-Schmid crystal plasticity finite element approach to multi-scale modeling of nickel-based superalloys," *Acta Materialia,* pp. 106-115, 2016.

[36] S. Forest, R. Sievert and E. C. Aifantis, "Strain gradient crystal plasticity : thermomechanical formulations and applications," *Journal of the Mechanical Behaviour of Materials,* vol. 13, pp. 219-232, 2002.

[37] A. Ma, F. Roters and D. Raabe, "A dislocation density based constitutive model for crystal plasticity FEM including geometrically necessary dislocations," *Acta Materialia,* pp. 2169-2179, 2006.

[38] T. O. Erinosho and F. P. Dunne, "Lattice strain distributions due to elastic distortions and GND development in polycrystals," *Journal of the Mechanics and Physics of Solids,* pp. 62-86, 2014.

[39] H. Abdolvand, J. Wright and A. J. Wilkinson, "Strong grain neighbour effects in polycrystals," *Nature Communications,* 2018.

[40] A. Lyckegaard, E. M. Lauridsen, W. Ludwig, R. W. Fonda and H. F. Poulsen, "On the Use of Laguerre Tessellations for Representations of 3D Grain Structures," *Advanced Engineering Materials,* pp. 165-170, 2011.

[41] H. Abdolvand, M. R. Daymond and C. Mareau, "Incorporation of twinning into a crystal plasticity finite element model: Evolution of lattice strains and texture in Zircaloy-2," *International Journal of Plasticity,* pp. 1721-1738, 2011.

[42] J. Gong, B. T. Britton, M. A. Cuddihy, F. P. Dunne and A. J. Wilkinson, "〈a〉 Prismatic, 〈a〉 basal, and 〈c+a〉 slip strengths of commercially pure Zr by micro-cantilever tests," *Acta Materialia,* pp. 249-257, 2015.

[43] E. S. Fisher and C. J. Renken, "Single-Crystal Elastic Moduli and the hcp → bcc Transformation in Ti, Zr, and Hf," *Physics Review,* vol. 135, 1964.

[44] D. Gonzalez, Simonovski, P. J. Withers and J. Quinta da Fonseca, "Modelling the effect of elastic and plastic anisotropies on stresses at grain boundaries," *International Journal of Plasticity,* pp. 49-63, 2014.

[45] M. P. Puls, The Effect of Hydrogen and Hydrides on the Integrity of Zirconium Alloy Components, London: Springer, 2012.

[46] H. Abdolvand, "Progressive modelling and experimentation of hydrogen diffusion and precipitation in anisotropic polycrystals," *International Journal of Plasticity,* pp. 39-61, 2019.

3 Microstructural variations in a neutron irradiated Zr-2.5Nb CANDU pressure tube

Abstract

In a CANada Deterium Uranium (CANDU) nuclear reactor, pressure tubes are the boundaries between the hot heavy water and the cold moderator. These tubes are made of a Zr-2.5Nb alloy and are susceptible to hydrogen diffusion and formation of a brittle phase called zirconium hydrides. The microstructure of the pressure tube can affect the process of hydrogen diffusion and the formation of hydrides. In this paper, Electron BackScatter Diffraction (EBSD) technique is used to characterize the variations of microstructures and textures in a neutron irradiated CANDU pressure tube. EBSD measurements are performed on the samples taken from different axial positions of a tube that was in a CANDU reactor for 22 years. In addition, measurements are conducted on the unirradiated samples taken from the offcut of the same tube. It is shown that for the positions that are measured, the radial transverse surface areas of the grains increase with distancing from the front-end of the tube. It is observed that the population of basal plane normals varies with distancing from the front-end of the tube. Also, it is shown that the localized orientation variation within some grains are as high as 14° in both irradiated and unirradiated samples.

3.1 Introduction

Zirconium (Zr) and its alloys are commonly used in the core of CANDU nuclear reactors due to their low neutron absorption cross section and good mechanical properties. In the core of a CANDU reactor, fuel rods are placed in 300-400 pressure tubes that are made of a Zr-2.5Nb alloy. This is a dual phase alloy containing an α-Zr phase with Hexagonal Close-Packed (HCP) crystals and a β-Zr phase with Body Centered Cubic (BCC) crystals. Both phases have anisotropic elastic and plastic properties. One of the main problems affecting the effective lifespan of the pressure tubes is the diffusion of hydrogen atom from hot water into the Zr lattice causing the formation of a brittle phase called zirconium

hydride (ZrH_x) which can lead to delayed hydride cracking (DHC) [1]. It is shown that the formation of hydrides in Zr is affected by the stresses developed at the grain boundaries and the stress variation within grains [2], [3]. It is also postulated that the thermal residual stresses that develop from manufacturing can affect the formation of hydrides [4], and it has been shown, in pure α-Zr, that these residual stresses are greatly affected by the grain size and texture of the specimen [5]. As such, studying the microstructure and texture of the pressure tube is of great significance and is the focus of this paper.

A significant number of studies conducted on Zr-2.5Nb have focused on understanding the effects of microstructure and texture on the performance of pressure tubes in the reactor. For instance, the effects of different manufacturing processes on the developed textures and mechanical properties have been examined [6], [7]. It was reported that higher extrusion ratios result in a more desirable and uniform texture, and the extrusion temperature greatly affects the microstructure of the α-phase grains. In another study conducted by Bickel and Griffiths [8], it was shown that due to impurities of the initial ingot, the performance of the pressure tubes varies even when the same manufacturing route was used to fabricate them. Such impurities can affect the final microstructure and the mechanical properties of the tubes. Other studies have shown that the secondary β-phase greatly affect the mechanical properties and the active deformation modes of the pressure tube material [9]–[11]. For example, the size of the β-phase grains affects the yield strength of tube. Also, the presence of the harder β-phase results in an increased grain average misorientation and lattice strains under loading, while the presence of softer, finer β-phase grains is more likely to cause deformation twinning. A more Nb enriched β-phase was shown to improve the oxidation resistance of the tube [12], [13].

Several experimental techniques can be used to characterize the texture and microstructure of the pressure tube material. Here macro-texture is referred to the average texture of samples when a significant number of grains are integrated, while micro-texture refers to very localized orientation variation that occurs within individual grains. Neutron diffraction has been used to characterize the macro-texture of ion irradiated, neutron irradiated and unirradiated pressure tube samples [14], [15]. X- ray diffraction (XRD) technique was also used to identify and measure the average texture of oxides in Zr-2.5Nb

[16]. Transmission electron microscope selected area diffraction was proven an effective method to study microstructure of the pressure tube material and identify β-phase grains [15], [17]. In addition, scanning transmission electron microscopy was used to identify zirconium oxide grains and metallic Zr suboxide grains at the metal-oxide interface of a Zr-1.0Nb sample [18].

Electron backscatter diffraction (EBSD) technique is another method that can be used to measure micro-texture, macro-texture, microstructure, and localized stress and rotation fields. For example, Holt and Zhao [19] used EBSD to measure the micro-texture from two lab-extruded unirradiated pressure tube samples. They were able to correlate the general micro-texture of the tube to the dislocations type and density. However, resolving grains finer than 1 μm was proven challenging in this study due to method limitations. In addition, Hovington et al. [20] used SEM digital image analysis and EBSD to study the microstructure and micro-texture of samples from the front end of a pressure tube and were able to characterize the finer grains. They showed that EBSD can characterize the α-α grain boundaries more reliably compared to digital image analysis; however, the SEM digital image analysis was more successful in capturing α-β grain boundaries. Also, an extrapolation technique was used to fill unindexed regions of the collected EBSD maps and determine β-Zr phase. EBSD was also used to measure the crystallographic orientation of δ-Hydrides in several Zr alloys, including Zr-2.5Nb [21]. More recently, EBSD was used to characterize the microstructure and texture of Zr-2.5Nb plates before and after low-temperature neutron irradiation [22]. The goal of the study was to investigate the effects of low temperature irradiation on the mechanical properties of Zr-2.5Nb plates.

In this paper, the microstructure as well as the micro- and macro-texture of Zr-2.5Nb neutron irradiated and unirradiated pressure tube samples are studied using EBSD. The neutron irradiated samples were taken from a pressure tubes that was in-service in a CANDU nuclear reactor for 25 years. These samples were taken from two different axial positions of the front-end section of the tube. The results from the irradiated samples are compared to those from unirradiated samples taken from the offcut of the same pressure tube. Methods used for measuring grains maps are described, and the measured microstructures at different axial positions are subsequently compared and discussed.

3.2 Samples and experimental setup

Samples were taken from a CANDU pressure tube that was extruded at 817 °C with an extrusion ratio of 11:1. This was followed by a 25% cold work, and then the tube is stress relieved at 450 °C for 24 hours. The pressure tube was inside of a CANDU reactor for 22 years. Four TEM foils were prepared for texture measurement. Three of the foils were taken from two different axial positions from the pressure tube. Two of the foils, S1 and S2, were taken from 0.09 m away from the front-end of the tube. The third foil, sample S3, was taken from 1.79 m away from the front-end of the tube. The last foil, sample AR, was taken from the offcut of the front end of the same pressure tube, but it was not irradiated. All samples are from the same radial position. In table 3.1, a summary on the samples is given. All foils were taken from the radial-transverse surface, known as transverse normal, of the pressure tube. 2 mm thick foils were electropolished at -30 °C using 17 V current in a solution of 95% methanol and 5% perchloric acid until the surface quality was suitable for EBSD measurements.

The EBSD measurements were conducted at the Reactor Materials Testing Laboratory at Queen's University using an FEI-FEG SEM. A beam energy of 30 kV was used with a beam current of 20 nA, and a step size of 25 nm. The sample to detector distance was set at 17 mm. With the set-up used it was possible to index α-Zr grains, but not the fine grains of the β-phase.

Table 3.1 Axial positions of the samples in the pressure tube, number of EBSD maps, and average map size.

Sample	Axial Position (m)	Number of Measured EBSD Maps	Average Map Size (µm x µm)
S1	**0.09**	**3**	**5.0 x 4.4**
S2	**0.09**	**3**	**4.7 x 4.1**
S3	**1.79**	**4**	**5.1 x 5.1**
AR	**Front-end off-cut**	**3**	**5.2 x 4.6**

3.3 Results

Three EBSD maps per sample were measured for samples S1 and S2, but from different regions. For sample S1, the average size of the EBSD maps was 5.0 µm x 4.4 µm while for the sample S2 it was 4.7 µm x 4.1 µm. From sample S3, four EBSD maps with the average map size of 5.1 µm x 5.1 µm were measured. For the AR sample, three maps with the average size of 5.2 µm x 4.6 µm were measured.

3.3.1 Reconstruction of grain maps

The measured Euler angles were used for reconstructing grain maps by assigning a specific threshold for determining grain boundaries (GBs). In this process, the orientation of each measured point was compared to the orientation of the neighboring points, and if the total misorientation was lower than the specified threshold, the point was considered to be inside the grain. The misorientation angle between any points A and B was determined as:

$$\theta = min\left[\cos^{-1}\frac{trace(R_A R_B^T) - 1}{2}\right] \qquad (1)$$

where R_A and R_B are the rotation matrixes of the two points and are calculated using their Euler angles [23]. Since HCP crystals are transversely isotropic, θ greater than 90° can be replaced by $180 - \theta$.

Table 3.2 Number of measured grains after filtering

Filter (minimum number of points/grain)	Grains S1	Grains S2	Grains S3	Grains AR
10	359	274	288	275
20	302	243	253	226
30	272	215	212	206
40	251	200	198	190
50	236	192	183	172

Assigning the suitable misorientation threshold for determining grain boundaries was done using an iterative process. That is, the estimated grain boundaries from the reconstructed grain map were compared to those observed in the corresponding EBSD quality map until the two maps were matched. Figure 3.1 shows an example of an EBSD map acquired from sample S1 where in Figure 3.1(a), the misorientation threshold is set at 2.5°. In comparison to the corresponding quality map, it is observed that some GBs are missing. In Figure 3.1(b), the GB threshold angle is reduced to 1° where the previously missing GBs are now present. It is however observed that using a 1° threshold does not capture the correct grain boundaries for some of the measured maps, e.g., see Figure 3.1(d). The misorientation angle is as small as 0.5° for these GBs (Figure 3.1(e)). However, using 0.5° to define GBs leads to some artificial GBs that are not found in the corresponding quality map (Figure 3.1(f)). Hence, a misorientation threshold of 1° was used for determining GBs, and the regions with 0.5° GBs angle are considered as "sub-structures" within the larger grains. The measured maps were subsequently filtered to remove noisy regions, incorrectly indexed points, and grains with significant unindexed points. This was done by removing "grains" with a low number of measurement points. Figure 3.1(g) shows an example of a map from the AR sample before applying any filters and after, where grains smaller than 10 and 50 measurement points were removed. Table 3.2 provides a sensitivity study of how the filtering procedure affects the number of measured grains. The biggest drop in the

number of grains occurs when the minimum number of points per grains changes from 10 to 20 where a maximum of 18% change is observed. The number of grains starts converging after applying a filter of 40 points per grain where a maximum drop of 9.4% in the numbers of grains is observed for the AR sample. As such, it is decided to filter grains with less than 50 measurement points from the analysis provided in the following sections. The final numbers of measured grains are 236, 192, 183, and 172 for samples S1, S2, S3, and AR, respectively, making a total of 783 grains to be analyzed.

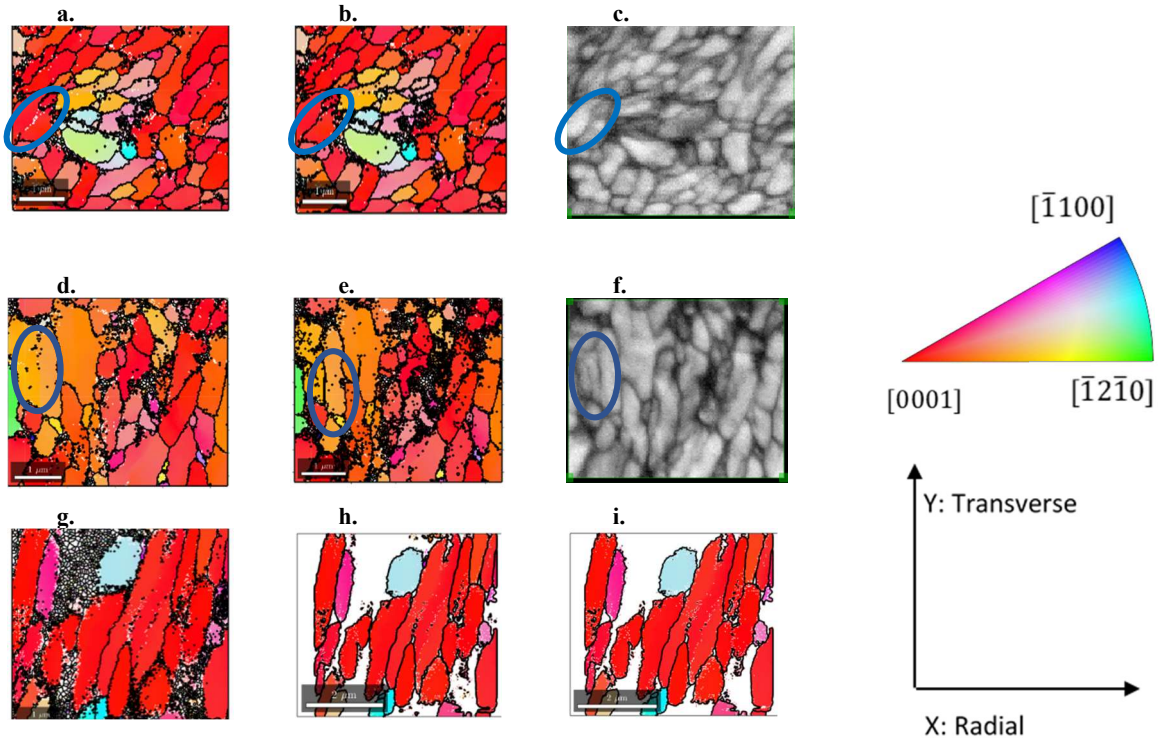

Figure 3.1 Grain maps from sample A1 reconstructed using (a) 2.5° and (b) 1° misorientation thresholds. (c) The corresponding quality map. Grain maps from sample A1 reconstructed using (d) 1° and (e) 0.5° misorientation thresholds. (f) The corresponding quality map. A reconstructed map from the AR sample (g) before filtering, (h) after filtering noise and using 10 points as the minimum limit for determining grains, and (i) after filtering the noise and using 50 points as the minimum limit for determining grains. The inverse pole figure Y legend and the coordinate system that are used are shown on the right.

3.3.2 Microstructure

In this section, the grain area of all samples is analyzed and compared. Grain area is defined as the number of points measured for a grain multiplied by the area of the point (25 nm x 25 nm). Table 3.3 provides the average grain area of each sample with the measured standard deviations.

Table 3.3 Summary of average grain area measured for each sample

	S1	**S2**	**S3**	**AR**
Average grain Area (μm^2)	0.24 ± 0.27	0.27 ± 0.36	0.34 ± 0.32	0.47 ± 0.68

Grains from samples S1 and S2 have the smallest average area followed by grains from sample S3. In all samples, the calculated standard deviation is greater than the mean grain area which indicates that the grain area varies significantly within each sample. The largest variation is found in the AR sample. In Figure 3.2(a), the measured grain areas of all samples are compared. It is observed that 70% of grains from sample S1 and S2 are with a grain area less than 0.2 μm^2 whereas 50% of grains from samples S3 and AR fall within this grain-area range. These results show that the grain area of the Radial-Transverse surface increases with distancing from the front end of the pressure tube towards sample S3; however, this does not imply that the same trend holds for the back end of the tube. More measurements from the middle section and back end of the tube are required. Further, the previous measurements of thermal residual stresses in pure zirconium indicated that there is a correlation between grain size and thermal residual stresses [5], where bigger grains exhibit lower residual stresses. Hence, on average, thermal residual stresses in S3 is expected to be lower than S1 and S2, i.e., thermal residual stresses at the front-end of the tube might be higher. Figure 3.2(b) shows the distribution of the measured grain aspect ratios in each sample. The aspect ratios are calculated by firstly fitting an ellipse to each grain and subsequently dividing the longer axis to the lower one. Unlike the area, the grain aspect ratios are rather random. It is also apparent that all samples have a higher percentage of elongated grains with aspect ratio greater than two. Also, our EBSD analysis indicate that most grains have their major axis along the transverse direction. Overall, it is shown that the microstructure of the pressure tube changes with respect to the axial position.

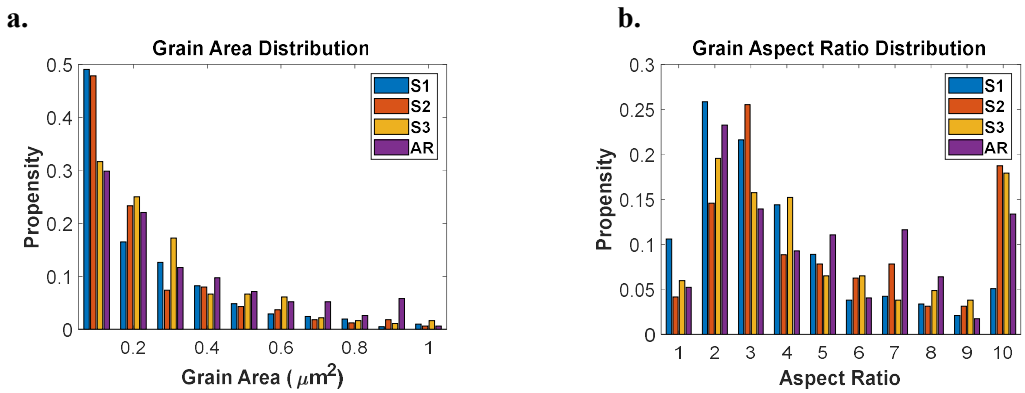

Figure 3.2 (a) The distribution of the measured grain areas for all samples. (b) The distribution of the measured grain aspect ratios for all samples.

3.4 Discussion

Characterizing the texture and the variation of misorientations within individual grains of the pressure tube are important for understanding and predicting hydrogen embrittlement. In this section, the misorientation within grains and the average texture of the investigated samples are analyzed and compared.

3.4.1 Texture Analysis

The distribution of the misorientations between the basal plane normals and the transverse direction (TD), radial direction (RD), and axial direction (AD), are shown in Figures 3.3(a), 3(b), and 3(c), respectively. In generating this figure, all measurement points are used. It is shown in Figure 3.3(a) that, 50% of the measurement points from samples S3 and AR have a misorientation of 15° or less, while 40% of the measured pixels from samples S1 and S2 are within that range. Further, 50% of the measurement points from all samples have a misorientation of 75° or higher with respect to the RD or AD..In addition, the lowest transverse texture is found in samples S1 and S2. The standard deviations of the Kearns factors are provided where highest texture variation is observed in sample S2 in the TD. The variation is 8.9% which is twice the measured variation for sample S1, even though both samples are from the same axial position. This indicates that the micro-texture of the pressure tube varies significantly.

Table 3.4 Summary of Kearns factor

Axis	S1	S2	S3	AR
F_{RD} (%)	17.5 ± 4.0	17.3 ± 7.5	14.7 ± 3.8	13.8 ± 2.9
F_{TD} (%)	80.5 ± 4.3	79.0 ± 8.9	82.4 ± 3.8	84.7 ± 2.8
F_{AD} (%)	2.0 ± 0.3	3.7 ± 1.4	2.9 ± 0.5	1.5 ± 0.5

The EBSD measured (0002) and $(11\bar{2}0)$ pole figures of each sample are shown in Figures 3.3(d)-3.3(g). Table 3.4 provides the Kearns factor of the (0002) poles for all samples. Kearns factor is the effective fraction of measurement points with the HCP crystal c-axis oriented towards one of the three principal directions. The measured maps for each sample are combined into one, and the Kearns factor is calculated for each sample. The standard deviations are calculated using the Kearns factor for each map. All samples are highly transversely textured. The population of basal plane is minimum along the AD. The AR sample has the highest transverse texture followed by sample S3. In addition, the lowest transverse texture is found in samples S1 and S2. This is significant because, based on the findings of Holt and Zhao [19], pressure tube specimens with higher transverse textures tend to have lower dislocation density. The standard deviations of the Kearns factors are provided where the highest texture variation is observed in sample S2 in the TD. This variation is 8.9 which is twice what measured for sample S1, even though both samples are from the same axial position. This indicates that the micro-texture of the pressure tube varies significantly. Further, some variations are observed with distancing from the inlet. Hovington et al. reported Kearns factors of F_{RD} = 30% and F_{TD} = 70% from a front end offcut grains population of over 3000 grains [20]. The difference in the reported results could be accounted to the difference in the number of grains population examined in the offcut.

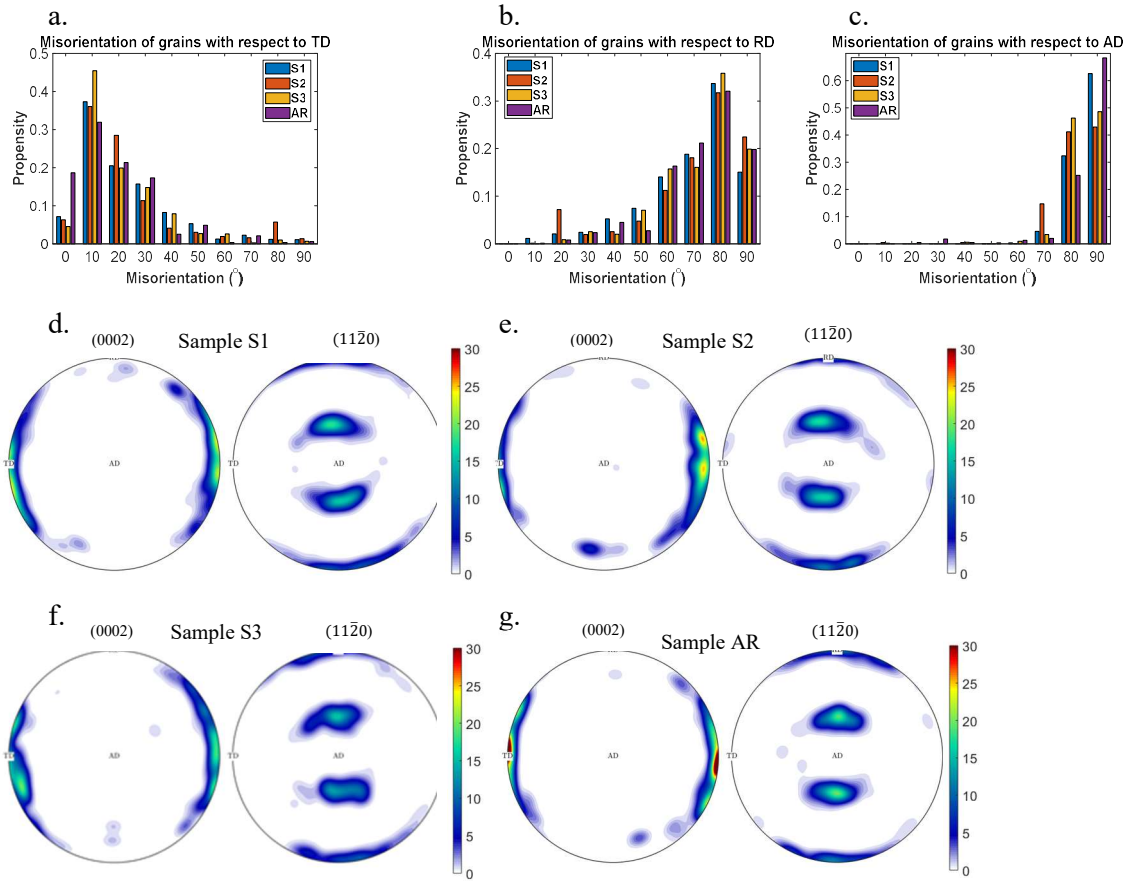

Figure 3.3 The misorientation between the basal plane normals and (a) TD, (b) RD, and (c) AD. The measured pole figures of (d) S1, (e) S2, (f) S3, and (g) AR samples. Pole figures are provided in the units of multiple random distribution (mrd).

3.4.2 Misorientation Analysis

The grain-average-misorientation is determined by first calculating the grain average orientation, and then calculating the misorientation of each measurement point within the same grain with respect to the grain average orientation. In this process the absolute values of misorientations are averaged. This parameter is an indication of the level of plasticity

that develops within grains during service and if the heat treatment performed on the pressure tube, prior to service, was enough to cause uniform recovery. The origin of such misorientations is generally the localized dislocation densities that do not annihilate during heat treatment which is a further indication of the partial re-arrangement of dislocations during aging and recovery of the tubes. The higher the grain-average-misorientation, the higher the probability of having partial recovery during manufacturing. Neutron irradiation and radiation-enhanced-creep are two other contributing factors. The grain-average-misorientation is found to be 0.99°, 0.93°, 0.71°, and 0.70° for samples S1, S2, S3 and AR, respectively. Figure 3.4(a) provides a distribution of grain-average-misorientation for the grains indexed in the four studied samples. While the grain-average-misorientation of all samples is less than 1°, in some grains, the average misorientation exceeds 4°. Further, the variation of grain-average-misorientations in samples S3 and AR is less than those of samples S1 and S2. This indicates higher level of plasticity and potentially residual stresses at the front end of the pressure tubes.

The variation of "local" misorientation within grains is further studied by comparing the measured orientations along different paths selected within the grains. The orientation of the first point along the path was used as the reference point for calculating the misorientations of the rest of the points along the same path (see Figures 3.4(b)-3.4(d)). In Figure 3.4(b), the variation of local misorientation within a grain of sample S1 is plotted. The selected path represents the highest variation in misorientation. It is shown that misorientation can be as high as 14°. Such a high misorientation is an indication of large lattice rotations and the existence of high geometrically necessary dislocation densities, especially at the vicinity of the grain boundaries where misorientations are significantly high.

In Figure 3.4(c), the variation of local misorientation within a grain of sample AR is plotted. The maximum local misorientation in this grain is ~ 7°. Since this sample is taken from the same tube but was not irradiated, it can be concluded that the high misorientations observed in the grains of S1 is not only due to irradiation but also due to the prior work hardening that was during manufacturing. Further, it shows that the heat treatment done on the tube during fabrication did not fully anneal the tube.

In Figure 3.4(d), the variation of local misorientation of another grain of sample S1 is plotted. The local misorientation of the longer axis is as high as 4° while along the minor axis it is only 2°. Other grains show a similar trend where the local misorientation is higher along the grains major axis compared to the minor one. In Figures 3.4(e) and 3.4(f) the grain-average-misorientation is plotted against grain area and grain aspect ratio, respectively. It can be seen that in all samples, the grains with bigger area and bigger aspect ratio have a higher average misorientation. These grains with higher misorientations are expected to develop higher thermal residual stresses based on previous work done on pure α-Zr [5].

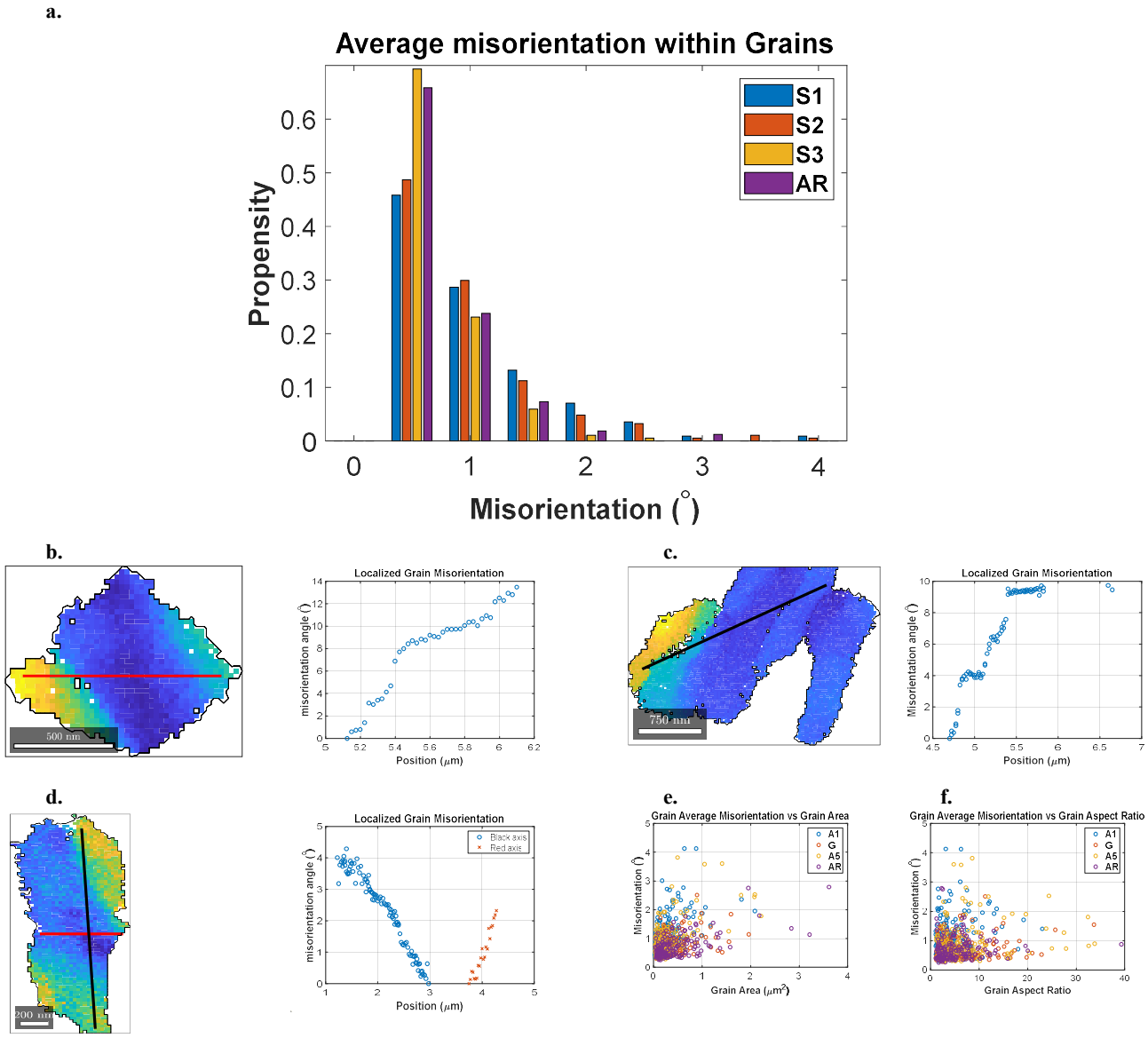

Figure 3.4 (a) Distribution of the grain average misorientation. (b) The local misorientation plot of a grain in sample S1. (c) The local misorientation plot of a grain from the AR sample. (d) The local misorientation plot of the major and minor axes of a grain in sample S1. (e) The grain average misorientation plotted against the grain area. (f) The grain average misorientation plotted against the grain aspect ratio.

3.5 Conclusion

Three samples from two axial positions of a neutron irradiated Zr-2.5 CANDU pressure tube were prepared for microstructural analysis with EBSD. Two samples, S1 and S2 were taken from the front-end of the tube, while the third sample (S3) was taken from 1.7 m from the front-end. In addition, one more sample (AR) was prepared from the front-end offcut of the same tube but was not irradiated. After grain map reconstruction, a total of 783 grains were analyzed. It was shown that:

- The microstructure of the pressure tube varies along the axial direction.
- The areas of the grains on the radial-transverse plane, i.e., transverse-normal, increases with distance from the front end of the pressure tube towards the location of S3.
- There are more elongated grains than equiaxed grains in the pressure tube, and with grains major axis oriented towards the transverse direction.
- grains in all samples have their c-axis parallel to the transverse direction but the population of c-axes changes among the samples even for the same axial location.
- The grain-average-misorientation for samples S1, S2, S3, and as-received were measured to be 0.99°, 0.93°, 0.71° and 0.70°, respectively; however, the average misorientation in some grains is as high as 4°.
- The higher grain-average-misorientation for the S1 and S3 samples and having smaller average grain area is an indication of higher residual stresses at the front-end of the pressure tube.
- While the grain average misorientation is of the order of 1°, it is shown that the local misorientation within a grain can be as high as 10°.

- High misorientation were found in the unirradiated samples as well as in the irradiated ones indicating that the heat treatment performed on the pressure tubes prior service may have not annihilate a significant fraction of dislocations.

3.6 References

[1] M. P. Puls, “Review of the thermodynamic basis for models of delayed hydride cracking rate in zirconium alloys,” *Journal of Nuclear Materials*. 2009, doi: 10.1016/j.jnucmat.2009.06.022.

[2] V. Perovic, G. C. Weatherly, S. R. MacEwen, and M. Leger, “The influence of prior deformation on hydride precipitation in zircaloy,” *Acta Metall. Mater.*, 1992, doi: 10.1016/0956-7151(92)90310-B.

[3] H. Abdolvand, “Progressive modelling and experimentation of hydrogen diffusion and precipitation in anisotropic polycrystals,” *Int. J. Plast.*, 2019, doi: 10.1016/j.ijplas.2018.12.005.

[4] C. D. Judge, W. Li, C. Mayhew, A. Buyers, and G. A. Bickel, “ADOPTING TRANSMISSION KIKUCHI DIFFRACTION TO CHARACTERIZE GRAIN STRUCTURE AND TEXTURE OF ZR-2.5NB CANDU PRESSURE TUBES,” *CNL Nucl. Rev.*, 2017, doi: 10.12943/cnr.2017.00010.

[5] A. Alawadi and H. Abdolvand, “Measurement and modeling of micro residual stresses in zirconium crystals in three dimension,” *J. Mech. Phys. Solids*, vol. 135, 2020, doi: 10.1016/j.jmps.2019.103799.

[6] N. Saibaba *et al.*, “Study of microstructure, texture and mechanical properties of Zr-2.5Nb alloy pressure tubes fabricated with different processing routes,” *J. Nucl. Mater.*, 2013, doi: 10.1016/j.jnucmat.2013.03.069.

[7] C. Nam, J. Lin, H. Li, J. A. Szpunar, and R. Holt, “Effects of tube fabrication variables on the oxidation of experimental Zr-2.5Nb tubes,” *J. Nucl. Mater.*, 2006, doi: 10.1016/j.jnucmat.2006.02.091.

[8] G. A. Bickel and M. Griffiths, “Manufacturing variability and deformation for Zr-2.5Nb pressure tubes,” *J. Nucl. Mater.*, 2008, doi: 10.1016/j.jnucmat.2008.08.048.

[9] Y. P. Devi, H. Donthula, N. Keskar, A. Sarkar, K. Vaibhaw, and K. V. M. Krishna, “Microstructural evolution in (α + βZr) region of Zr-2.5 wt% Nb annealed at different temperatures: Effect on mechanical properties,” *J. Nucl. Mater.*, 2020, doi: 10.1016/j.jnucmat.2019.151978.

[10] M. Gallaugher *et al.*, “Variations in nanomechanical properties of back-end Zr-2.5Nb pressure tube material,” *J. Nucl. Mater.*, 2013, doi: 10.1016/j.jnucmat.2013.08.047.

[11] S. K. Sahoo *et al.*, “Deformed microstructures of two-phase Zr-2.5Nb alloy: Effects of the second phase hardnesss,” *J. Nucl. Mater.*, 2010, doi: 10.1016/j.jnucmat.2010.07.028.

[12] G. Choudhuri *et al.*, “Effect of heavy ion irradiation and α+β phase heat treatment on oxide of Zr-2.5Nb pressure tube material,” *J. Nucl. Mater.*, 2017, doi:

10.1016/j.jnucmat.2017.03.032.

[13] S. K. Nouduru, M. K. Kumar, V. Kain, A. S. Khanna, N. Saibaba, and G. K. Dey, "High temperature and high pressure oxidation behavior of Zr-2.5Nb pressure tube material - Effect of β phase composition and surface machining," *J. Nucl. Mater.*, 2016, doi: 10.1016/j.jnucmat.2015.12.030.

[14] Q. Wang, F. Long, Z. Wang, N. Guo, and M. R. Daymond, "Orientation dependent evolution of plasticity of irradiated Zr-2.5Nb pressure tube alloy studied by nanoindentation and finite element modeling," *J. Nucl. Mater.*, 2018, doi: 10.1016/j.jnucmat.2018.10.033.

[15] Y. Li, R. Rogge, and R. A. Holt, "Development of local microstructure and crystallographic texture in extruded Zr-2.5Nb tubes," *Mater. Sci. Eng. A*, 2006, doi: 10.1016/j.msea.2006.04.048.

[16] J. Lin, H. Li, C. Nam, and J. A. Szpunar, "Analysis on volume fraction and crystal orientation relationship of monoclinic and tetragonal oxide grown on Zr-2.5Nb alloy," *J. Nucl. Mater.*, 2004, doi: 10.1016/j.jnucmat.2004.06.003.

[17] Y. P. Lin and O. T. Woo, "Oxidation of β-Zr and related phases in Zr-Nb alloys: An electron microscopy investigation," *J. Nucl. Mater.*, 2000, doi: 10.1016/S0022-3115(99)00153-1.

[18] J. Hu *et al.*, "Identifying suboxide grains at the metal-oxide interface of a corroded Zr-1.0%Nb alloy using (S)TEM, transmission-EBSD and EELS," *Micron*, 2015, doi: 10.1016/j.micron.2014.10.004.

[19] R. A. Holt and P. Zhao, "Micro-texture of extruded Zr-2.-5Nb tubes," *J. Nucl. Mater.*, 2004, doi: 10.1016/j.jnucmat.2004.07.043.

[20] P. Hovington, P. T. Pinard, M. Lagacé, L. Rodrigue, R. Gauvin, and M. L. Trudeau, "Towards a more comprehensive microstructural analysis of Zr-2.5Nb pressure tubing using image analysis and electron backscattered diffraction (EBSD)," *J. Nucl. Mater.*, 2009, doi: 10.1016/j.jnucmat.2009.05.017.

[21] N. A. P. Kiran Kumar and J. A. Szpunar, "EBSD studies on microstructure and crystallographic orientation of δ-hydrides in Zircaloy-4, Zr-1% Nb and Zr-2.5% Nb," *Mater. Sci. Eng. A*, 2011, doi: 10.1016/j.msea.2011.05.022.

[22] C. Silva, K. Leonard, M. Trammel, and C. Bryan, "Characterization of different forms of Zr-2.5Nb samples before and after neutron irradiation," *Mater. Sci. Eng. A*, 2018, doi: 10.1016/j.msea.2018.01.059.

[23] O. Engler and V. Randle, *Introduction to Texture Analysis: Macrotexture, Microtexture and Orientation Mapping*. 2010.

4 Residual stresses in a neutron irradiated Zr-2.5Nb CANDU pressure tube

Abstract

In CANada Deterium Uranium (CANDU) nuclear reactors, pressure tubes are the primary boundary between the hot pressurized water coolant and the cold moderator. These pressure tubes are made of a Zr-2.5Nb alloy and are susceptible to the diffusion of hydrogen atoms and the formation of a brittle phase called zirconium hydrides. Stress variation and highly localized stress fields can affect the diffusion of hydrogen atoms. In this paper, high angular resolution electron backscatter diffraction (HR-EBSD) is used to measure the orientation and stress variation within grains of four different samples taken from different axial position of a pressure tube. Three of the samples were taken from the front-end and middle of the tube that was neutron irradiated inside a CANDU reactor for 25 years. The fourth sample was taken from the front-end offcut of the same pressure tube but was not irradiated. The EBSD measured grain maps are subsequently imported into a crystal plasticity finite element (CPFE) model to study the state of the residual stresses considering the possible effects of irradiation growth. The CPFE results are compared with those measured with EBSD. Results show that the stress variation and localized intragranular stresses are higher at the front end of the pressure tube. It is shown that the development of such stresses is mainly affected by the micro textures of the samples and intergranular orientation variations.

4.1 Introduction

Zirconium (Zr) alloys are used in the core of CANDU nuclear reactors due to their low neutron absorption cross section and good mechanical properties. In CANDU reactors, the

pressurized heavy water coolant runs through pressure tubes that contain fuel bundles. These tubes are made of a Zr-2.5Nb alloy and are manufactured by extrusion at elevated temperatures followed by a heat treatment at a lower temperature. Zr-2.5Nb is a dual phase alloy comprising of α-Zr with hexagonal close-packed (HCP) crystals, and β-Zr with body centered cubic (BCC) crystals. Both α and β phases are elastically and plastically anisotropic. The diffusion of hydrogen atoms from the hot water into Zr lattice is one of the main challenges affecting the lifespan of the pressure tubes. By increasing the concentration of hydrogen atoms beyond the solid solubility limit, a brittle phase known as zirconium hydride (ZrH_x) forms which reduces the fracture toughness of the alloy. It is shown that the variation of stresses at the grain boundaries and within the grains affects the diffusion of hydrogen atoms [1]. Therefore, investigating the state of residual stresses that develop during manufacturing of pressure tubes helps understand their subsequent effects on formation of hydrides and in-service performance of the tubes. As such, this paper focuses on characterizing grain-scale residual stresses in a CANDU pressure tube.

Irradiation by neutrons or ions is another possible reason for embrittlement of the Zr alloys used in the core of nuclear reactors. The effects of neutron and ion irradiation on the yield strength of Zr-2.5Nb have been widely studied. For example, it is shown that the irradiated Zr-2.5Nb samples exhibit higher yield strength with reduced elastic and plastic anisotropy [2], [3]. Dong et al. [4] showed that alloying Zr-2.5Nb with Cu reduces the irradiation induced dislocation loops and slows down the irradiation hardening process. Moreover, it was shown that the presence or absence of a neutron flux does not affect the diffusion of deuterium in unirradiated Zr-2.5Nb samples [5].

To understand the mechanism of hydrogen embrittlement, it is necessary to characterize the microstructure of the material and determine any possible existing correlation. Zr-2.5Nb pressure tubes are manufactured by extrusion at 815 °C followed by aging at 425 °C for 24 hours. This results in formation of a very fine grains that are nontrivial to resolve. High angular resolution electron backscatter diffraction (HR-EBSD) is one of the few techniques that can be used to not only analyze such a fine microstructure but also quantify the state of the residual stresses at the grain scale [6]. For measuring elastic lattice strain and rotations, the Kikuchi diffraction patterns collected at different locations within a grain

are cross correlated to determine their movements with sub-pixel resolutions. Using the method developed by Wilkinson et al [7], it is possible to correlate such movements to the "relative" stresses measured with respect to a reference point selected within the same grain. The precision of this method for measuring relative elastic strains is 10^{-4} and for measuring relative elastic lattice rotations is 10^{-4} radians [8]. HR-EBSD is used successfully to measure grain-scale stresses every 18 nm [9], to measure stresses near grain boundaries [10], [11], slip bands [12], twins [13], and most recently to measure stresses in irradiated materials [14].

Numerical simulations are often combined with experimental measurements to provide complementary information. Different numerical methods are used to study the effects of irradiation on the performance of Zr alloys. For example, atomistic modeling and molecular dynamics (MD) are used to simulate the effects of irradiation growth and formation of vacancy loops in Zr. It was shown that irradiation growth is mainly affected by the formation of self-interstitial atoms. Further, the growth of vacancy loops could affect delayed hydride cracking of zirconium alloys by providing the crack initiation sites that weaken the hydride-matrix interfaces [15]–[17]. The formation of defects in irradiated Zr under macroscopic load was also studied using MD. It was shown that the macroscopic strain affects the size of the defects rather than the total number of defects [18]. While MD modeling has provided valuable insight into understanding the performance of Zr alloys, it is computationally costly to use this technique to study polycrystals or study materials in "real" engineering time scales. Crystal plasticity, in finite element or self-consistent framework, has been used to connect the scales. For example, Visco-plastic self-consistent models are used to simulate irradiation creep and growth of Zircaloy-2 samples under different scenarios such as the loss of coolant accident [19], [20]. In addition, crystal plasticity finite element (CPFE) analysis is used to model the orientation dependence of irradiation hardening in Zr polycrystals [21]. The advantage of CPFE modeling is that it can be used to study the effects of elastic and plastic anisotropy on the grain-grain interactions. CPFE analysis has also been coupled with HR-EBSD measurements to study deformation of polycrystals [22], [23].

In this paper, HR-EBSD is used to measure the variation of residual stresses and lattice rotations of four different Zr-2.5Nb pressure tube samples. Three of the samples were taken from two different axial positions of a pressure tube that was neutron irradiated in a CANDU reactor for 25 years. The fourth sample was taken from an offcut of the same pressure tube but was not irradiated. The measured EBSD grain maps were imported into a CPFE model to simulate the state of the thermal residual stresses that develop in the last step of tube fabrication. This is to understand if there is any variation in the state of residual stresses as a function of tube axial position. Such variations can affect the diffusion of hydrogen into zirconium. In addition, since EBSD measurements are conducted on neutron irradiated samples, the effects of irradiation growth were added to the CPFE model to study their subsequent effects on the pre-existing thermal residual stresses.

4.2 Experimental Method

4.2.1 Sample

The samples were obtained from a CANDU pressure tube that was extruded at a 11:1 ratio at 817 °C followed by a 25% cold work. The tube was stress relieved at 425 °C for 24 hours and was placed in a reactor for 25 years. Four TEM foils were obtained from 3 different axial positions of the tube. Two of the TEM foils, S1 and S2, were taken from 0.09 m away from the front-end of the tube. The third foil was taken from 1.79 m away from the front-end. The last foil (AR) was taken from a front-end offcut of the same tube but was not irradiated. All samples were from the same radial position. It was estimated that samples S1 and S2 were exposed to a neutron fluence of 6 x 10^{25} n/m^2 whereas sample S3 were exposed to 17.9 x 10^{25} n/m^2. Table 4.1 provides a summary of the analyzed samples. The foils were cut from the radial-transverse surface of the pressure tube and were 2 mm thick. A schematic of the pressure tube and the coordinate system used are shown in Figure 4.1(a). All samples were electropolished in a solution of 90% methanol and 10% perchloric acid at -30 °C using 17 V DC current until the surface quality was suitable for EBSD measurements.

Table 4.1 Summary of the analyzed samples

Sample	Axial Position (m)	Neutron Fluence (n/m^2)	Number of Measured Maps	Average Map Size (µm x µm)
S1	**0.09**	**6 x 10^{25}**	**2**	**5.0 x 4.4**
S2	**0.09**	**6 x 10^{25}**	**2**	**4.7 x 4.1**
S3	**1.79**	**17.9 x 10^{25}**	**3**	**5.1 x 5.1**
AR	**Front end off-cut**	**N/A**	**2**	**5.2 x 4.6**

4.2.2 HR-EBSD Experiment

EBSD measurements were conducted at the Reactor Materials Testing Laboratory at Queen's University using a FEI FEG-SEM. The SE beam was set at 30 kV, with probe current of 20 nA. Sample-to-detector distance was set at 17 mm and Kikuchi patterns were collected every 25 nm. With the set-up used, it was possible to index α-Zr grains, but due to their very small size, β-phase grains were not indexed. For measuring relative elastic strain and rotation, the acquired Kikuchi patterns from each measurement point was cross correlated to a reference pattern selected within the same grain as discussed in [7]. An example of a Kikuchi pattern acquired from one of the neutron irradiated samples is shown in Figure 4.1(b).

Figure 4.1I shows an example of a radial stress, σ_R, map obtained from HR-EBSD analysis. As shown in Figure 4.1(a), RD, TD, and LD refer to the radial direction, transverse direction, and longitudinal direction, respectively. HR-EBSD measurements were conducted on the RD-TD surface of the pressure tube. The measured orientation maps used to calculate the (0002) and (11$\bar{2}$0) pole figures are shown in Figures 4.1(d)-4.1(g). It is observed that all samples are textured such that the basal plane normals (BPN) are mainly parallel to the TD, with a fewer BPNs pointing along the RD. There is nearly no BPN along the LD. In addition, the AR sample is the most transversely textured, followed by the S3, and S1 and S2 samples.

a. b.

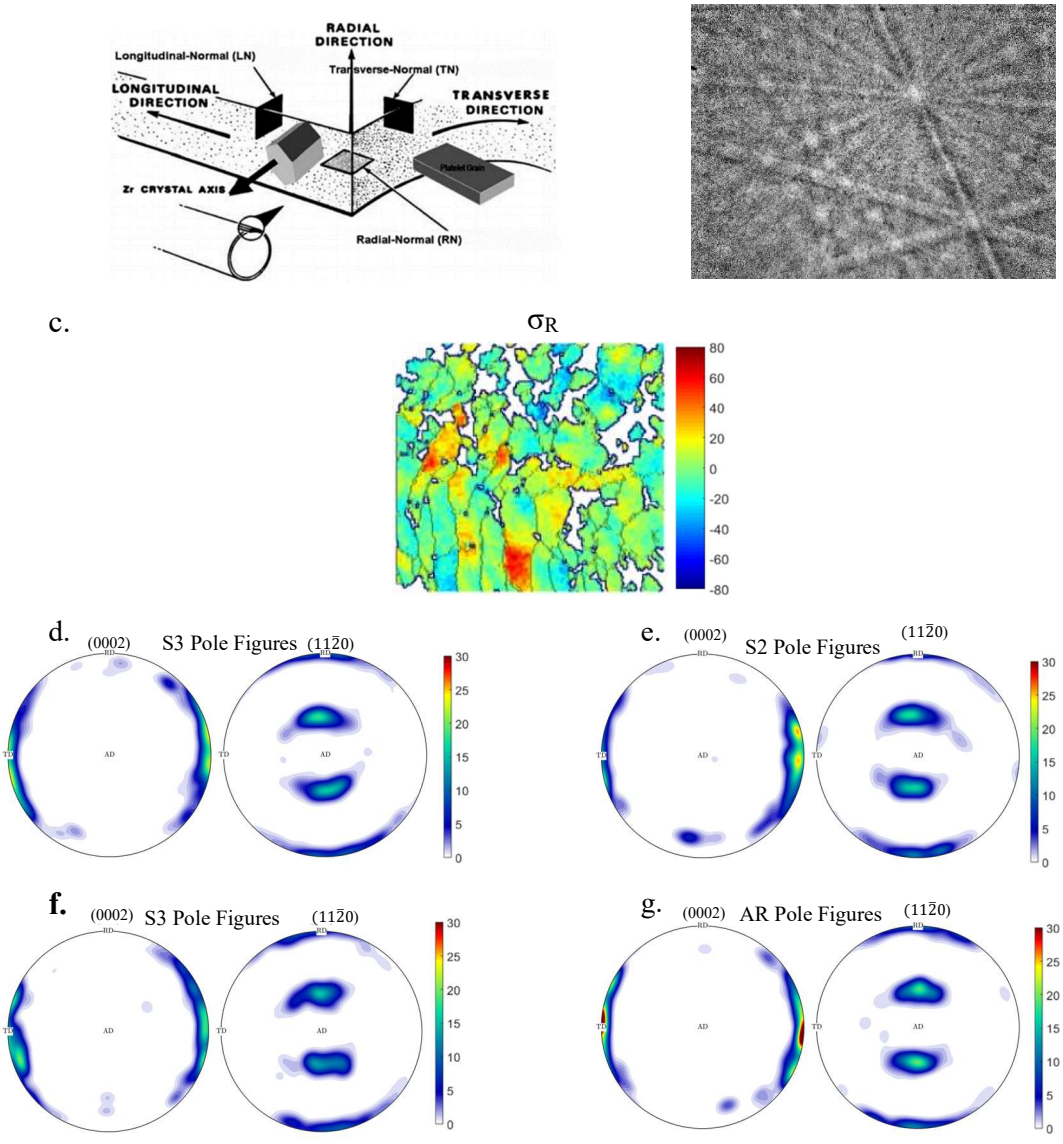

Figure 4.1 (a) A schematic of pressure tube and the coordinate system used in this paper. (b) An example of a Kikuchi pattern obtained from a neutron irradiated sample. (c) An example of relative σ_R stress measured by HR-EBSD (c) Measured pole figures for (d) S1, (e) S2, (f) S3, and (g) AR samples.

4.3 CPFE Model

The three EBSD maps shown in Figures 4.2(a)-4.2(c) were imported to ABAQUS FE solver for CPFE modeling. These maps are respectively shown in Figures 4.2(d)-4.2(f). The first map is from sample S1, the second map is from sample S3, and the third map is from the unirradiated AR sample. Examples of transverse stress, σ_T, maps obtained from CPFE simulations are provided in Figures 4.2(g)-4.2(i).

Symmetry boundary conditions were applied onto the RD, TD, and LD faces of the models. C3D8 mesh elements were used for all simulations. To mesh samples S1, S3, and AR, respectively 64490, 26640, and 26000 elements were used.

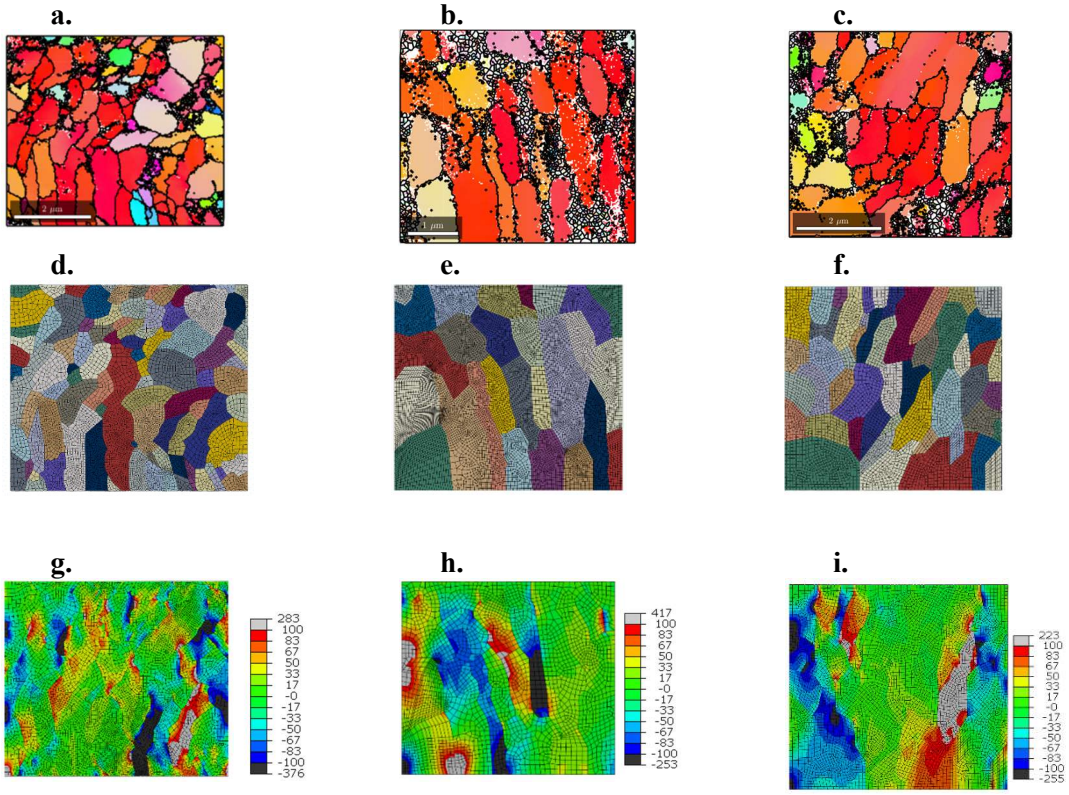

Figure 4.2 EBSD maps of (a) sample S1, (b) sample S3, and (c) AR sample with their corresponding reconstructed CPFE models shown in (d) I(e), respectively. The results of CPFE modeling for σ_T stress (in MPa) for (g) sample S1, (h) sample S3, and (i) sample AR.

The crystal plasticity user material (UMAT) subroutine developed by Abdolvand et al [24] was modified to incorporate the effects of irradiation growth. At the beginning of each time increment, the FE solver provides UMAT with total strain, rotation, and time increments as well as the solution dependent state variables. The total strain increment ($\Delta\varepsilon^{\mathrm{tot}}$) can be written as:

$$\Delta\varepsilon_{ij}^{tot} = \Delta\varepsilon_{ij}^{el} + \Delta\varepsilon_{ij}^{pl} + \Delta\varepsilon_{ij}^{th} + \Delta\varepsilon_{ij}^{growth} \quad (1)$$

where $\Delta\varepsilon_{ij}^{el}$, $\Delta\varepsilon_{ij}^{pl}$, $\Delta\varepsilon_{ij}^{th}$, and $\Delta\varepsilon_{ij}^{growth}$ respectively are the increments of elastic strain, plastic strain induced by crystallographic slip, thermal strain, and the irradiation growth increment.

The thermal strain increment is calculated by:

$$\Delta\varepsilon_{\mathrm{ij}}^{\mathrm{th}} = \alpha_{\mathrm{ij}}\Delta\mathrm{T} \quad (2)$$

where α_{ij} is the coefficient of thermal expansion (CTE). For the α-Zr with HCP crystal structure α_{ij} is $10.1 \times 10^{-6}\ \mathrm{K}^{-1}$ along the crystal c-axis and $5.3 \times 10^{-6}\ \mathrm{K}^{-1}$ along the a-axis [25]. The plastic strain increment is calculated by:

$$\Delta\varepsilon_{ij}^{pl} = \sum_{\alpha=1}^{N^{spl}} P_{ij}^{\alpha}\dot{\gamma}^{\alpha}\,\Delta\mathrm{t}$$
$$P^{\alpha} = sym(S^{\alpha})\ where\ S^{\alpha} = d^{\alpha} \otimes n^{\alpha} \quad (3)$$

where P_{ij}^{α} is the symmetric part of the Schmid tensor (S^{α}) for the slip system α, $\dot{\gamma}^{\alpha}$ is the slip rate, d^{α} and n^{α} are respectively the slip direction and normal to the slip plane for the system α. The slip rate of the system α is calculated as [26]:

$$\dot{\gamma}^{\alpha} = \dot{\gamma}_0 \left|\frac{\tau^{\alpha}}{g^{\alpha}}\right|^{n} sign\left(\frac{\tau^{\alpha}}{g^{\alpha}}\right) \quad (4)$$

where $\dot{\gamma}_0$ is a reference shear strain rate, τ^{α} is the resolved shear stress acting on the slip system α, and g^{α} is the current critical resolved shear stress (CRSS) of the slip system α. The initial CRSS values used in the simulations are 120 MPa, 168 MPa, and 331 MPa for prism $\langle 11\bar{2}0\rangle$, basal $\langle 11\bar{2}0\rangle$, and pyramidal $\langle 11\bar{2}3\rangle$ slip systems, respectively [24].

The experimental data reported by Holt et al. [27] were used to develop an empirical equation for the irradiation growth strain as a function of fluence using a single crystal

model. The measurements were done on polycrystalline Zr-2.5Nb material, but since most of the HCP crystals c-axis are oriented toward TD, it is assumed that the measured growth strain along TD and LD represent growth strain along the HCP crystal c- and a-axis, respectively. Hence the following equations in the HCP crystal coordinate are fitted:

$$\Delta\varepsilon_c^{\text{growth}} = \mathrm{A_c}\Delta\varphi^2 + \mathrm{B_c}\Delta\varphi$$
$$\Delta\varepsilon_a^{\text{growth}} = \mathrm{A}_a\Delta\varphi^2 + \mathrm{B}_a\Delta\varphi \quad (5)$$

where $\mathrm{A_c}$, $\mathrm{B_c}$, A_a,and B_a are materials constants and $\Delta\varphi$ is the fluence increment. The subscripts a and c correspond to the HCP crystal a-axis and c-axis, respectively. Since the time increment at each step is provided by the FE solver, a correlation between $\Delta\varphi$ and time increment is made assuming that the in-reactor neutron fluence experienced by each sample was constant over 25 years. It was determined that for sample S3 located 1.79 m from the front-end $\dot{\varphi}$ was 2.27×10^{17} $\frac{\mathrm{n}}{\mathrm{m^2 * s}}$. Hence, Eq. 5, can be re-written as:

$$\Delta\varepsilon_c^{\text{growth}} = \mathrm{A}_c(2.27 \times 10^{17}\Delta\mathrm{t})^2 + \mathrm{B}_c(2.27 \times 10^{17}\Delta\mathrm{t})$$
$$\Delta\varepsilon_a^{\text{growth}} = \mathrm{A}_a(2.27 \times 10^{17}\Delta\mathrm{t})^2 + \mathrm{B}_a(2.27 \times 10^{17}\Delta\mathrm{t}) \quad (6)$$

where $\Delta\mathrm{t}$ is the time increment provided by the FE solver. The coefficients of Eq. 6 are calibrated using the single crystal model. The results of the parameter calibration efforts are shown in Figure 4.3 with the calibrated parameters provided in Table 4.2. Calibration was done for sample S3 since it experienced a higher irradiation dosage. The parameters fitted in Eq. 6 were used for modeling irradiation growth of sample S1, yet a time-equivalent of 8.3 years was used to replicate the measured fluence of 6 x 10^{25} n/m^2. To calculate $\Delta\varepsilon_{ij}^{growth}$, the EBSD measured orientations were used to calculate the rotation matrix and to transform the growth strains from the local crystal coordinates to the global coordinates.

Table 4.2 Irradiation growth coefficients

	c-axis		**a-axis**	
Map	**$\mathrm{A_c}$ ($\frac{\mathrm{m^2}}{\mathrm{n*s}}$)**	**$\mathrm{B_c}$ ($\frac{\mathrm{m^2}}{\mathrm{n*s}}$)**	**$\mathrm{A_a}$ ($\frac{\mathrm{m^2}}{\mathrm{n*s}}$)**	**$\mathrm{B_a}$ ($\frac{\mathrm{m^2}}{\mathrm{n*s}}$)**
S3	**-8.81 x 10^{-37}**	**-1.76 x 10^{-27}**	**1.76 x 10^{-36}**	**3.08 x 10^{-27}**

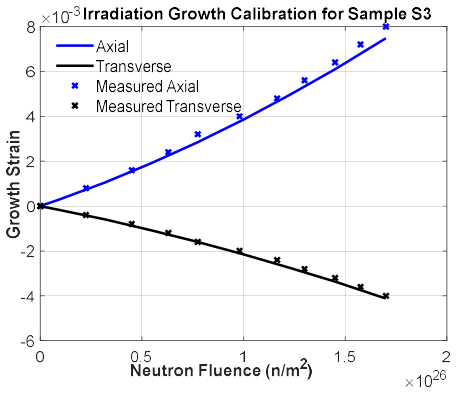

Figure 4.3 Comparison between calculated and measured growth strain after calibrating the parameters of Eq. 6.

The elastic strain increment is calculated by reducing the thermal, plastic, and growth strain increments from the total strain increment. Once the elastic strain is calculated, the stress tensor is defined as:

$$\Delta\sigma_{ij} = C_{ijkl}\Delta\varepsilon_{kl} \quad (7)$$

where C_{ijkl} is the stiffness tensor of α-Zr. The elastic modulus used in the model are the ones that are determined by Fisher and Renken [28]: C_{1111} = 143.5 GPa, C_{3333} = 164.9 GPa, C_{1122} = 72.5 GPa, C_{1133} = 65.4 GPa, and C_{2323} = 32.1 GPa.

Several scenarios that affect the state of residual stresses are examined. First, the thermal residual stresses that develop during the last step of tube fabrication are modeled by simply cooling the FE models from 450 °C to room temperature. This was followed by investigating the state of residual stresses induced only by irradiation growth. The applied boundary conditions for both models were the same since irradiation growth is the dimensional change under no externally applied stress. In the last set of simulations, both thermal and irradiation growth effects are studied. No significant plastic strain induced by crystallographic slip was observed in FE simulations.

4.4 Results and Discussion

In this section, the results obtained from HR-EBSD and CPFE are presented and discussed. The stresses are given in the global coordinates unless stated otherwise. σ_R and σ_T respectively refer to the radial and transverse normal stresses, σ_{RT} refers to the radial-transverse shear stress, and σ_H refers to the hydrostatic stress. ω_{RT} refers to the radial-transverse elastic lattice rotation.

4.4.1 HR-EBSD Results

Two maps and 129 grains from sample S1 were measured with average map size of 5.0 µm x 4.4 µm. For sample S2, two maps and 136 grains were measured with the average map size of 4.7 µm x 4.1 µm. For sample S3, three maps that cover 114 grains were measured with the average map size of 5.1 µm x 5.1 µm. Lastly, for the AR sample, two maps and 92 grains were measured with the average map size of 5.2 µm x 4.6 µm. Only grains with 50 or more measurement points (pixels) are considered in the following analysis. Since with HR-EBSD relative stresses and rotations are measured, in this section, the variations of stresses are studied. Absolute stresses are discussed in the CPFE modeling section. As shown in Figure 4.4(a), stress variations are characterized by calculating the full width at half maximum (FWHM) of the stress distributions within each grain. The FWHM of the stress distributions correlates with the intragranular stress variations. Table 4.3 shows the average FWHM extracted from HR-EBSD measurements from all grains measured in each map.

HR-EBSD results show that the distributions of the relative stresses and elastic rotations for the AR sample are the lowest, followed by sample S3. The grains of samples S1 and S2, at the front-end of the pressure tube, experience the largest stress variations. This is significant as such stress variations affect the diffusion of hydrogen atoms and sequence of hydride formation [29]. In addition, these results show that there is a correlation between the propensity of the BPNs and stress distribution within grains. The highly textured samples, S3 and AR, have lower stress distribution compared to the less textured samples S1 and S2. The effect of the texture on stresses originates from the “mismatch” in elastic, thermal, and plastic properties of each grain. A specimen with a sharper texture has more

grains oriented in the same direction; hence lower localized stresses develop. Also, for all samples, σ_T is greater than σ_R since the c-axis of most of the HCP crystals is oriented towards TD.

Table 4.3 Summary of HR-EBSD results

Map	Average FWHM of σ_R (MPa)	Average FWHM of σ_T (MPa)	Average FWHM of σ_{RT} (MPa)	Average FWHM of ω_{RT} (rad, x 10^{-4})
Sample S1 Map 1	**18.0**	**41.5**	**32.8**	**2.03**
Sample S1 Map 2	**15.0**	**39.2**	**28.3**	**2.07**
Sample S2 Map 1	**13.9**	**27.8**	**25.5**	**1.86**
Sample S2 Map 2	**13.8**	**38.5**	**36.12**	**1.89**
Sample S3 map 1	**15.0**	**27.6**	**13.0**	**1.55**
Sample S3 map 2	**16.0**	**29.1**	**12.2**	**1.70**
Sample S3 map 3	**14.8**	**28.5**	**16.9**	**1.85**
AR Sample Map 1	**12.7**	**22.0**	**21.0**	**0.95**
AR Sample Map 2	**14.5**	**28.7**	**16.5**	**1.66**

4.4.2 Effects of thermal residual stresses

To characterize the possible variation of stresses with axial position along the pressure tube, different modeling scenarios are examined. In this first case, only the effects of the thermal residual stresses that develop in the last step of the manufacturing process is studied. In this model, called T-model, all samples were cooled from 450 °C to the room temperature at a rate of 1 °C/min. No additional load was applied to the models, i.e. $\Delta\varepsilon^{\text{growth}} = 0$, and no slip activity was observed in the FE simulations.

Figures 4.4(a)-4.4(b) show the distribution of stresses calculated at each integration point at the end of simulation for all modeled samples. It is shown that all maps have an average stress of 0 which is expected as no external load is applied. The overall stress variation of the model is characterized by the FWHM of the distribution curves in Figures 4.4(a)-4.4(b).

In these figures, the stresses from all integration points of the FE models are plotted; as such, the effects of the localized stresses are homogenized and are reflected in the in the tails of the distribution curves. To have a better understanding of such localized stresses, the stress calculated at all integration points assigned to each grain is firstly plotted from which, FWHM are subsequently calculated. All these values for all grains of each sample are then collected and presented in a single histogram shown in Figures 4.4(c) and 4.4(d). Table 4.4 reports the overall stress variation and average intragranular stress variation calculated in each map. The S1 map develops the highest overall stress variation followed by the AR map. For intragranular stress variation, the least variation is observed in the AR map, and the highest variation is observed by the S1 map.

Table 4.4 Summary of the CPFE results for the T-model

Modeled Map	Overall Stress Variation			Average Intragranular Stress Variation		
	σ_R (MPa)	σ_T (MPa)	σ_H (MPa)	σ_R (MPa)	σ_T (MPa)	σ_H (MPa)
S1 Map	**105.9**	**127.3**	**82.5**	**72.3**	**72.4**	**55.0**
S3 Map	**62.5**	**120.9**	**68.6**	**40.9**	**62.1**	**37.2**
AR Map	**98.0**	**127.7**	**83.6**	**46.7**	**43.2**	**32.8**

The intragranular stress variation trends captured by the CPFE model match the stress variation trends measured in HR-EBSD experiment, i.e., the most textured sample has the least stress variation compared to the less textured samples. These results show that, for the intragranular stresses, the intergranular misorientation and average texture are the main parameters that affect the magnitude of the stresses that arise from the heat treatment of the pressure tube. This observation is in agreement with the recent 3D-XRD residual stress measurements conducted on pure Zr [30].

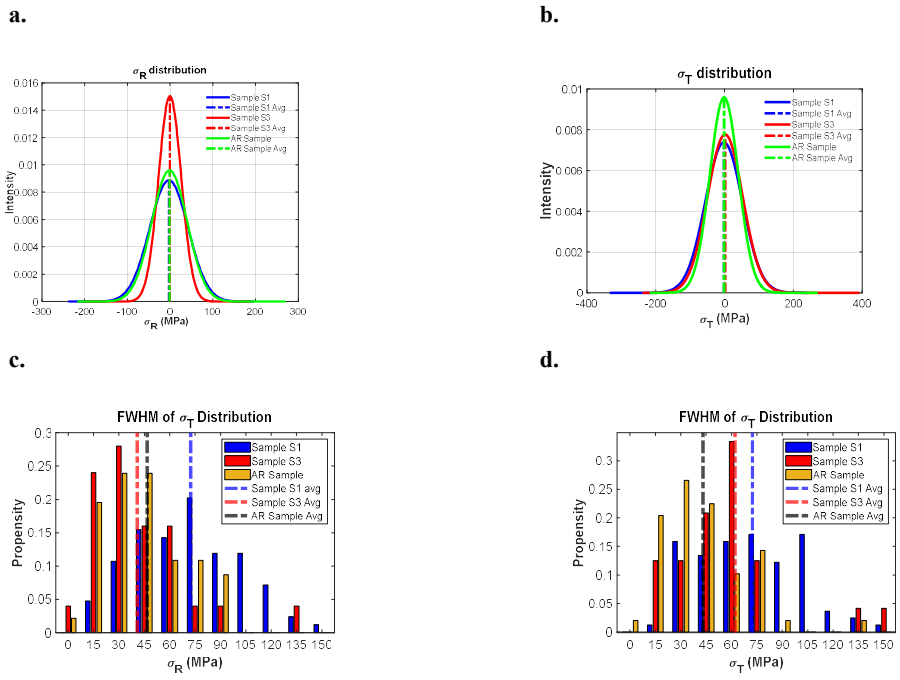

Figure 4.4 CPFE results: the distribution of (a) σR and (b) σT from all integration points assigned to samples S1, S3, and AR. Histograms of the FWHM distribution of (c) σR and (d) σT for individual grains for all grains of samples S1, S3, and AR.

4.4.3 Effects of Irradiation Growth

Only samples S1 and S3 are considered in the irradiation growth simulations since they are the neutron irradiated samples. These models are called G-model in which irradiation growth strain is applied to the models, but no thermal strain, i.e. $\Delta\varepsilon^{th} = 0$. Two sets of simulations are performed to analyze the effects of texture and neutron fluence on the local stresses induced by irradiation growth.

4.4.3.1 Texture and Irradiation Growth

In the first set of simulations, called G1-model, the same fluence is applied to both samples to only study the effects of texture. The applied neutron fluence is 6 x 10^{25} n/m^2 which is the measured fluence for sample S1. Figures 4.5(a)-4.5(b) show the stress distribution from all integration points. The average stress in both samples is 0. Figures 4.5(c)-4.5(d) show the distribution of intragranular stress variation for both maps. Table 4.5 shows a summary of the overall stress variation as well as the average intragranular stress variation for each map.

Table 4.5 Summary of the CPFE results for G1-Model

Modeled Map	Overall Stress Variation			Average Intragranular Stress Variation		
	σ_R (MPa)	σ_T (MPa)	σ_H (MPa)	σ_R (MPa)	σ_T (MPa)	σ_H (MPa)
S1 Map	**114.8**	**132.7**	**89.8**	**78.2**	**78.1**	**59.6**
S3 Map	**76.1**	**140.2**	**82.3**	**50.2**	**72.3**	**44.8**

Due to being less textured, sample S1 develops a higher overall stress variation. It is also notable that the magnitude of the stress variation is within 15% of that extracted from the heat-treatment model (T-Model). That is, the stresses develop due to heat treatment and those develop due to irradiation growth are in same order at the front-end of the pressure tube. Similar to the T-model, the variation of localized intragranular stresses are higher for S1. The results from the G1-model show that, for samples with equal fluence, the texture is the main parameter that affects the magnitude of localized stresses that develop from irradiation growth. The more textured sample develops lower stresses.

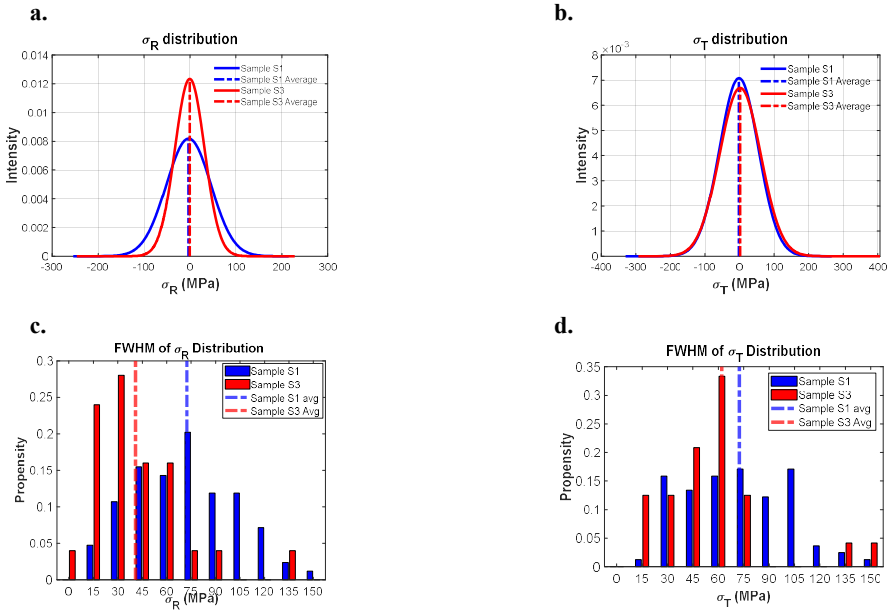

Figure 4.5 CPFE results: the distribution of (a) σ_R and (b) σ_T from all integration points assigned to samples S1, S3, and AR. Histograms of the FWHM distribution of (c) σ_R and (d) σ_T for individual grains for all grains of samples S1, and S3.

4.4.3.2 Fluence and Irradiation Growth

In the second set of simulations, called G2-model, the actual measured fluences at each axial position are applied. The neutron fluence experienced by each sample is provided in Table 4.1.

Table 4.6 Summary of the CPFE results for G2-Model

Modeled Map	Overall Stress Variation			Average Intragranular Stress Variation		
	σ_R (MPa)	σ_T (MPa)	σ_H (MPa)	σ_R (MPa)	σ_T (MPa)	σ_H (MPa)
S1 Map	**114.8**	**132.7**	**89.8**	**78.2**	**78.1**	**59.6**
S3 Map	**179.0**	**311.0**	**191.4**	**123.4**	**179.0**	**117.3**

Figures 4.6 shows stress distributions, and Table 4.6 shows a summary of the overall stress variation as well as the average intragranular stress variation for each map. Note that the results obtained for the sample S1 remain the same as the G1-model since the fluence applied is the same. Both the overall and intragranular stresses for sample S3 under "as-measured" neutron fluence are higher than those calculated for sample S1. This is not in agreement with the experimental measurements (see section 4.5). These results indicate that the higher neutron fluence, that occur with distancing from the front end of the tube, is the major factor affecting the state of the stresses, not the texture. Also, at higher fluences, the developed stresses from irradiation growth are much higher than those developed from the heat treatment.

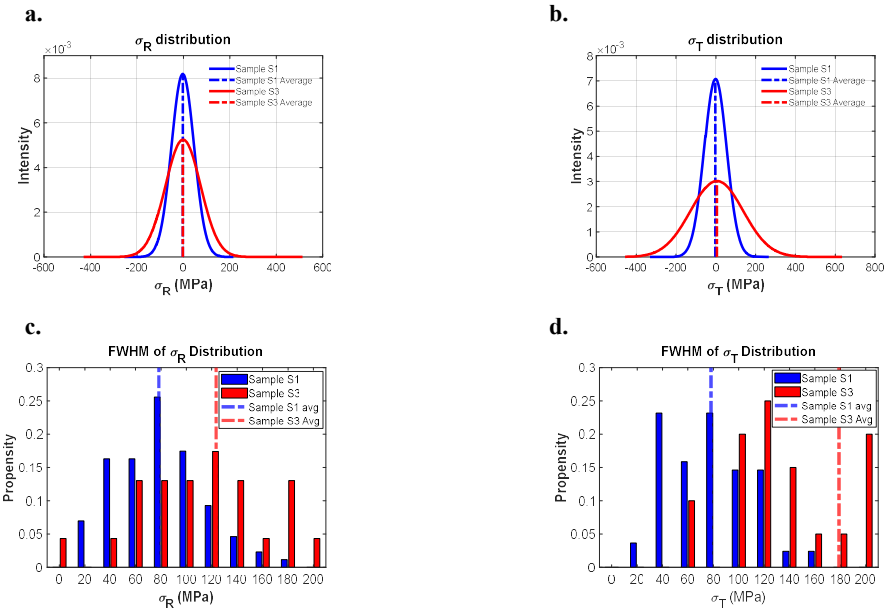

Figure 4.6 CPFE results: the distribution of (a) σ_R and (b) σ_T from all integration points assigned to samples S1, S3, and AR. Histograms of the FWHM distribution of (c) σ_R and (d) σ_T for individual grains for all grains of samples S1, and S3.

4.4.4 Effects of Combined Loading

In the combined loading models, called C-model, samples are cooled down from 450 °C to room temperature at a rate of 1 °C/min, and then the irradiation growth strain is applied. Similar to the G-model, two sets of simulations are considered here. In the first set, called C1-model, it is assumed that both S1 and S3 are exposed to the same neutron fluence. This is to examine the effects of materials texture. In the second set, called C2-model, the actual measured fluences are applied to each sample.

4.4.4.1 Texture and Combined Loading

Figure 4.7 show the distribution of stresses for both maps and Table 4.7 provides a summary of the results. The results of the C1-model show that material texture is the main parameter affecting both intragranular and overall stresses, with the more textured sample developing lower stresses.

Table 4.7 Summary of the CPFE results for C1-Model

Modeled Map	Overall Stress Variation			Average Intragranular Stress Variation		
	σ_R (MPa)	σ_T (MPa)	σ_H (MPa)	σ_R (MPa)	σ_T (MPa)	σ_H (MPa)
S1 Map	**171.2**	**190.2**	**135.2**	**117.7**	**115.0**	**91.2**
S3 Map	**118.6**	**208.9**	**125.6**	**78.1**	**112.3**	**71.2**

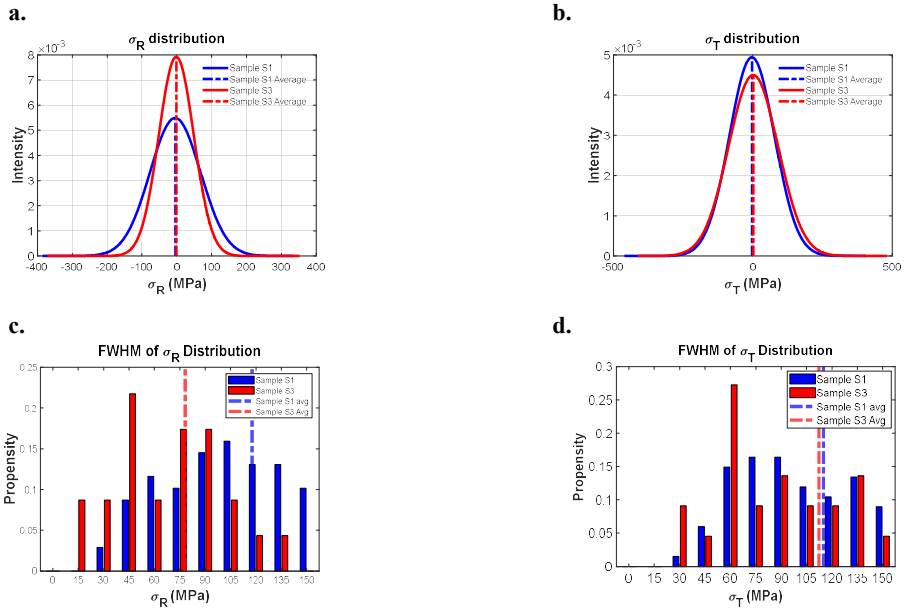

Figure 4.7 . CPFE results: the distribution of (a) σ_R and (b) σ_T from all integration points assigned to samples S1, S3, and AR. Histograms of the FWHM distribution of (c) σ_R and (d) σ_T for individual grains for all grains of samples S1, and S3.

4.4.4.2 Fluence and Combined Loading

Figure 4.8 show the distribution of stresses at each integration points of both models and Table 4.8 provides a summary of the results. The results for the S1 map remain unchanged. The C2-model shows that higher neutron fluences are the main parameter affecting the intragranular stresses that develop in regions away from the front-end of the pressure tube.

Table 4.8 Summary of the C2-Model Results

Modeled Map	Overall Stress Variation			Average Intragranular Stress Variation		
	σ_R (MPa)	σ_T (MPa)	σ_H (MPa)	σ_R (MPa)	σ_T (MPa)	σ_H (MPa)
S1 Map	**171.2**	**190.2**	**135.2**	**117.7**	**115.0**	**91.2**
S3 Map	**184.7**	**319.6**	**197.5**	**127.6**	**182.9**	**122.3**

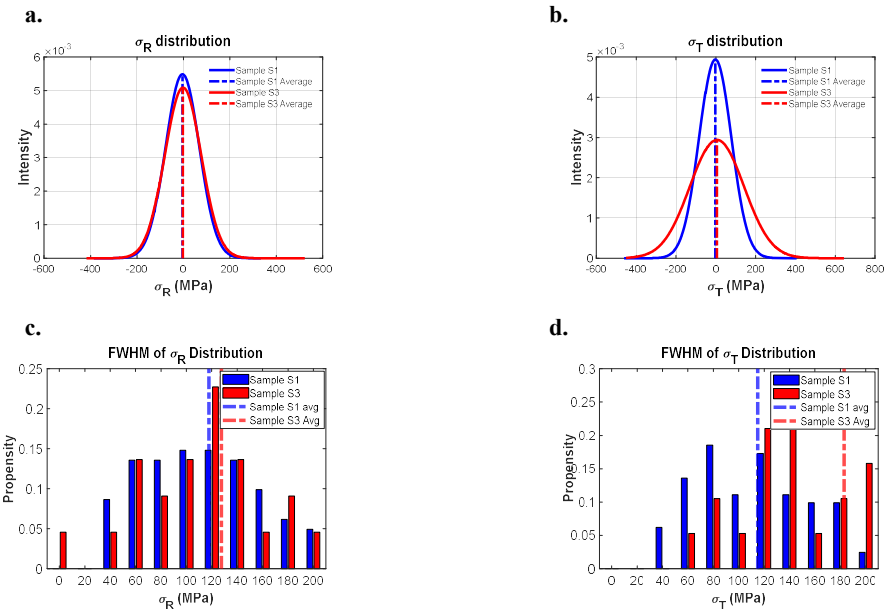

Figure 4.8 CPFE results: the distribution of (a) σ_R and (b) σ_T from all integration points assigned to samples S1, S3, and AR. Histograms of the FWHM distribution of (c) σ_R and (d) σ_T for individual grains for all grains of samples S1, and S3.

4.4.5 CPFE vs HR-EBSD Results

It is shown in previous sections that the CPFE numerical results for the T-model, G1-model, and C1-model are consistent with those observed in the HR-EBSD results. However, when the as-measured neutron fluence for the sample S3 is used, the G2-model and C2-model show different trends than those obtained by HR-EBSD. Many parameters contribute to the observed discrepancy. For example, EBSD allows for measuring surface grains, not the subsurface grains. The interaction of the subsurface grains with the surface grains can have significant effects on the developed stresses in the CPFE model [31], [32]. In addition, no β-Zr was indexed with EBSD, thus the β-Zr grains are excluded from CPFE simulations, and their effects on the developed stresses are not present. Unindexed points may also contribute to the observed discrepancy. These data points are apparent in FiguI4.2(c), and sample S3 was the most affected one, comparing to samples S1, S2, and

AR. These data points are removed from the analysis conducted on HR-EBSD measurements which could be one of the reasons for obtaining lower average FWHMs for the sample S3. Also, when importing the EBSD maps into the CPFE models, the orientations of these data points are unknown, and assumptions are made to extend the size of the closest neighboring grain to cover the unindexed points. Finally, the neutron irradiated samples are obtained from CANDU pressure tube which was in service for 25 years. At the operating conditions, CANDU pressure tubes undergo ~130 MPa hoop stress and ~75 MPa axial stress. The effects of these stresses are reflected in the experimental results but not in the CPFE results. Authors are currently including the effects of irradiation hardening, softening, and irradiation-enhanced creep to the CPFE model.

In Figure 9 the results obtained from the T-model and C2-model are compared to those measured with HR-EBSD. To provide a like-to-like comparison, the reference point values are reduced from the CPFE results. The reference points are shown by red dots in Figure 4.I), 4.9(e), 4.9(i), and 4.9(m). It is shown that, the T-model can generally capture the experimental trends, with the C-model slightly improving them. An example of such cases is shown Figure 4.9(c), where the T-model captures the trends observed for σ_T; however, the C2-model adds a region of stress concentration, shown by the blue circle, that is consistent with the measurement. Another example of such grains is shown in Figure 4.9(h). There is a region of high relative elastic rotation, as shown with a red circle, in the results of the T-model that is not present in the experimental result. This region of high elastic rotation is not present in the result from the C2-model.

There are cases where the T-model fails to capture the trends that are observed by HR-EBSD measurement; however, when the C2-model is used, such trends are captured. For example, it is shown in Figure 4.9(l) that the T-model predicts negative ω_{RT} at the north part of the grain, while both C2-model and HR-EBSD show a positive ω_{RT} for the same region. Finally, as discussed earlier in this section, there are grains that both the C2-model and T-model fail to capture the trends obtained by HR-EBSD e.g. Figure 4.9(f).

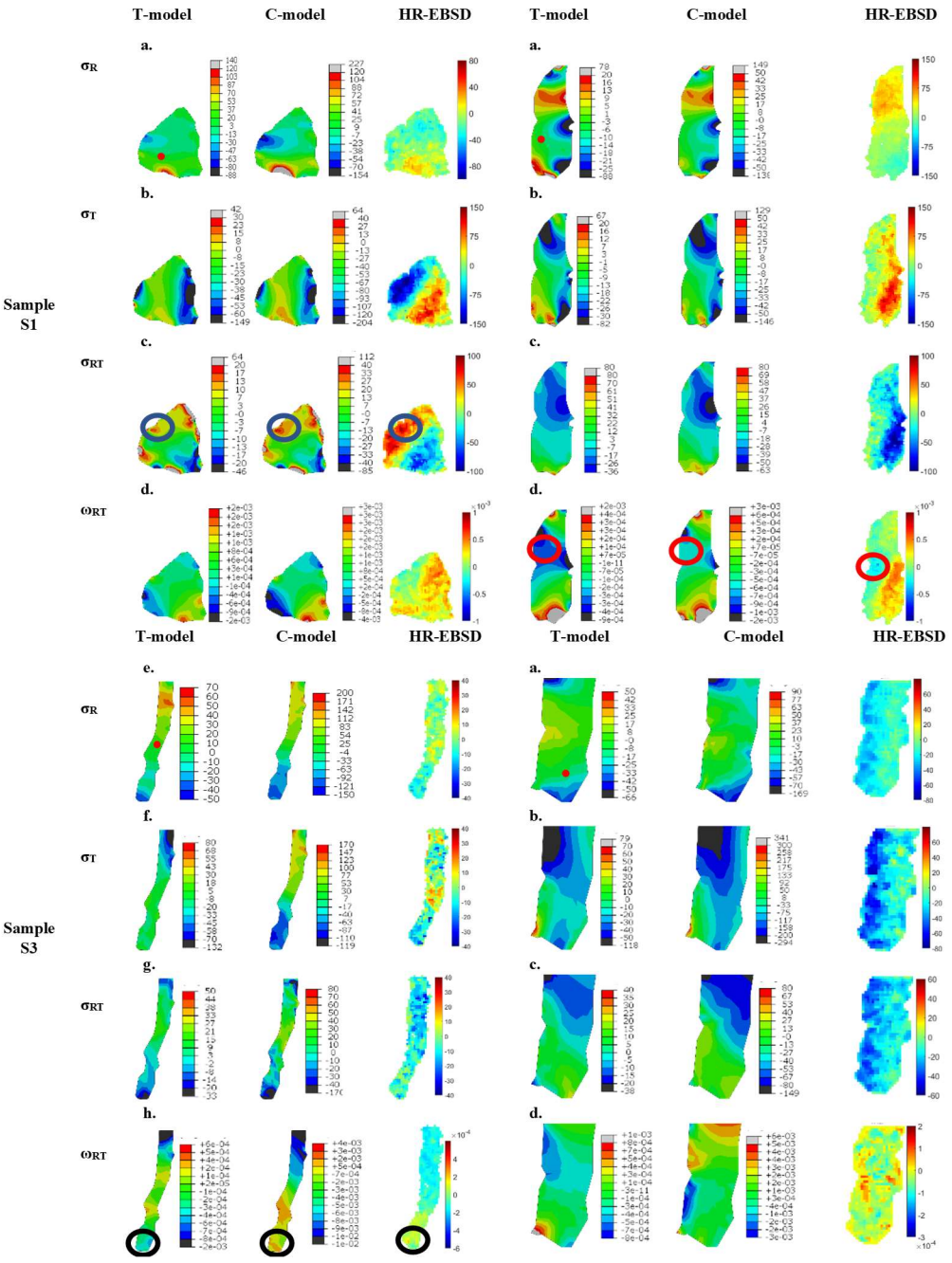

Figure 4.9 A comparison of relative stress and elastic rotation variation trends obtained from CPFE models and HR-EBSD. The first column shows the sample from which the grains are obtained. The second column shows the stress and elastic rotation components examined. The stresses and elastic rotation from CPFE are shown after reducing the reference point values. The reference points are shown by the red dots. The stresses are reported in MPa and elastic rotations are reported in radians.

4.5 Conclusion

The state of the residual stresses that develop in a CANDU pressure tube during fabrication process was studied in this paper. Samples were taken from two axial positions of a neutron irradiated tube and from an offcut of the same tube, but not irradiated. CPFE and HR-EBSD methods were used to assess the state of the residual stresses. The EBSD measured grain maps were imported into a CPFE model and different simulation scenarios were examined. All analyses were conducted at the front-end and 1.7 m from the front-end of the tube, from which the following conclusions were made:

a. The experimental results show that stress variations decrease with distancing from the front-end of the tube indicating that higher localized stresses develop at the front-end.
b. CPFE results show that the thermal residual stresses that develop from the heat treatment process are mainly affected by intergranular misorientation and texture of the samples. Samples located at the front-end of the tube had highest intergranular misorientation as well as highest thermal residual stresses.
c. Similarly, under the same neutron fluence, the CPFE model predicts higher stresses at the front-end, yet when the as measured fluences are used, the middle of the tube undergoes higher stresses.
d. For the axial position located at 1.7 m from the front-end, the effects of irradiation growth overcomes thermal residual stresses.
e. Using the neutron fluence measured for the front-end of the tube, the stresses that develop from irradiation growth are in the same order as those that develop from heat treatment. At higher fluences, the stresses that develop from irradiation growth are higher than thermal stresses.

4.6 References

[1] V. Perovic, G. C. Weatherly, S. R. MacEwen, and M. Leger, "The influence of prior deformation on hydride precipitation in zircaloy," *Acta Metall. Mater.*, 1992, doi: 10.1016/0956-7151(92)90310-B.

[2] F. Long *et al.*, "Effect of neutron irradiation on deformation mechanisms operating during tensile testing of Zr-2.5Nb," *Acta Mater.*, 2016, doi: 10.1016/j.actamat.2015.09.032.

[3] Q. Wang, C. Cochrane, F. Long, H. Yu, and M. R. Daymond, "Micropillar compression study on heavy ion irradiated Zr-2.5Nb pressure tube alloy," *J. Nucl. Mater.*, 2018, doi: 10.1016/j.jnucmat.2018.09.021.

[4] Q. Dong, H. Qin, Z. Yao, Q. Wang, and M. R. Daymond, "Effect of the addition of Cu on irradiation induced defects and hardening in Zr-Nb alloys," *J. Nucl. Mater.*, 2019, doi: 10.1016/j.jnucmat.2019.03.025.

[5] D. Khatamian, A. Shaddick, and V. F. Urbanic, "Influence of neutron irradiation on H diffusion in Zr-2.5Nb alloy," *J. Alloys Compd.*, 1999, doi: 10.1016/S0925-8388(99)00372-2.

[6] A. J. Wilkinson, "Measurement of elastic strains and small lattice rotations using electron back scatter diffraction," *Ultramicroscopy*, 1996, doi: 10.1016/0304-3991(95)00152-2.

[7] A. J. Wilkinson, G. Meaden, and D. J. Dingley, "High-resolution elastic strain measurement from electron backscatter diffraction patterns: New levels of sensitivity," *Ultramicroscopy*, 2006, doi: 10.1016/j.ultramic.2005.10.001.

[8] T. B. Britton and A. J. Wilkinson, "High resolution electron backscatter diffraction measurements of elastic strain variations in the presence of larger lattice rotations," *Ultramicroscopy*, 2012, doi: 10.1016/j.ultramic.2012.01.004.

[9] V. Tong, J. Jiang, A. J. Wilkinson, and T. Ben Britton, "The effect of pattern overlap on the accuracy of high resolution electron backscatter diffraction measurements," *Ultramicroscopy*, 2015, doi: 10.1016/j.ultramic.2015.04.019.

[10] Z. Zhang, D. Lunt, H. Abdolvand, A. J. Wilkinson, M. Preuss, and F. P. E. Dunne, "Quantitative investigation of micro slip and localization in polycrystalline materials under uniaxial tension," *Int. J. Plast.*, 2018, doi: 10.1016/j.ijplas.2018.04.014.

[11] J. Jiang, J. Yang, T. Zhang, F. P. E. Dunne, and T. Ben Britton, "On the mechanistic basis of fatigue crack nucleation in Ni superalloy containing inclusions using high resolution electron backscatter diffraction," *Acta Mater.*, 2015, doi: 10.1016/j.actamat.2015.06.035.

[12] Y. Guo, T. B. Britton, and A. J. Wilkinson, “Slip band-grain boundary interactions in commercial-purity titanium,” *Acta Mater.*, 2014, doi: 10.1016/j.actamat.2014.05.015.

[13] Y. Guo *et al.*, “Measurements of stress fields near a grain boundary: Exploring blocked arrays of dislocations in 3D,” *Acta Mater.*, 2015, doi: 10.1016/j.actamat.2015.05.041.

[14] D. C. Johnson, B. Kuhr, D. Farkas, and G. S. Was, “Quantitative analysis of localized stresses in irradiated stainless steels using high resolution electron backscatter diffraction and molecular dynamics modeling,” *Scr. Mater.*, 2016, doi: 10.1016/j.scriptamat.2016.01.017.

[15] M. Christensen *et al.*, “Vacancy loops in Breakaway Irradiation Growth of zirconium: Insight from atomistic simulations,” *J. Nucl. Mater.*, 2020, doi: 10.1016/j.jnucmat.2019.151946.

[16] B. Christiaen, C. Domain, L. Thuinet, A. Ambard, and A. Legris, “A new scenario for ‹c› vacancy loop formation in zirconium based on atomic-scale modeling,” *Acta Mater.*, 2019, doi: 10.1016/j.actamat.2019.07.030.

[17] S. Di, Z. Yao, M. R. Daymond, X. Zu, S. Peng, and F. Gao, “Dislocation-accelerated void formation under irradiation in zirconium,” *Acta Mater.*, 2015, doi: 10.1016/j.actamat.2014.09.020.

[18] S. Di, Z. Yao, M. R. Daymond, and F. Gao, “Molecular dynamics simulations of irradiation cascades in alpha-zirconium under macroscopic strain,” *Nucl. Instruments Methods Phys. Res. Sect. B Beam Interact. with Mater. Atoms*, 2013, doi: 10.1016/j.nimb.2013.01.048.

[19] A. Patra, C. N. Tomé, and S. I. Golubov, “Crystal plasticity modeling of irradiation growth in Zircaloy-2,” *Philos. Mag.*, 2017, doi: 10.1080/14786435.2017.1324648.

[20] R. Montgomery, C. Tomé, W. Liu, A. Alankar, G. Subramanian, and C. Stanek, “Use of multiscale zirconium alloy deformation models in nuclear fuel behavior analysis,” *J. Comput. Phys.*, 2017, doi: 10.1016/j.jcp.2016.09.051.

[21] Q. Wang, C. Cochrane, T. Skippon, Z. Wang, H. Abdolvand, and M. R. Daymond, “Orientation-dependent irradiation hardening in pure Zr studied by nanoindentation, electron microscopies, and crystal plasticity finite element modeling,” *Int. J. Plast.*, 2020, doi: 10.1016/j.ijplas.2019.08.007.

[22] H. Abdolvand, M. Majkut, J. Oddershede, J. P. Wright, and M. R. Daymond, “Study of 3-D stress development in parent and twin pairs of a hexagonal close-packed polycryst–l: Part II - Crystal plasticity finite element modeling,” *Acta Mater.*, 2015, doi: 10.1016/j.actamat.2015.04.025.

[23] J. Gong, T. Benjamin Britton, M. A. Cuddihy, F. P. E. Dunne, and A. J. Wilkinson, "(a) Prismatic, (a) basal, and (c+a) slip strengths of commercially pure Zr by micro-cantilever tests," *Acta Mater.*, 2015, doi: 10.1016/j.actamat.2015.06.020.

[24] H. Abdolvand, M. R. Daymond, and C. Mareau, "Incorporation of twinning into a crystal plasticity finite element model: Evolution of lattice strains and texture in Zircaloy-2," *Int. J. Plast.*, 2011, doi: 10.1016/j.ijplas.2011.04.005.

[25] F. Xu, R. A. Holt, and M. R. Daymond, "Modeling lattice strain evolution during uniaxial deformation of textured Zircaloy-2," *Acta Mater.*, 2008, doi: 10.1016/j.actamat.2008.04.019.

[26] R. J. Asaro, "Micromechanics of Crystals and Polycrystals," *Adv. Appl. Mech.*, 1983, doi: 10.1016/S0065-2156(08)70242-4.

[27] R. A. Holt, A. R. Causey, M. Griffiths, and E. T. C. Ho, "in: Proceedin^{gs} of the 12th International Symposium on Zirconium in the Nuclear Industry," in *ASTM STP 1354*, 2000, p. 86.

[28] E. S. Fisher and C. J. Renken, "Single-crystal elastic moduli and the hcp → bcc transformation in Ti, Zr, and Hf," *Phys. Rev.*, 1964, doi: 10.1103/PhysRev.135.A482.

[29] H. Abdolvand, "Progressive modelling and experimentation of hydrogen diffusion and precipitation in anisotropic polycrystals," *Int. J. Plast.*, 2019, doi: 10.1016/j.ijplas.2018.12.005.

[30] A. Alawadi and H. Abdolvand, "Measurement and modeling of micro residual stresses in zirconium crystals in three dimension," *J. Mech. Phys. Solids*, vol. 135, 2020, doi: 10.1016/j.jmps.2019.103799.

[31] L. St-Pierre, E. Héripré, M. Dexet, J. Crépin, G. Bertolino, and N. Bilger, "3D simulations of microstructure and comparison with experimental microstructure coming from O.I.M analysis," *Int. J. Plast.*, 2008, doi: 10.1016/j.ijplas.2007.10.004.

[32] C. Zhang *et al.*, "Effect of realistic 3D microstructure in crystal plasticity finite element analysis of polycrystalline Ti-5Al-2.5Sn," *Int. J. Plast.*, 2015, doi: 10.1016/j.ijplas.2015.01.003.

5 Conclusions and Future Recommendations

5.1 Conclusions

The goal of this project is to characterize the state of micro- and nano -scale residual stresses in Zr-2.5Nb pressure tubes. This is done by firstly investigating how residual stresses develop in a pure Zr specimen using 3D-XRD and CPFE method. EBSD is subsequently used to perform an intensive microstructural and texture analysis on neutron irradiated and unirradiated Zr-2.5Nb pressure tube specimens. Finally, HR-EBSD and CPFE methods are used to characterize the variations of residual stresses in the specimens. The following conclusions are made:

- **Chapter 2:** It is shown in this chapter that thermal residual stresses that develop in α-Zr grains are significant, even after stress relieving and heat treatment. This is due to the high anisotropic properties of the HCP crystals. It is also shown that highly textured samples develop lower micro stresses compared to randomly textured samples. In smaller grains, the value of the grain-average residual stresses is mainly controlled by the localized stresses from grain-grain interactions. The grain-average residual stresses of bigger grains are lower than smaller grains as the area of the bigger grains are high enough to counteract the effects of the localized stresses developing due to grain-neighbor interactions. Also, due to grain neighborhood, stress range increases with grain size.
- **Chapter 3:** It is shown in this chapter that the microstructure of the pressure tube varies along the axial direction. The radial-transverse surface area of the grains in the investigated pressure tube increases with distancing from the front-end of the tube. Most grains in the examined specimens are elongated along the transverse direction. Crystals in all specimens have their c-axis parallel to the transverse direction but the population of c-axes changes among the specimens. The grain-average-misorientation for all samples is less than 1°; however, in some grains, the average misorientation is as high as 4°. Higher misorientation is found in the specimens taken from the front-end of the tubes which indicates the presence of higher residual stresses at the front-end. Also, localized misorientations of 10° and higher were found. High misorientations are also found in the unirradiated samples

which indicate that the pressure tube was probably not fully annealed during the fabrication process.

- **Chapter 4:** In this chapter, the experimental results show that stress variations decrease with distancing from the front-end of the pressure tube which indicates the presence of higher localized stresses at the front-end. CPFE results show that the thermal residual stresses that develop from the heat treatment process are mainly affected by the intragranular misorientation and texture of the specimens, with higher textured specimen developing lower micro stresses. CPFE results show that under the same neutron fluence, the specimens located at the front-end of the pressure tube develop higher stresses; however, when using the measured fluences, the middle of the tube develop higher stresses. Induced stresses by irradiation growth at lower neutron fluences are comparable, in magnitude, to the thermal residual stresses. However, at higher fluences, the stresses from irradiation growth overcome those from thermal residuals.

5.2 Future Recommendations

The long-term goal of this project is to understand the deformation mechanisms of pressure tubes in the operating conditions. This is to improve the micro-scale materials models that are aimed to provide a better prediction of the lifespan of pressure tubes. In this section, a few recommendations are given to achieve this goal:

- It is recommended to perform EBSD analysis on the specimens from the back-end of the tube and compare the results to those from the front-end.

- It is recommended to perform EBSD analysis on the axial-transverse surface of the tube and compare the results to those presented this thesis.

- Characterizing the grains from the transverse-axial and radial-axial of the pressure tube rather than just radial-transverse surface. This is to further investigate the quality of the results obtained from CPFE modeling.

- Using higher resolution experimental techniques such as TEM to characterize the β-Zr grains in the Zr-2.5Nb samples to incorporate β-Zr grains in the CPFE models.

- Modifying the CPFE code to include the effects of irradiation creep, hardening, and softening as well as incorporating a mechanistic irradiation growth formulation to increase the accuracy of the current CPFE simulations.

Curriculum Vitae

Name:	Abdulla Alawadi
Post-secondary Education and Degrees:	The University of Western Ontario London, Ontario, Canada 2014-2018 B.A.
Honours and Awards:	Dean's Honor List 2014-2015, 2015-2016, 2016-2017

Publications:

Alawadi, A., Abdolvand, H*. " Measurement and modeling of micro residual stresses in zirconium crystals in three dimension", *Journal of the Mechanics and Physics of Solids*, 2020, Vol 135, 103799, DOI: https://doi.org/10.1016/j.jmps.2019.103799